UNIVERSITY OF ROCHESTER
LABORATORY FOR LASER ENERGETICS

Volume 168
July–September 2021
DOE/NA/3856-1684

LLE Review

Quarterly Report

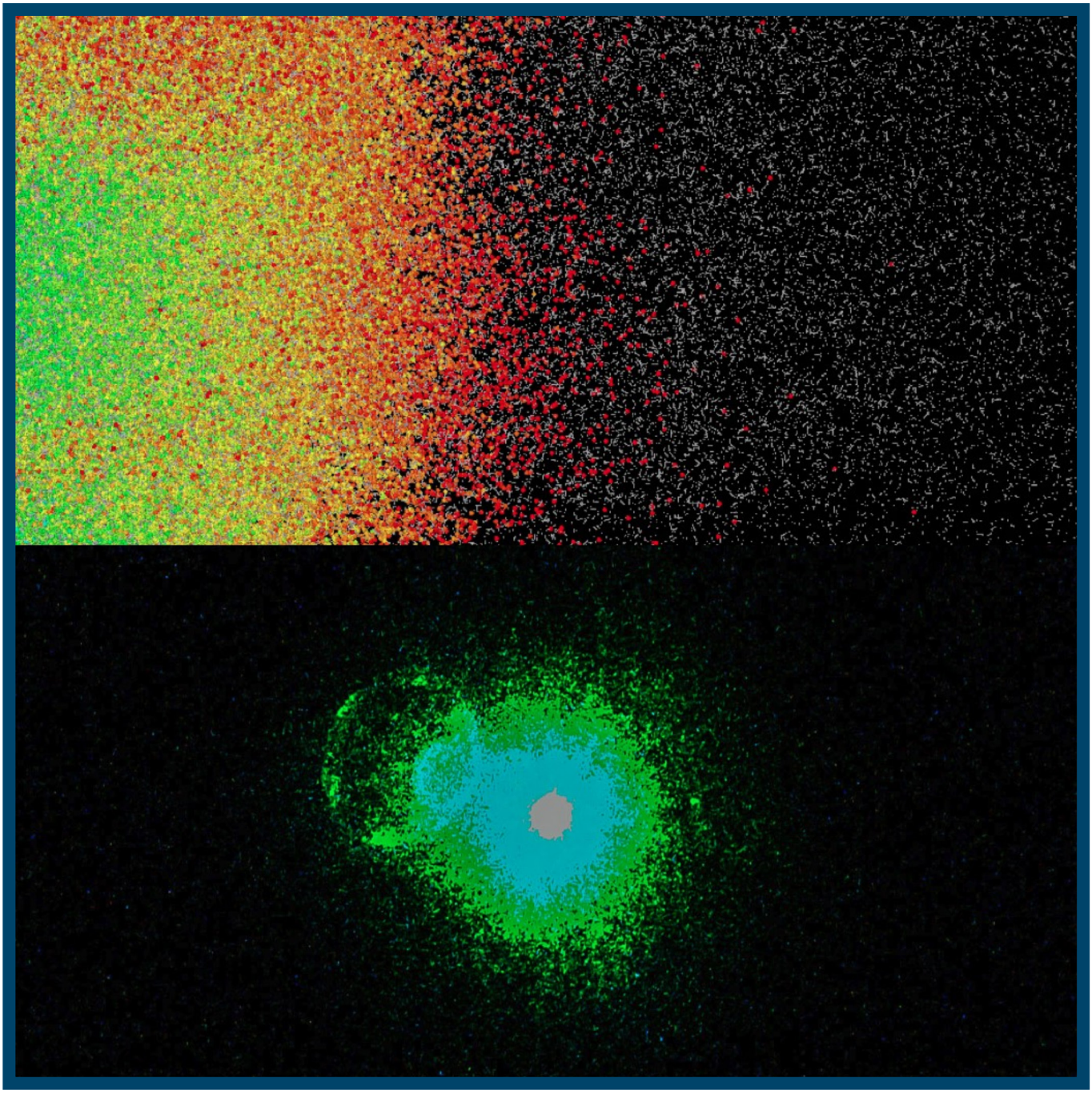

About the Cover:

The cover photo highlights the research on polystyrene (CH) shock release that combines computation and experiments, led by Dr. S. Zhang (LLE) and Dr. D. E. Fratanduono (LLNL), respectively. The top image is a snapshot of the simulation cell showing separation between carbon (color-coded according to their velocities) and hydrogen (white-colored dots) species during the shock release of CH (with u_p = 20 km/s); the bottom image is a view of the target during shot 64742.

In the figure to the right, the experimental target design (a) prevents radiation preheat of the sample and employs a witness foil to investigate the release of shocked CH across a vacuum gap. VISAR reflectivity (b) was observed to change (at the time numbered "4") before fringe shifts (at the time numbered "5"), and similar changes were observed in all experiments of plastics shocked to above 550 GPa, but not in experiments of pure diamond or beryllium. These observations are all consistent with species separation and hydrogen streaming predicted by molecular-dynamics simulations, which were found to occur upon shock breakout and during the release of CH under strong shocks (u_p = 15 km/s or faster, corresponding to 350 GPa or highter) but absent for weak shocks (u_p = 10 km/s or slower, corresponding to 150 GPa or lower.)

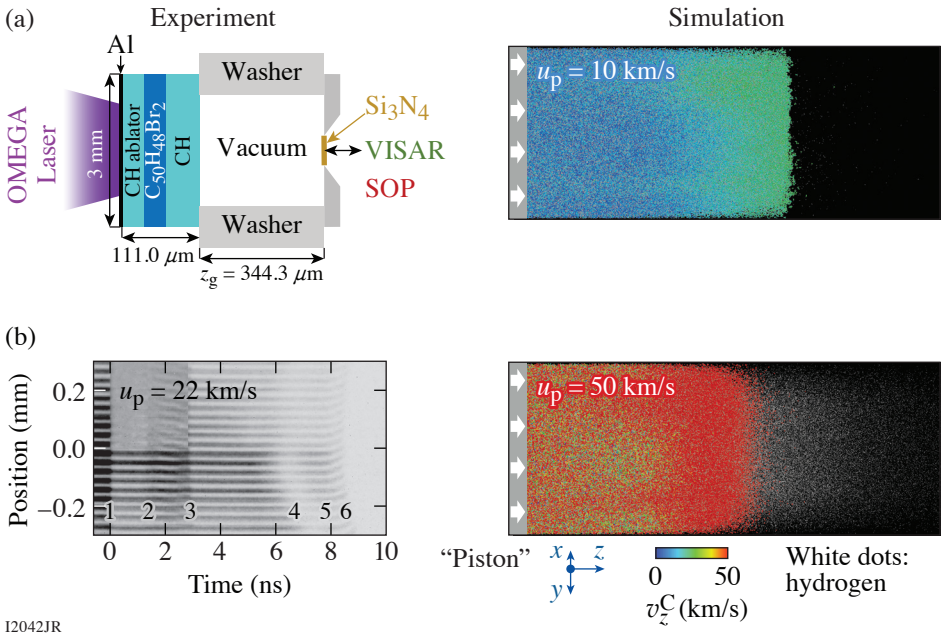

Printed in the United States of America
Available from
National Technical Information Services
U.S. Department of Commerce
5285 Port Royal Road
Springfield, VA 22161
www.ntis.gov

The work described in this volume includes current research at the Laboratory for Laser Energetics, which is supported by New York State Energy Research and Development Authority, the University of Rochester, the U.S. Department of Energy Office of Inertial Confinement Fusion under Cooperative Agreement No. DE-NA0003856, and other agencies.

For questions or comments, contact Erik Power, Editor, Laboratory for Laser Energetics, 250 East River Road, Rochester, NY 14623-1299, (585) 275-0548.

www.lle.rochester.edu

UNIVERSITY OF ROCHESTER
LABORATORY FOR LASER ENERGETICS

Volume 168
July–September 2021
DOE/NA/3856-1684

LLE Review

Quarterly Report

Contents

In Brief

This volume of LLE Review 168 covers the period from July–September 2021. Articles appearing in this volume are the principal summarized results for long-form research articles. Readers seeking a more-detailed account of research activities are invited to seek out the primary materials appearing in print, detailed in the publications and presentations section at the end of this volume.

Highlights of research presented in this volume include:

- S. Zhang *et al.* show that species separation during CH shock release leads to hydrogen streaming and longer scale-length plasmas than those predicted by single-fluid hydrodynamic simulations (p. 189).
- D. H. Edgell *et al.* quantify scattered-light nonuniformity from individual beams and trace the source of nonuniformity back to OMEGA's polarization smoothing (p. 192).
- J. Baltazar *et al.* use brightness profiles of coronal plasma and hot-spot emissions to quantify shell decompression caused by laser-imprint–induced Rayleigh–Taylor instability (p. 195).
- R. H. H. Scott *et al.* use a shallow-cone target to create National Ignition Facility (NIF)-scale ablation plasma densities and show that the dominant instability is convective stimulated Raman scattering (SRS) at densities and intensities relevant for shock ignition (p. 200).
- A. A. Solodov *et al.* present measurements on hot-electron preheat in NIF-scale implosions and show that thin layers of mid-*Z* material buried within the ablator can reduce both SRS and hot-electron preheat (p. 205).
- N. V. Kabadi *et al.* quantify the level of thermal decoupling in deuterium and tritium using data from both OMEGA cryogenic DT experiments and NIF indirect-drive exploding-pusher experiments (p. 208).
- W. Theobald *et al.* measure an energy-coupling increase of (11±4)% using the new small-spot SG-650 distributed phase plates; however, the smaller spots come at the expense of increased instabilities and lower yield and areal density (p. 210).
- G. Bruhaug and A. Kish propose the use of spin-polarized fuels for fusion-based spacecraft propulsion systems and calculate reductions in required shielding mass and ignition requirements and a >30% increase in propulsive efficiency (p. 213).
- X. Bian *et al.* use magnetohydrodynamic simulations to derive a scale-dependent turbulent magnetic Prandtl number and infer a power-law scaling (p. 216).
- A. K. Schwemmlein *et al.* present the first experimental demonstration of triton beam production using target normal sheath acceleration and react the triton beam with a secondary CD target to produce 14.2-MeV DT neutrons (p. 218).
- T. T. Simpson *et al.* propose using cross-phase modulation to produce "flying-focus" spatiotemporally shaped pulses without the constraints on far-field pulse duration, transverse profile, or orbital angular momentum that are inherent in previously developed schemes (p. 220).
- D. I. Mihaylov *et al.* present an improved first-principles equation of state for deuterium, which includes density functional theory-driven molecular dynamics, universal treatment of exchange-correlation thermal effects, and quantum treatment of ions (p. 223).

- P. J. Adrian *et al.* present experimental results using a new x-ray penumbral imager and show the electron-temperature profile measurements are in good agreement with *HYADES* calculations (p. 226).
- I. A. Begishev *et al.* describe the design and capabilities of the Multi-Terawatt (MTW) Laser at LLE (p. 229).
- S.-W. Bahk derives absolute analytic phase solutions for three-wave interactions and shows that for parameters relevant to amplification on MTW-OPAL (optical parametric amplifier line), the signal beam has a pump-beam intensity-dependent phase profile (p. 237).
- G. W. Jenkins, C. Feng, and J. Bromage present an experimental demonstration of divided pulse nonlinear compression and measure a compression factor of 13.4 using 10-mJ input into a four-pulse-division setup (p. 240).
- H. Huang, K. R. P. Kafka, and S. G. Demos simulate electric-field enhancement within subwavelength-scale particles on an optical surface and within the nearby multilayer dielectric coating stack, and show that particles as small as 1/4 the laser wavelength can induce field strengths exceeding coating design parameters (p. 243).
- W. Trickey *et al.* show an increased convergence ratio in simulations of dynamic in-flight shell formation via the use of an extended series of picket pulses. Separate simulations also show the optimal beam-port configurations for mitigation of low-mode perturbations (p. 245).
- C. A. Williams *et al.* present modified cryogenic DT target designs using thin-ice DT liners and predict fusion yields in excess of 1 kJ for a 30-kJ laser drive (p. 248).
- R. S. Craxton summarizes the 32nd LLE Summer High School Research Program. Eight students were invited from Rochester-area high schools to participate in the lab's state-of-the art research environment (p. 251).
- J. Puth *et al.* summarize operations of the Omega Laser Facility during the fourth quarter of FY21 (p. 253).

Erik Power
Editor

Computational and Experimental Evidence of Species Separation in CH Shock Release

S. Zhang,[1] D. E. Fratanduono,[2] M. C. Marshall,[1] J. R. Rygg,[1] A. E. Lazicki,[2] A. Shvydky,[1] D. Haberberger,[1] V. N. Goncharov,[1] T. R. Boehly,[1] G. W. Collins,[1] and S. X. Hu[1]

[1]Laboratory for Laser Energetics, University of Rochester
[2]Lawrence Livermore National Laboratory

Materials shock release, such as that of the CH ablator into the DT fuel or that of DT ice into gas, is involved in different stages of inertial confinement fusion (ICF) and can affect performance but is challenging to quantify both experimentally and theoretically. Typically, the design of ICF experiments relies on single-fluid hydrodynamic simulations. On occasion, however, such simulations omit the microscopic chemistry and physics that play an important role. For example, Thomson-scattering experiments[1] have shown that the fractions of carbon and hydrogen species on the laser-ablation side of a CH_2 foil are different from the initial target composition. Another set of experiments[2] based on optical interferometry measurements of CH shock release found low-density plasmas at locations far ahead of hydrosimulation predictions. Interestingly, when considering radiation transport and pre-expansion at the rear surface of CH before shock arrival, improved agreements with experiments were reached.[2] Follow-up studies,[3] however, indicate that inconsistency remains between simulation and experiments that used a gold shield to prevent radiation preheat.

Recently, S. Zhang and S. X. Hu employed a large-scale molecular-dynamics (MD) approach to simulate the release of strongly shocked CH polystyrene.[4] They found species separation and hydrogen streaming ahead of carbon that produce low-density plasmas whose velocities and scale lengths both match experimental observations. This demonstrates MD as a promising approach for simulating nonequilibrium processes, such as shock release, under extreme conditions. One advantage of the MD approach is that any atomic level kinetic effect is explicitly taken into account. In addition, our calculations show that existing reactive force fields for CH can be readily used for high-pressure applications involving CH and produce post-shock equations of state that are similar to the known Hugoniot of CH in a broad range of pressures (deviations are less than 20% for pressures up to 135 Mbar).

We performed extensive MD simulations and designed new laser-driven experiments by considering different shock strengths to further clarify the microscopic shock-release physics of CH. Our experimental design prevents radiation preheat of the sample and employs a thin (~50-nm) Si_3N_4 foil to witness the release of shocked CH across a vacuum gap [Fig. 1(a)]. Interestingly, we observe VISAR (velocity interferometer system for any reflector) reflectivity changes before fringe shifts [Fig. 1(b)] and similarly for all glow-discharge polymer and CH experiments when shocked to above 550 GPa, but not in the experiments of pure diamond or beryllium. These observations are all consistent with our MD-predicted species separation and hydrogen streaming, which are clearly seen upon shock breakout and during the release of CH under strong shocks (350 GPa or higher) but absent for weak shocks (160 GPa or lower) [Figs. 1(c) and 1(d)]. Furthermore, our experiments show that the velocity of the Si_3N_4 foil jumps up earlier in the case of a stronger shock [Fig. 1(f)]. This is also consistent with our MD results, which show that species momentum ramps up (when hydrogen arrives) before jumping up (as carbon arrives) and that this momentum jumping happens at earlier times for stronger shocks [Fig. 1(e)].

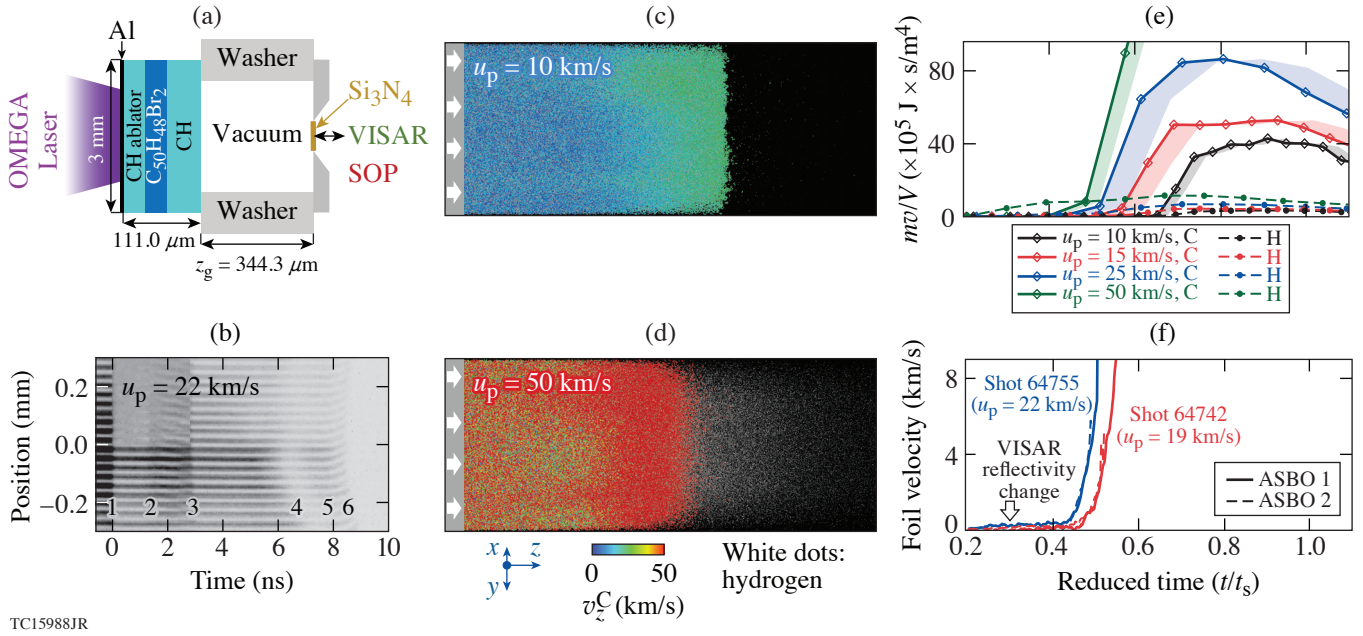

Figure 1
(a) A schematic of the target design and (b) a representative VISAR image of our CH shock-release experiment. An aluminum overcoat and a brominated CH layer are used to prevent radiation preheat of the CH sample. The upper half of the Si_3N_4 foil is coated with titanium. In (b), the numbers "1" to "6" denote the times that the laser turns on, first visibility of the shock front, shock breakout of the CH sample, the reflectivity change of the Si_3N_4 foil, fringe shift indicating motion of the foil, and blankout of fringes, respectively. [(c),(d)] Snapshots of our MD simulations during the release. Carbon atoms are color coded according to their z-component velocities, and hydrogen atoms are shown as white dots. Species separation is clearly observable for strong shocks but absent for weak shocks. (e) Species momentum at the position of a "witness foil" and (f) experimentally measured foil velocities after breakout of shocks with different strength. Time in (e) and (f) is originated from the moment of shock breakout and reduced by the scaling factor $t_s = z_g/u_s$, where z_g is the thickness of the vacuum gap and u_s is the velocity of shock upon breakout. In (e), shaded areas denote the estimated uncertainties in time bounded by the post-shock and first-principles[5] Hugoniot values of u_s. In (f), the time of VISAR reflectivity change in shot 64755 is indicated with an arrow; u_p is the particle velocity in experiments or piston velocity in simulations. ASBO: active shock breakout.

We also quantified the effect of hydrogen isotopes on CH shock release by comparing the results from CH, CD, and CT calculations. We found lighter hydrogen isotopes stream farther away from carbon, while the spatial velocity profiles of different species are similar. This results in higher momentum and energy (by one to two orders of magnitude) of the lighter species/isotopes at the release front of the heavier species. Such differences in streaming rate of different isotopes could lead to degradation of the final compression in ICF experiments, as well as discrepancies between hydrodynamic predictions and experiments.

To understand the effect of radiation preheat on the shock release, we simulated preheated CH by considering samples with different thicknesses. Our calculations show species velocities increase with both the cell size and the degree of preheat, more so for hydrogen than carbon. We also found that the scale length of the species increases with cell size but is not sensitive to preheat. By extrapolating these results to the experimental sample size with 10% thermal expansion (as predicted by hydrodynamic simulations with radiation transport[3]), we can expect the velocity and scale length of the carbon species (or electrons if considering average ionization $\langle Z \rangle \sim 1$) to become comparable to those measured in experiments,[2] which would reconcile the findings from hydrodynamic simulations. Under our established understanding of species separation, however, we must expect that hydrogen runs ahead at much faster velocities and longer scale lengths than carbon. Therefore, we conclude that pre-expansion, if it occurred in the experiment conducted by Haberberger *et al.*,[2] would be much less than 1 μm. This is in clear contrast to hydro-predictions and can be tested by future experiments.

This material is based upon work supported by the Department of Energy National Nuclear Security Administration under Award Number DE-NA0003856, the University of Rochester, and the New York State Energy Research and Development Authority.

1. J. S. Ross *et al.*, Rev. Sci. Instrum. **83**, 10E323 (2012).
2. D. Haberberger *et al.*, Phys. Rev. Lett. **123**, 235001 (2019).
3. A. Shvydky *et al.*, Phys. Plasmas **28**, 092703 (2021).
4. S. Zhang and S. X. Hu *et al.*, Phys. Rev. Lett. **125**, 105001 (2020).
5. S. Zhang *et al.*, Phys. Rev. E **96**, 013204 (2017); S. Zhang *et al.*, J. Chem. Phys. **148**, 102318 (2018).

Nonuniform Absorption and Scattered Light in Direct-Drive Implosions Driven by Polarization Smoothing

D. H. Edgell, P. B. Radha, J. Katz, A. Shvydky, D. Turnbull, and D. H. Froula

Laboratory for Laser Energetics, University of Rochester

Laser-direct-drive symmetric implosions on OMEGA illuminate a target with 60 laser beams and are designed to produce spherical implosions. Simulations suggest that direct-drive laser irradiation nonuniformity must be below the 1% rms level to minimize low-mode nonuniformities and hydrodynamic instabilities that quench the implosion.[1] Observations of light scattered from OMEGA implosions do not show the expected symmetry and have a much larger variation than standard predictions. For the first time, we have quantified the scattered-light nonuniformity from individual beams and identified cross-beam energy transfer (CBET)[2] between the polarization components produced by OMEGA's polarization smoothing as the source of the enhanced nonuniformity.

The 3ω gated optical imager (3ωGOI), scattered-light diagnostic[3,4] was developed to image the light scattered from an implosion. The scattered light appears as a symmetric pattern of 60 distinct spots, each corresponding to a beamlet of light collected from one of the 60 beams. Each beamlet originates from a specific point in the far-field profile of a beam, and as it refracts through the plasma, its intensity varies due to absorption and CBET until it ultimately reaches the diagnostic collection optic. An important feature of the 3ωGOI is a Wollaston prism that splits the collected light into orthogonal horizontal and vertical polarization components that are imaged simultaneously.

In a symmetric implosion, all beamlets collected from beams at the same angular distance from the diagnostic are imaged at the same radial distance from the center of the spot pattern. Figure 1 shows the observed variation (blue circles) in beamlet

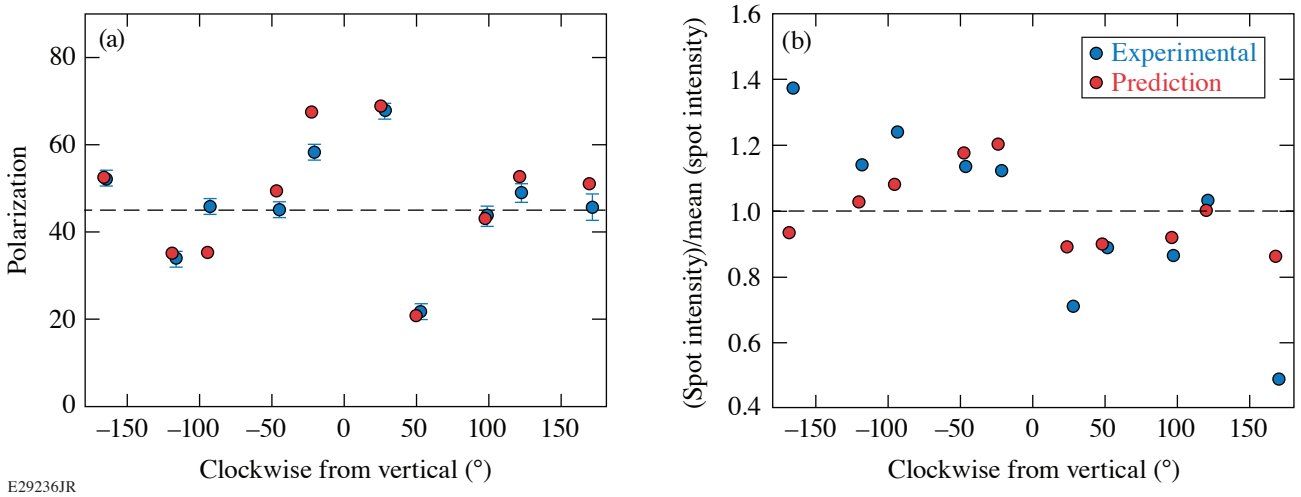

Figure 1
The measured (blue circles) and predicted (red circles) values for the beamlet (a) polarization and (b) intensity as a function of angle from vertical are plotted for a radial beam group.

polarization and total relative intensity for a radial group of beamlets. Truly symmetric laser absorption and CBET should produce constant relative intensity [dashed line in Fig. 1(b)]. Energy exchange due to CBET can rotate the polarization components in the beams,[5] but in a symmetric implosion, the polarization would be altered identically for each beamlet and the polarizations recorded by the 3ωGOI would show symmetry about the vertical and horizontal axes due to the Wollaston prism orientation. No such symmetry about these axes (0°/180° and +90°/–90°, respectively) is observed in Fig. 1(a). Both the observed intensity and polarization of the beamlets indicate that the scattered light from an OMEGA implosion is highly asymmetric.

On OMEGA, each beam is polarization smoothed by passing the laser beams through distributed polarization rotators (DPR's)[6] that split it into two orthogonal polarizations. The split beams exit the DPR with a minute difference in direction that results in an on-target offset of 90 μm. The total on-target overlapped far-field beam profile has two opposite regions in the direction of the offset where the light is mostly linearly polarized. A 3-D CBET model[7] was developed to follow the evolution of the polarization of each split beam as it propagates through the plasma and interacts with crossing beams. When both the DPR-produced polarizations and offsets were used to predict the beamlet polarizations and intensities (red circles in Fig. 1), the measured variation in both was explained. The high correlation between the measured and predicted polarization of the beamlets in Fig. 1(a) demonstrates the accuracy of the modeling, while the correlation between the measured and predicted intensity of the beamlets provides confirmation that the DPR's are responsible for the observed asymmetry in the scattered light.

Enhanced CBET in the strongly polarized regions created by the DPR split offset is a source of asymmetry during an implosion. To illustrate the magnitude of this effect, the 3-D CBET + DPR model was applied to a typical OMEGA cryogenic target implosion and the total time-integrated nonuniformity was calculated. Figures 2(a) and 2(b) show that the total time-integrated nonuniformity over the entire course of an implosion due to CBET and the DPR-polarization split is predicted to be significant for an otherwise symmetric implosion. Figure 2(a) shows the calculated total scattered light over the inner surface of the target chamber wall. The predicted variation in radial exposure is 5.4% rms with a peak to valley over 30%. This large variation demonstrates the significance of this effect on scattered light. Measurements must account for the effect of the DPR offsets to accurately infer laser absorption during implosions on OMEGA.

A relatively simple solution to the issue of DPR + CBET-induced nonuniformity is to fabricate and deploy new DPR's with a decreased spot separation of 10 μm in the far field, which the model predicts will reduce the scattered-light rms variation by a factor of more than 5 to only 0.92%.

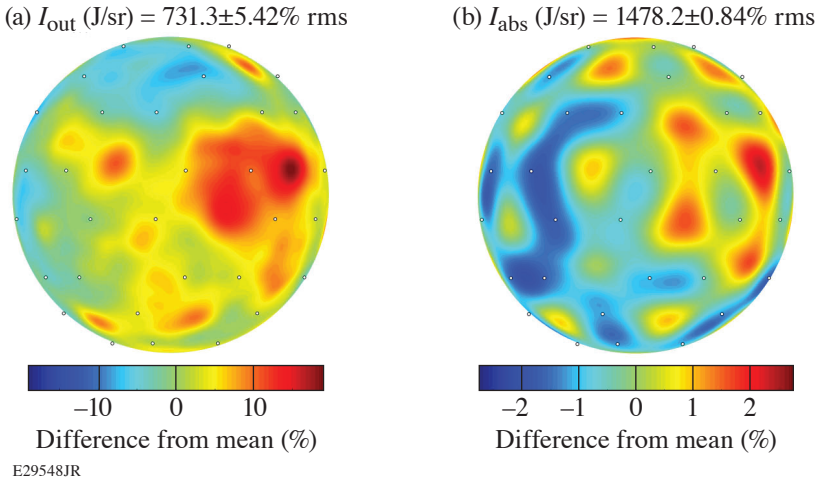

Figure 2
Predicted variation from mean of the (a) scattered light and (b) absorption radiant exposure (J/sr) distributions over a spherical surface for an OMEGA cryogenic implosion using the current DPR's that create a 90-μm offset on target chamber center between the polarization split sub-beams.

This material is based upon work supported by the Department of Energy National Nuclear Security Administration under Award Number DE-NA0003856, the University of Rochester, and the New York State Energy Research and Development Authority.

1. V. N. Goncharov *et al.*, Plasma Phys. Control. Fusion **59**, 014008 (2017).
2. W. L. Kruer *et al.*, Phys. Plasmas **3**, 382 (1996).
3. D. H. Edgell *et al.*, Rev. Sci. Instrum. **89**, 10E101 (2018).
4. D. H. Edgell *et al.*, Rev. Sci. Instrum. **92**, 043525 (2021).
5. P. Michel *et al.*, Phys. Rev. Lett. **113**, 205001 (2014).
6. T. R. Boehly *et al.*, J. Appl. Phys. **85**, 3444 (1999).
7. D. H. Edgell *et al.*, Phys. Plasmas **24**, 062706 (2017).

Feasibility Study of Diagnosing In-Flight Shell Thickness for Laser-Direct-Drive DT Cryogenic Implosions on OMEGA

J. Baltazar,[1,2] R. C. Shah,[1] S. X. Hu,[1,2] K. Churnetski,[1,2] R. Epstein,[1] V. N. Goncharov,[1,2] I. V. Igumenshchev,[1] T. Joshi,[1] W. Theobald,[1,2] and S. P. Regan[1,2]

[1]Laboratory for Laser Energetics, University of Rochester
[2]Department of Mechanical Engineering, University of Rochester

During the deceleration phase of laser-direct-drive inertial confinement fusion experiments, the shell acts as a piston on the fuel, converting its kinetic energy into internal energy of the hot spot and the main fuel. The shell applies a pressure (p_{sh}) on the hot-spot plasma that depends on the in-flight shell thickness (ΔR_i), mass of the shell (M), and velocity of the shell (v), with the relation $p_{sh} \sim \left(M/\Delta R_i^3\right)v^2$ (Ref. 1). The final hot-spot pressure (p_{hs}) scales with the compressive work of the shell, giving $p_{hs} \sim p_{sh}^{5/3}$ [Eq. (62) in Ref. 1]. Many factors in the experiment such as single-beam nonuniformity (laser imprint), target surface debris, and ice roughness, among others, can lead to asymmetric implosions, which perform worse than symmetric implosions. Ablation-surface modulations caused by target features and laser nonuniformity imprint can become the seed for the Rayleigh–Taylor (RT) instability, which further evolves surface modulations at the ablation front during the acceleration phase and decompresses the shell (increases ΔR_i^3), leading to a reduction of the final compression of hot-spot plasma. Surface modulations can be reduced by increasing the shell's entropy, characterized by the shell adiabat $\alpha \sim P/P_F$ and set by the initial picket in the laser pulse (where P_F is the Fermi-degenerate pressure), but there is a trade-off[2] in overall performance. A higher α results in larger ablation velocities and better stability due to increased RT stabilization effects, but with reduced compression achieved in the implosion.[2]

An adiabat study (Refs. 3 and 4), $\alpha \sim 2$ to 6, of plastic-shell implosions using 2-D *DRACO* simulations without laser imprint showed the trend that as the adiabat decreased the shell thickness decreased. When laser imprint was introduced to the 2-D simulations, a decompression of the shell (increase in the shell thickness) was observed and became more prominent as the adiabat decreased due to the decrease in RT stabilization effects. Self-emission measurements taken on OMEGA matched the decompression of the shell observed in the simulations and thus, it was determined that laser imprint explained the decompression of the shell in plastic-shell implosions. A separate adiabat study of DT cryogenic implosions[5] with $\alpha \sim 2$ to 5 using 3-D *ASTER* simulations without laser imprint exhibited a similar trend in the shell thickness to plastic-shell implosions as the adiabat decreased. When laser imprint was introduced to the 3-D *ASTER* low-adiabat ($\alpha \sim 2$) and mid-adiabat ($\alpha \sim 3$) implosions, the shell decompression followed a similar trend to the plastic implosion simulations and measurements. However, measurements of the DT cryogenic implosions did not match the mid-adiabat ($\alpha \sim 3$) implosion simulation; they only matched the low-adiabat implosions ($\alpha \sim 2$). Therefore, it was suggested that additional perturbations or 1-D effects not captured accurately in hydro-simulations may be present in experiments.[5] It is still not clear where the origin of these perturbations occurs; however, some possible sources include the rise of ^{3}He bubbles in the ice layer due to tritium decay, target defects from the cryogenic filing process,[6] and microscopic defects on the ablator surface that were characterized using atomic force microscopy.[7] This motivated an investigation to determine if it was feasible to extend the technique to infer the shell thickness from the self-emission[3,4] of DT cryogenic implosions in order to better understand the effects of laser imprint on shell decompression.

In this work, shell decompression is diagnosed in DT cryogenic implosions from brightness profiles of the coronal plasma and hot-spot emission. Simulations of DT cryogenic implosions are used to study the x-ray signatures for the compressed DT shell. The simulations are post-processed using *Spect3D* to obtain gated images of the x-ray self-emission from the implosion. In experiments,

this is accomplished by recording time-resolved images of x-ray emission from the imploding target using a filtered, 16-pinhole array imager and an x-ray framing camera.[8] The x-ray images are angularly averaged, and the shell thickness is inferred from the separation between the edge of the hot-spot emission and the emission from the outer peak signal, which corresponds with the location of the ablation front. The radial shape from the measurements is dependent on the material of the compressing shell and hot-spot plasma. Therefore, a different analysis is required when analyzing either plastic or cryogenic implosions.

X-ray self-emission measurements of DT cryogenic implosions on OMEGA are simulated using 1-D (*LILAC*) and 3-D (*ASTER*) hydrodynamic codes to study the effects of laser imprint. Metrics for the shell locations were developed by comparing *LILAC* simulations to angularly averaged self-emission profiles.

A 1-D simulation highlighting how the technique is applied to DT cryogenic measurements is shown in Fig. 1. During the acceleration phase, the outer-shell trajectory is obtained by tracking the outer maximum signal point in synthetic gated x-ray images. This signal is blurred by the instrument response function (IRF) and masked by the signal from the hot spot during the deceleration phase; therefore, the trajectory is extrapolated from the acceleration phase to follow a free-fall line in the deceleration phase, where the hot-spot signal has increased and becomes brighter than the signal at the ablation front. The experimental signature for the inner shell turns on after the onset of hot-spot x-ray emission. From comparing the steep gradients in temperature and density from the *LILAC* simulations with the self-emission brightness profiles, it was determined that the inner-shell trajectory is tracked using the 20% intensity from the edge of the hot-spot signal [$I_{20} = 0.20(I_{max}–I_{min}) + I_{min}$]. The 20% intensity point matched the inner-shell location, determined from the hydrodynamic profiles, for different adiabats and target sizes. Taking the difference between the extrapolated and the inner-shell trajectory provides the measurement of the shell thickness over different times.

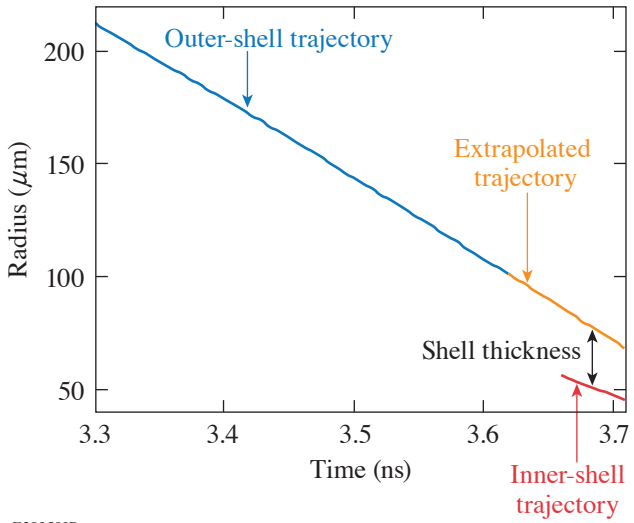

Figure 1
Results from 1-D *LILAC* simulations ($\alpha \sim 2$) and the post-processed (*Spect3D*) measurements show how shell measurements are obtained in the implosion. The outer shell (blue) is tracked using the maximum signal point and is extrapolated to follow a free-fall line (orange) after the laser is turned off. The shell thickness is obtained when the hot spot turns on and the inner-shell (red) trajectory can be tracked.

A comparison of the x-ray–inferred thickness, without applying any spatial or temporal blurring, and the hydrodynamic quantity is shown in Fig. 2. The shell thickness in the 1-D simulation is inferred by tracking the largest gradients in the density profile through measuring the distance between the position of the positive gradient for the inner shell and the negative gradient for the outer shell. In Fig. 2, the gray-shaded region shows that the rebounding shock has not yet collided with the high-density shell. In this time range, the hot spot has not been heated by the shock and the hot-spot emission is low compared to the ablation front. After the shock hits the shell, indicated by the white region in Fig. 2, the hot-spot emission becomes prominent and the x-ray–inferred shell thickness measurements are in agreement with the simulations.

The diagnostic requirements to obtain shell measurements within ~3 μm are ≤10-ps integration and a point spread function with FWHM ≤ 5 μm. The IRF for a pinhole array imager and an x-ray framing camera (20-μm spatial blurring and 40-ps integration), along with other camera parameters, are applied to the synthetic x-ray measurements in Fig. 3 to determine the diagnostic

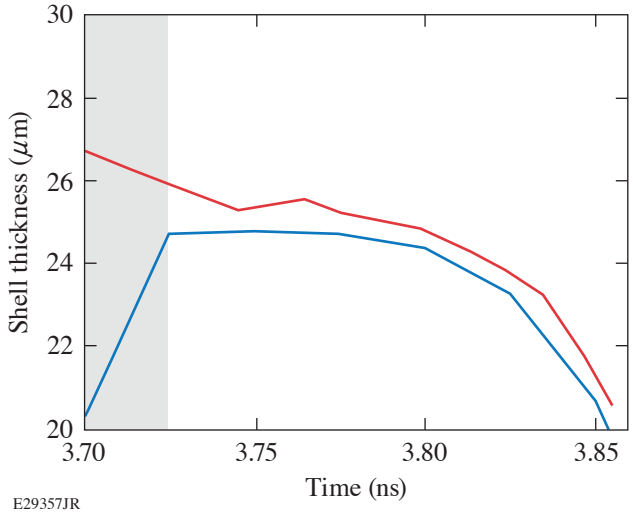

Figure 2
The shell thickness obtained from tracking the hydrodynamic gradients (blue) shows a 1-μm correspondence with shell measurements (without IRF, gray region) after the shock reaches the shell (white region). The temporal and spatial finiteness of the simulations are ~5 ps and ~1 μm, respectively. In the gray region, the rebounding shock has not traversed through the incoming compressing shell; therefore, the emission of the hot spot at this time is low compared to the ablation-front emission.

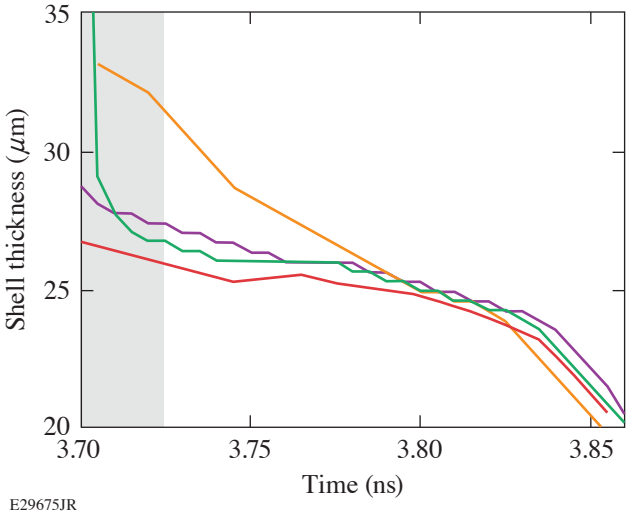

Figure 3
The x-ray measurement without the IRF is shown by gray shading. Various IRF's were applied to the x-ray measurement to determine the diagnostic requirement: 40-ps integration and 20-μm spatial blurring (orange curve), 10-ps integration and 5-μm spatial blurring (purple curve), and 10-ps integration and 1-μm spatial blurring (green curve). As the spatial and temporal blurring increases the x-ray measurement is affected. The diagnostic requirement (purple curve) followed a similar trajectory to the best-case scenario (without spatial and temporal blurring).

requirements to infer the shell thickness. Applying a temporal blurring of 40 ps showed that the x-ray–inferred shell thickness is increased by ~4 μm but follows the same trajectory as the case without any temporal blurring. Therefore, the measurements are not as sensitive to the temporal blurring compared to the spatial blurring of the instrument. The effect from the spatial blurring has a larger effect on the measurements and leads to a reduction in the inferred shell thickness when the spatial blurring increases, as shown in Figs. 4(a) and 4(b). Application of this technique with the current resolution does not give an accurate measurement of the shell thickness; however, this technique can be used to analyze trends in the shell thickness.

Using the current camera parameters (i.e., a spatial resolution of 20 μm and a temporal resolution of 40 ps) on OMEGA,[9] it was determined that the trend in the shell thickness should be analyzed as opposed to the shell thickness alone. An adiabat study was conducted to demonstrate the effectiveness of the analysis technique on 3-D *ASTER* simulations, with and without laser imprint. A range of shell thickness measurements for implosions of $\alpha \sim 1.7$ to 2.8 is shown in Fig. 5. The low-adiabat ($\alpha = 1.7$) implosion with laser imprint shows a clear increase in the trend when compared with the uniform case, while the high-adiabat ($\alpha = 2.8$) implosion shows only a slight increase in comparison, which is expected due to the higher stability. Additionally, the laser-imprint case of the low-adiabat implosion exhibited an advancement of the hot-spot emission, while the high-adiabat case showed no major discrepancy in the onset of the hot-spot emission. The criteria for the onset of hot-spot emission are defined by the time when the hot-spot signal is ~50% of the peak signal. The early hot-spot emission agrees with a previous analysis of the same campaign[5] and is consistent with what was observed in low-adiabat plastic-shell implosions,[3,4] where the advancement of

the onset of hot-spot emission is caused by the laser-imprint–induced RT instability that causes spikes at the ablation front and bubbles to break through the shell, which drives the inner shell farther toward the center during the acceleration phase. This technique will be applied to experimental data[5] and used to further our understanding of laser imprint on DT cryogenic implosions.

This material is based upon work supported by the Department of Energy National Nuclear Security Administration under Award Number DE-NA0003856, the University of Rochester, and the New York State Energy Research and Development Authority.

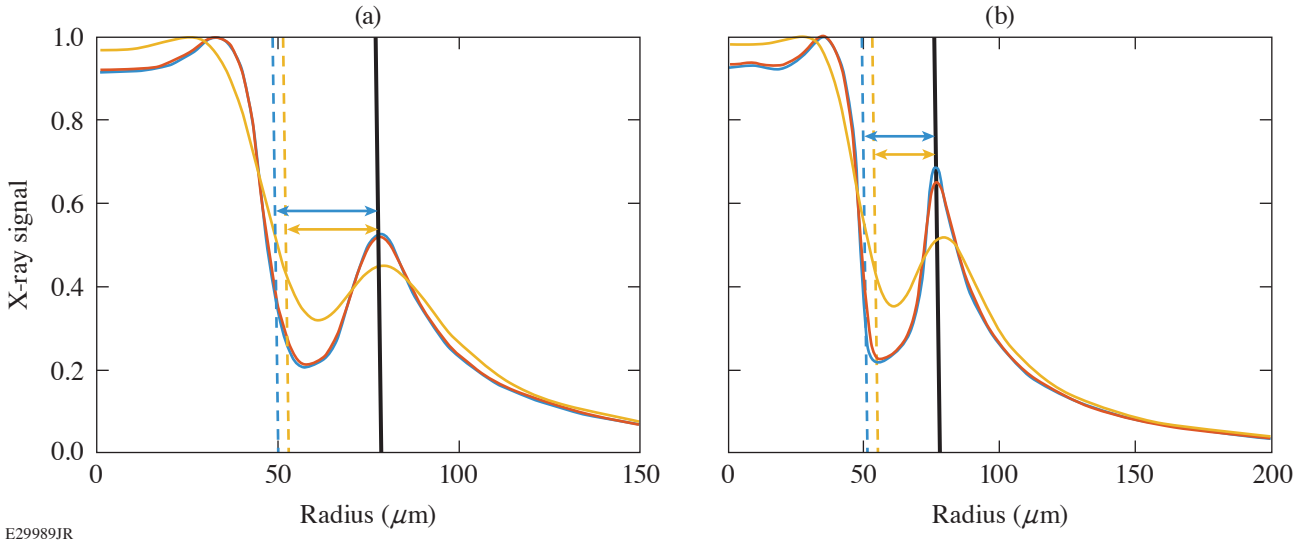

Figure 4
(a) Simulated x-ray brightness profiles obtained in the deceleration phase of a DT cryogenic implosion are shown with an IRF that includes a temporal blurring of 40 ps and a spatial blurring of 1 μm (blue), 5 μm (red), and 20 μm (yellow). The location of the hot-spot boundary was in the same vicinity for the 1-μm and 5-μm cases. Therefore, the location for the hot-spot boundary is shown as dashed lines for the 5-μm (red), and 20-μm (blue) case. (b) Simulated x-ray brightness profiles obtained in the deceleration phase of a DT cryogenic implosion are shown with an IRF that includes a temporal blurring of 10 ps and a spatial blurring of 1 μm (blue), 5 μm (red), and 20 μm (yellow). Increasing the spatial blurring will decrease the inferred shell thickness due to the widening of the diagnosed image of the emission signal profile caused by instrumental effects. Furthermore, the spatial blurring's effect on the measurement is dominant when compared to the effects from the temporal blurring.

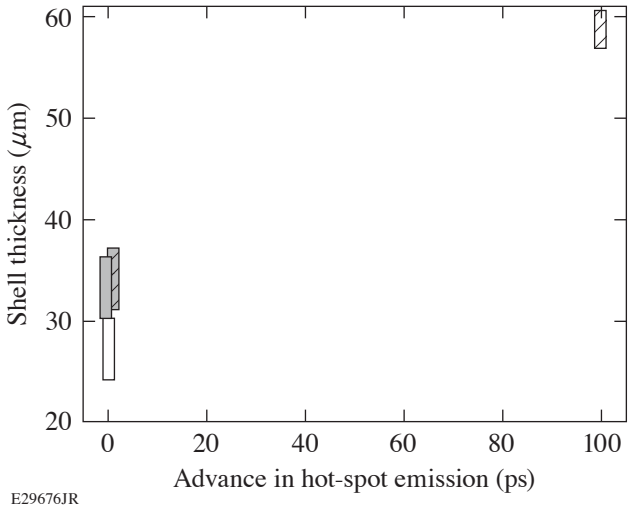

Figure 5
The calculated shell thickness from 3-D *ASTER* x-ray simulations with the IRF of 40-ps temporal resolution and 20-μm spatial resolution for two implosions without (solid color) and with (striped) the effects of laser imprint included: $\alpha = 1.7$ (white box/striped white box) and $\alpha = 2.8$ (gray box/striped gray box). The low-adiabat implosion with laser imprint shows an overall increase in the shell-thickness trend and an advancement in time of the hot-spot emission.[3–5] Both of these characteristics agree with what was observed in plastic-shell implosions. The high-adiabat implosion is less sensitive to the laser-imprint effects and exhibits only a slight increase in the shell thickness and a negligible advancement in time of the hot-spot emission.

1. V. N. Goncharov *et al.*, Phys. Plasmas **21**, 056315 (2014).
2. R. S. Craxton *et al.*, Phys. Plasmas **22**, 110501 (2015).
3. S. X. Hu *et al.*, Phys. Plasmas **23**, 102701 (2016).
4. D. T. Michel *et al.*, Phys. Rev. E **95**, 051202(R) (2017).
5. R. C. Shah *et al.*, Phys. Rev. E **103**, 023201 (2021).
6. I. V. Igumenshchev *et al.*, Phys. Plasmas **20**, 082703 (2013).
7. S. P. Regan *et al.*, Nucl. Fusion **59**, 032007 (2019).
8. D. K. Bradley *et al.*, Rev. Sci. Instrum. **63**, 4813 (1992).
9. A. K. Davis, "Laser Ablation and Hydro-Efficiency of Capsules Imploded in a Direct-Drive Inertial-Confinement-Fusion Configuration," Ph.D. thesis, University of Rochester, 2017.

Shock-Ignition Laser–Plasma Interactions in Ignition-Scale Plasmas

R. H. H. Scott,[1] K. Glize,[1] L. Antonelli,[2] M. Khan,[2] W. Theobald,[3] M. S. Wei,[3] R. Betti,[3] C. Stoeckl,[3] A. G. Seaton,[4] T. D. Arber,[5] D. Barlow,[5] T. Goffrey,[5] K. Bennett,[5] W. Garbett,[6] S. Atzeni,[7] A. Casner,[8] D. Batani,[8] C. Li,[9] and N. Woolsey[2]

[1]Central Laser Facility, STFC Rutherford Appleton Laboratory, UK
[2]York Plasma Institute, Department of Physics, University of York, UK
[3]Laboratory for Laser Energetics, University of Rochester
[4]Los Alamos National Laboratory
[5]University of Warwick, UK
[6]Atomic Weapons Establishment, UK
[7]Dipartimento SBAI, Universita` di Roma "La Sapienza," Italy
[8]CELIA, University of Bordeaux, France
[9]Massachusetts Institute of Technology

The 30-kJ OMEGA—a sub-ignition-scale laser—and a novel shallow-cone target are currently being used to study laser–plasma interactions at ablation-plasma density scale lengths and laser intensities anticipated for direct-drive shock-ignition implosions at National Ignition Facility scale. Our results show that, under these conditions, the dominant instability is convective stimulated Raman scattering (SRS) with experimental evidence of two-plasmon decay (TPD) only when the density scale length is reduced. Particle-in-cell (PIC) simulations indicate that this is due to TPD being shifted to lower densities, removing the experimental backscatter signature, and reducing the hot-electron temperature. The experimental laser–energy coupling to hot electrons was found to be 1% to 2.5%, with electron temperatures between 35 and 45 keV. Radiation-hydrodynamic simulations employing these hot-electron characteristics indicate that they should not preheat the fuel in MJ-scale shock-ignition experiments.

This work describes the first laser–plasma interaction experiment performed at ignition scale and at laser intensities of relevance to shock ignition. A novel target design was created in order to reproduce the anticipated ablation-plasma conditions for an ignition-scale laser-direct-drive implosion using a sub-ignition facility. Planar targets have an infinite radius of curvature and, therefore, the potential for long density scale lengths. Twenty of OMEGA's 60 beams can be coupled onto a planar target and arranged as cones with incidence angles of 23°, 48°, and 62°. Ten of these 20 beams (5 kJ) are used to create a long-density-scale-length ablation plasma, with the remaining ten beams (5 kJ) driving a "shock-ignition" pulse into this preformed ablation plasma. The 62° cone of beams has a high angle of incidence (θ) on target, resulting in beam reflection at low density ($n_{\text{refl}} = n_c \cos^2 \theta$, where n_{refl} is the electron density where reflection occurs), which, in turn, results in inefficient laser absorption. Simulations indicate that the absorption is as low as 60%, reducing the ablation rate and forming short density scale lengths of ~200 μm.

Laser–target coupling is improved using a novel flat-tipped, shallow-cone target and repointing the low-intensity laser beams beyond the cone axis of symmetry. The conical target has the effect of reducing the beams' effective angle of incidence, θ, significantly improving the predicted absorption to 90%. A schematic of the target and example beam position is shown in Fig. 1(a). Furthermore, the conical geometry acts to reduce the divergence of the ablation-plasma flow, further increasing the density scale length. Moreover, maintaining an open-cone geometry avoids on-axis plasma flow convergence and jet formation. Simulations used the 2-D, cylindrically symmetric Lagrangian radiation-hydrodynamic code *H2D*, with 3-D laser ray tracing, *SESAME* equations of state, multigroup diffusive radiation transport, and flux-limited thermal conductivity. The calculated density scale

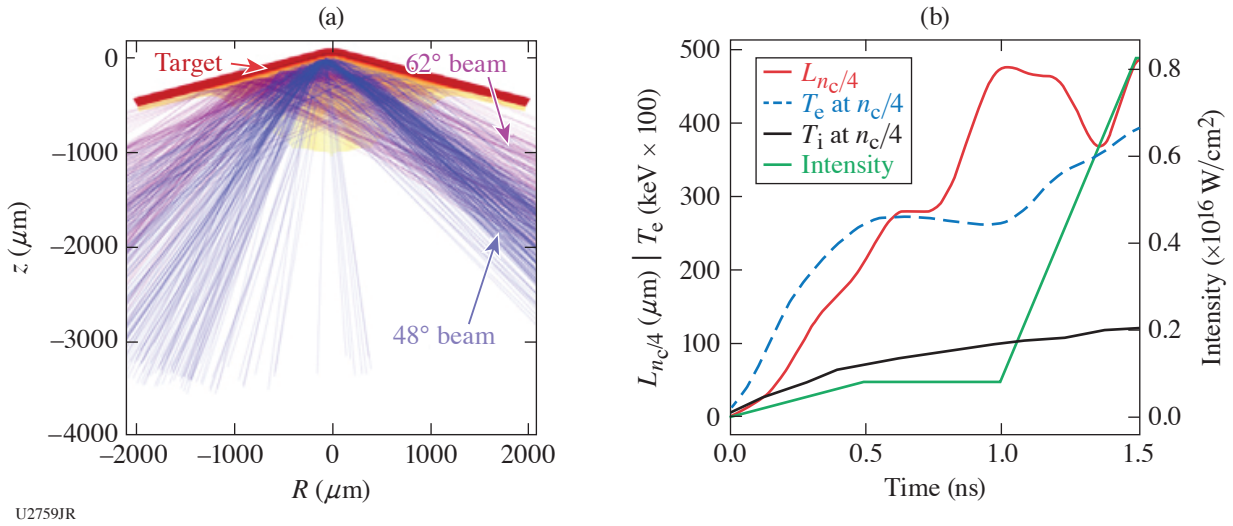

Figure 1
(a) The open-cone target design employed to generate large ablation-plasma scale lengths, shown just before the high-intensity beams switch on at 1 ns. Only two low-intensity beams are shown for clarity. (b) Simulated density scale length, electron temperature, and intensity at $n_c/4$ as a function of time using the open-cone target.

length $L_{n_c/4}$ and electron temperature T_e at the quarter-critical surface, shown in Fig. 1(b), predict ignition-scale density scale lengths of 450 μm and T_e = 3 keV at 1 ns (the time at which the high-intensity interaction commences).

The target (Fig. 1) is comprised of a 3.6-mm-diam cone with 152° opening angle and a 100-μm-diam flat tip. The laser was incident on a 40-μm-thick CH plastic ablator, backed with a 5-μm Cu diagnostic layer, followed by 30 μm of CH to tamp target expansion and prevent electron refluxing. By varying the power in the high-intensity beams on a given shot, a range of peak intensities, corrected for inverse bremsstrahlung absorption, from 8×10^{14} to 8.3×10^{15} W/cm^2 was incident on the $n_c/4$ surface, which simulations indicate was located ~200 μm from the target's front surface. The nominal delay between low- and high-intensity beams was 1 ns. A total of 12 target shots were performed.

Laser light backscattered into two of the high-intensity beams on the 23° beam cone was temporally and spectrally resolved using the full-aperture backscatter (FABS) diagnostic. Backscattered light not entering the beam port was imaged using the near backscatter imager and filtered to distinguish stimulated Brillouin scattering (~351 nm) and SRS and/or TPD (400 to 700 nm) components. Hot-electron production was diagnosed from Cu K-shell line emission using an absolutely calibrated zinc von Hamos (ZVH) spectrometer across the spectral region of 8 to 9 keV and a spherically bent quartz crystal imager (SCI) aligned to the Cu K_α spectral line at 8047.8 eV. The SCI has a narrow spectral window of 8047 to 8054 eV and records data onto an image plate (IP). The hot-electron temperature was inferred from bremsstrahlung emission using a nine-channel, differentially filtered, IP-based, time-integrated hard x-ray image plate (HXIP) over the range of 10 to 200 keV.

Figure 2(a) is an example of the backscattered light spectra with an ~450-μm density scale length. The early-time (<1-ns) backscatter signal is attributed to TPD: the narrowband spectral features above and below 702 nm have previously been shown to be indicative of TPD. As the high-intensity beams ramp up after 1 ns, a broad, bright spectral feature is seen across the 475- to 600-nm range. This broad feature is consistent with backscattered light caused by convective SRS: the backscattered light originates from densities in the range of 0.04 to 0.16 n_c—well below the ~0.22 to 0.25 n_c range where TPD is able to occur.[1] The dashed white line indicates the normalized SRS threshold (I_{thSRS}) assuming a linear density profile. This was found to consistently predict the onset of convective SRS. SRS reflectivity measured in one high-intensity beam port (B25) as a function of single-beam intensity is shown in Fig. 3(b). During the high-intensity part of the drive, no clear evidence of TPD nor absolute SRS was observed. The sharp cutoff in the signal below ~480 nm is not unexpected because the lower densities reduce convective SRS gain and enhance Landau damping; however, it may also be a signature of SRS rescatter.

Bremsstrahlung radiation emission produced via collisions of hot electrons within the target make it possible to estimate the hot-electron temperature. Measurements from the time-integrated HXIP instrument are interpreted using a Geant4-derived instrument response function[2] and χ^2 minimization techniques. Any low-energy x rays from the ablation plasma and/or Cu K-shell emission were removed by excluding the two lower-energy HXIP channels. The inferred hot-electron temperatures are in the range ~35 to 45 keV, as shown by the red ×'s in Fig. 3(a).

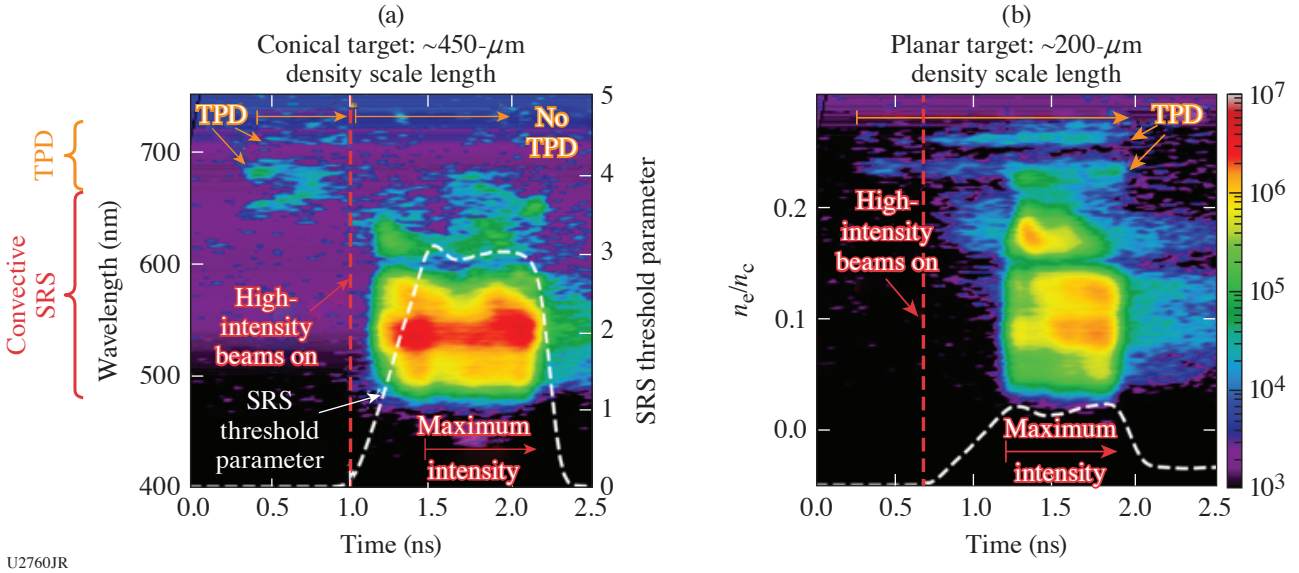

Figure 2

FABS streaked backscatter spectra: (a) Typical long-density-scale-length data: TPD is visible at early time, while during the high-intensity pulse convective SRS dominates. (b) Reduced density scale length with a planar target: TPD is visible throughout. In both cases, the low-intensity beams ramp up from 0 to 0.5 ns, while the maximum intensity is 8.5×10^{15} W/cm^2. The y axes and color scale apply to both plots with densities assuming a temperature of 3 keV. Dashed white lines indicate the SRS threshold parameter (>1 is above threshold), dashed red lines indicate the point at which the high-intensity beams turn on. In the small density scale-length case (where SRS is just above threshold), TPD is visible throughout. This is not the case in the long scale length when SRS is well above threshold. The FABS data were highly reproducible.

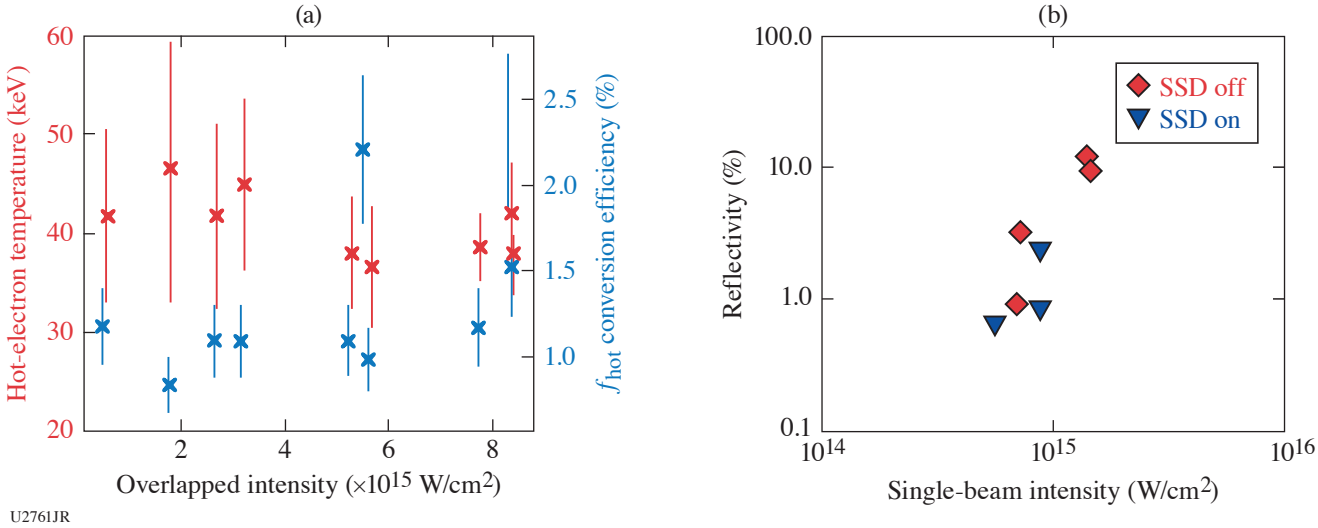

Figure 3

(a) Hot-electron temperature and total laser energy conversion to hot electrons as a function of intensity. (b) SRS reflectivity from (high-intensity) Beam 25.

The fraction of total laser energy converted to hot electrons was inferred from the K_α yield, as measured using the ZVH diagnostic. The number of K_α photons was extracted from background-subtracted ZVH data and then converted into hot-electron energy using Geant4 Monte Carlo simulations that use the cold target geometry and a 40-keV Maxwellian hot-electron population. A conversion efficiency between 1% and 2.5% [blue ×'s in Fig. 3(a)] is inferred, with some suggestion of an intensity dependence. Modeling indicates that laser-ablation–induced x-ray emission did not contribute to the signal. These data are consistent with SCI K_α images.

A comparison measurement at shorter density scale lengths is possible by reducing the delay of the high-intensity beams with respect to the low-intensity beams to 0.7 ns. This limits the plasma expansion duration, reducing the quarter-critical density scale length to ~300 μm [see Fig. 1(b)]. An alternative to laser retiming is to switch to a planar target, which further reduces the density scale length to ~200 μm. Radiation-hydrodynamic simulations predict a reduction in the electron temperature to 2.5 and 2 keV, respectively, for these two cases. At the shortest density scale length [see Fig. 2(b)], TPD is visible throughout the interaction during the low- and high-intensity parts of the laser pulse. Moreover, SRS is just above threshold during the high-intensity interaction. This contrasts with the long-scale-length case, where TPD is not observed and the high-intensity interaction significantly exceeds the SRS threshold. This suggests a transition from a small-scale-length, TPD-dominated regime to a long-scale-length regime, which appears to be dominated by convective SRS.

To investigate the relative roles of TPD and convective SRS in these experiments, 2-D plane-wave PIC simulations were performed with the code *EPOCH*[3] in a density scale length, electron (ion) temperature, and intensity regime of direct relevance to this experiment: 0.1 to 0.26 n_c, 600 μm, 4.5 (2.25) keV, and 2×10^{15} W/cm^2, respectively. These simulations show qualitative agreement with the experiments. Detailed examination of the simulations reveals that the electron plasma waves (EPW's) in the region from 0.20 to 0.24 n_c are principally caused by TPD, which explains the lack of reflected light emitted from this region and provides a compelling explanation for the "Raman gap." The occurrence of TPD at these densities is attributed to convective TPD. The low (32-keV) hot-electron temperature in the simulations—in approximate agreement with experiments—is ascribed to the fact that EPW phase velocities increase rapidly as n_e approaches $n_c/4$. As the EPW wave spectrum, which is comprised of TPD EPW's and low-density SRS EPW's, is shifted below $n_c/4$, EPW phase velocities are limited; consequently, the hot-electron temperature is reduced. At the simulated intensity, convective SRS is just above threshold; therefore, at higher intensities it would be expected that pump depletion, due to convective SRS at lower densities, would play an increasing role in governing the competition between TPD and SRS.[4] Nevertheless, we have shown that a significant factor in the dynamics observed experimentally and via simulation is likely explained by the shifting of TPD to lower densities. This shift removes the experimental $\omega_0 = 2$ "doublet" diagnostic feature, prevents convective SRS backscatter from ~0.20 to 0.24 n_c, and reduces the hot-electron temperature.

To assess the impact that the hot electrons observed in these experiments have on an implosion, we performed 2-D arbitrary Lagrangian–Eulerian radiation-hydrodynamic simulations of a 500-kJ shock-ignition implosion using the code *ODIN*. During the laser ray trace, energy is extracted from the laser (2.5%) and hot electrons are launched from the $n_c/4$ surface with a 40-keV temperature in a 45° cone. A Monte Carlo approach (benchmarked against MCNP) was used for hot-electron transport, scattering, and energy deposition. Using these experimentally measured hot-electron characteristics, the generated pressure is unaffected by the hot electrons with very little degradation in the density profile—an encouraging result for future MJ-scale shock-ignition experiments.

In summary, using a novel target design fielded on the 30-kJ OMEGA Laser System, we have found that for ablation-plasma conditions of relevance to shock ignition, the hot-electron temperature remains relatively low at 35 to 45 keV, with up to ~2.5% of the laser energy converted to hot electrons. Hydrodynamic simulations indicate the low observed hot-electron number and temperature are compatible with shock ignition at MJ scales.

This work was funded by EPSRC Grant Nos. EP/P023460/1, EP/P026486/1, and EP/P026486/1. This work has been carried out within the framework of the EUROfusion Consortium and has received funding from the EuroFUSION research and training programme under Grant Agreement Number 633053. The views and opinions expressed herein do not necessarily reflect those of the European Commission. The involved teams have operated within the framework of the Enabling Research Project: ENR-IFE19.CEA-01 Study of Direct Drive and Shock Ignition for IFE: Theory, Simulations, Experiments, Diagnostics Development.

1. W. Seka *et al.*, Phys. Plasmas **16**, 052701 (2009).
2. M. Stoeckl and A. A. Solodov, Nucl. Instrum. Methods Phys. Res. A **931**, 162 (2019).
3. T. D. Arber *et al.*, Plasma Phys. Controlled Fusion **57**, 113001 (2015).
4. C. Z. Xiao *et al.*, Nucl. Fusion **60**, 016022 (2019).

Hot-Electron Preheat and Mitigation in Polar-Direct-Drive Experiments at the National Ignition Facility

A. A. Solodov,[1] M. J. Rosenberg,[1] M. Stoeckl,[1] A. R. Christopherson,[2] R. Betti,[1] P. B. Radha,[1] C. Stoeckl,[1] M. Hohenberger,[2] B. Bachmann,[2] R. Epstein,[1] R. K. Follett,[1] W. Seka,[1] J. F. Myatt,[3] P. Michel,[2] S. P. Regan,[1] J. P. Palastro,[1] D. H. Froula,[1] E. M. Campbell,[1] and V. N. Goncharov[1]

[1]Laboratory for Laser Energetics, University of Rochester
[2]Lawrence Livermore National Laboratory
[3]Department of Electrical and Computer Engineering, University of Alberta

The direct-drive approach to laser fusion is susceptible to hot-electron preheat due to the long-scale-length plasma conditions near the quarter-critical density of the target $n_c/4$ [where $n_c \approx 1.1 \times 10^{21}\,\lambda_0^{-2}\text{cm}^{-3}$ is the critical density and λ_0 (in μm) is the laser wavelength]. This plasma is susceptible to parametric instabilities, such as stimulated Raman scattering (SRS),[1] that generate electrostatic plasma waves capable of accelerating electrons. For full-scale, direct-drive–ignition experiments, it is estimated that the target adiabat and performance will be negatively affected if more than ~0.15% of the laser energy is coupled into the cold fuel in the form of hot electrons.[2]

In this summary, we report measurements of hot-electron energy deposition in National Ignition Facility (NIF)–scale implosions. Surrogate ~2.4-mm-diam fuel capsules are driven in the polar-direct-drive (PDD) NIF geometry, which are only ~30% smaller than targets for the proposed ignition NIF PDD design.[3] We employ the multilayered target platform to study the hot-electron energy deposition profile in the imploding shell,[4] using mass-equivalent plastic targets with inner Ge-doped layers. Figure 1 shows (a) the laser power shape and [(b),(c)] targets with CH ablators and CH(Ge) payload. Different thicknesses of the Ge-doped layer (35 μm to 59 μm) were used, and the hard x-ray (HXR) emission was compared to the HXR emission from the reference all-CH target. The HXR emission was measured using the ten-channel NIF filter-fluorescer x-ray diagnostic.[5]

NIF target implosions were simulated using the 1-D hydrodynamic code *LILAC*.[6] *LILAC* simulations predict similar coronal conditions for all of the mass-equivalent targets, with a density scale length at the $n_c/4$ surface of 420 μm, an electron temperature of 3.5 keV, and an overlapped intensity of 4.5×10^{14} W/cm^2. Similar coronal conditions indicate similar laser–plasma interaction and hot-electron generation. Indeed, the measured SRS scattered-light spectra were almost identical in the experiments. The Monte Carlo code Geant4 (Ref. 7) modeled hot-electron transport, energy deposition, and bremsstrahlung emission in the imploding shell. Hot electrons were injected at the $n_c/4$ surface with a Maxwellian energy distribution and the temperature (T_{hot}), total energy, and divergence half-angle ($\theta_{1/2}$) were varied to best match the measured HXR spectra; $\theta_{1/2}$ was found to exceed 40° to 45°, the half-angle at which the dense shell is seen from the $n_c/4$ surface during the implosion.

Figure 1(d) shows the HXR spectra measured in the experiments and their best fits using the simulated spectra. The inferred hot-electron temperature is $T_{hot} = 56\pm2$ keV. The hot-electron energy deposition profile for the all-CH target, based on the simulation that best fits the data, is plotted in Fig. 1(e). It shows the cumulative hot-electron energy fraction in percent of the laser energy ($E_L = 720$ kJ) plotted as a function of the radial coordinate in the unimploded shell, measured from the inner shell radius. The inset shows the energy deposition in the unablated part of the shell in more detail. The red circles show the hot-electron energy deposition in the Ge-doped layers in the simulations of the multilayered targets plotted versus the mass-equivalent radius in the all-CH target. The inferred energy depositions in the multilayered and all-CH targets are in good agreement. Most of the hot-electron energy is deposited in the plasma that is ablated during the implosion. The energy deposited in the unablated shell ($R-R_{inner} < 79.5$ μm) is 0.4±0.05% of E_L, with only about half of this energy deposited in the inner 80% of the unablated shell.

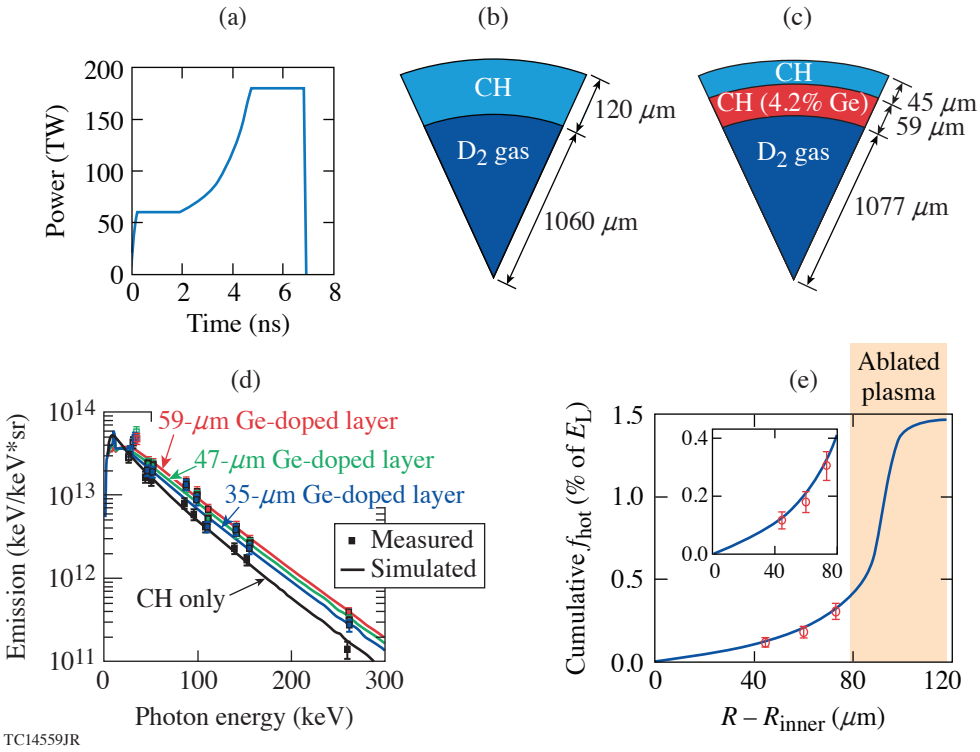

Figure 1
(a) The total laser power profile; [(b),(c)] design of targets with CH ablators; (d) measured and simulated time-integrated HXR spectra; (e) the cumulative hot-electron energy fraction for the all-CH target as function of the radial coordinate in the unimploded shell.

Thin layers of mid-Z material, such as Si, strategically placed in the ablator, can mitigate SRS and reduce hot-electron preheat. Figures 2(a) and 2(b) show the mass-equivalent targets having a buried Si layer in the ablator, designed to pass through the $n_c/4$ region during the laser flattop. This configuration shows significant reduction of SRS compared to the experiment without a Si layer. The inferred hot-electron temperature is $T_{hot} = 52 \pm 2$ keV. With a Si layer, hot-electron energy deposition in the unablated shell is reduced by about a factor of 2, demonstrating an important mitigation effect of the Si layer and providing a promising preheat-mitigation strategy that can expand the ignition-design space to higher intensities. Preheat extrapolation to ignition-scale cryogenic DT implosions on the NIF shows that by using a Si layer, preheat levels can be acceptable for on-target intensities close to 10^{15} W/cm^2.

This material is based upon work supported by the Department of Energy National Nuclear Security Administration under Award Number DE-NA0003856, the University of Rochester, and the New York State Energy Research and Development Authority.

1. W. Seka *et al.*, Phys. Fluids **27**, 2181 (1984); H. Figueroa *et al.*, Phys. Fluids **27**, 1887 (1984); C. S. Liu, M. N. Rosenbluth, and R. B. White, Phys. Fluids **17**, 1211 (1974).
2. J. A. Delettrez, T. J. B. Collins, and C. Ye, Phys. Plasmas **26**, 062705 (2019).
3. T. J. B. Collins *et al.*, Phys. Plasmas **19**, 056308 (2012); T. J. B. Collins and J. A. Marozas, Phys. Plasmas **25**, 072706 (2018).
4. A. R. Christopherson *et al.*, Phys. Rev. Lett. **127**, 055001 (2021).
5. M. Hohenberger *et al.*, Rev. Sci. Instrum. **85**, 11D501 (2014).
6. J. Delettrez *et al.*, Phys. Rev. A **36**, 3926 (1987).
7. S. Agostinelli *et al.*, Nucl. Instrum. Methods Phys. Res. A **506**, 250 (2003).

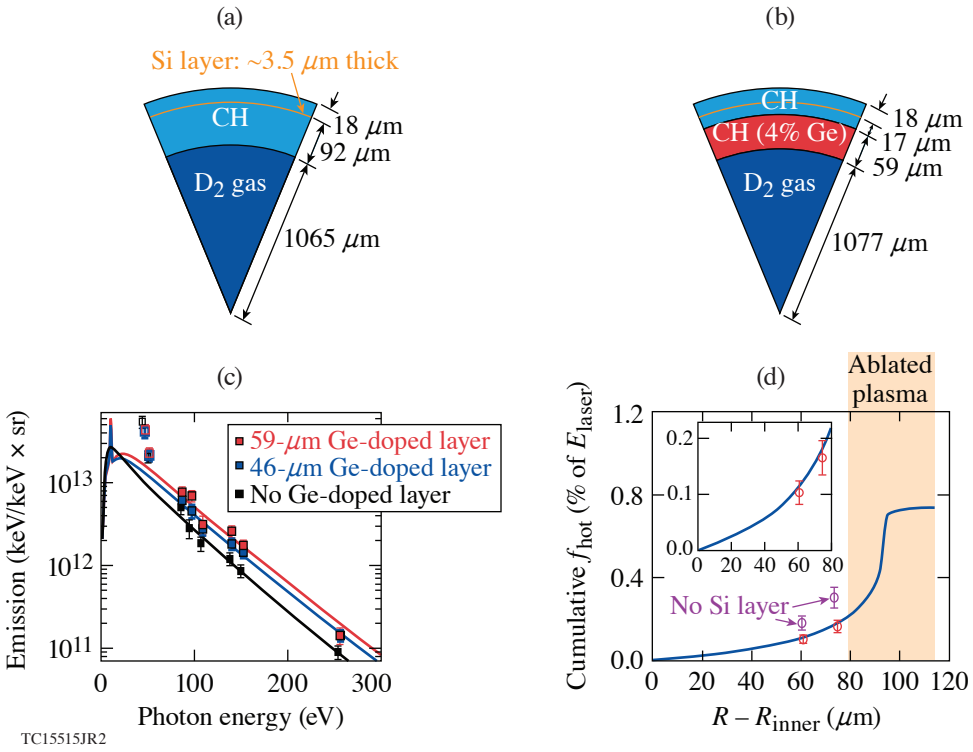

Figure 2
[(a),(b)] Targets with a Si layer in the ablator. (c) Measured and simulated time-integrated HXR spectra. (d) The cumulative hot-electron energy fraction for the target with a Si layer shown in (a) as a function of the radial coordinate in the unimploded shell.

Thermal Decoupling of Deuterium and Tritium During the Inertial Confinement Fusion Shock-Convergence Phase

N. V. Kabadi,[1] R. Simpson,[1] S. Atzeni,[2] J. Eriksson, P. J. Adrian,[1] A. Bose,[1] J. A. Frenje,[1] M. Gatu Johnson,[1] B. Lahmann,[1] C. K. Li,[1] C. E. Parker,[1] F. H. Séguin,[1] G. D. Sutcliffe,[1] C. J. Forrest,[3] S. Fess,[3] V. Yu. Glebov,[3] R. T. Janezic,[3] O. M. Mannion,[3] H. G. Rinderknecht,[3] M. J. Rosenberg,[3] C. Stoeckl,[3] G. Kagan,[4] M. Hoppe,[5] R. Luo,[5] M. Schoff,[5] C. Shuldberg,[5] H. W. Sio,[6] J. Sanchez,[6] L. Berzak Hopkins,[6] D. Schlossberg,[6] K. Hahn,[6] C. Yeamans,[6] and R. D. Petrasso[1]

[1]Plasma Science and Fusion Center, Massachusetts Institute of Technology
[2]Dipartimento SBAI, Universit'a degli Studi di Roma "La Sapienza," Italy
[3]Laboratory for Laser Energetics, University of Rochester
[4]Centre for Inertial Fusion Studies, The Blackett Laboratory, Imperial College, UK
[5]General Atomics
[6]Lawrence Livermore National Laboratory

A series of experiments using DT gas-filled, shock-driven implosions was carried out at the Omega Laser facility. The capsules were nominally 2.3-μm-thick glass shells with an 860-μm outer diameter that were driven by a 0.6-ns square laser pulse delivering 15 kJ. Both the initial fill densities (0.2 to 4 mg/cm^3) and fill ratios (40% to 97% D) were varied. These experiments generated conditions relevant to the shock-convergence phase of hot-spot ignition experiments such as those conducted at the National Ignition Facility (NIF), without being complicated by a subsequent compression phase. With a high ablation rate and minimal residual shell mass, implosions of this type are insensitive to hydrodynamic instabilities. Data from shock-driven, indirect-drive exploding pushers (IDEP's) conducted on the NIF are also used. In these experiments, the spectral DTn and DDn ion temperatures (T_{sDTn} and T_{sDDn}) are inferred from the width of the produced neutron spectra as measured by neutron time-of-light diagnostics. To infer the level of thermal decoupling, the apparent species temperatures (T_{T} and T_{D}) can be inferred directly from the measured spectral temperatures based on the species masses (m_{D} and m_{T}) without accounting for emission weighting due to temperature profiles:

$$T_{\mathrm{D}} = T_{\mathrm{sDDn}}, \tag{1}$$

$$T_{\mathrm{T}} = T_{\mathrm{sDTn}} + \frac{m_{\mathrm{D}}}{m_{\mathrm{T}}}\left(T_{\mathrm{sDTn}} - T_{\mathrm{sDDn}}\right). \tag{2}$$

The differential equation governing the evolution of the ratio of two-ion temperatures due to ion–ion equilibration is given by

$$\frac{d}{\mathrm{d}t}\frac{T_2}{T_1} = -\frac{1}{\tau_{12}}\left(\frac{T_2}{T_1}\right)^2 + \left(\frac{1}{\tau_{12}} - \frac{1}{\tau_{21}}\right)\frac{T_2}{T_1} + \frac{1}{\tau_{21}}, \tag{3}$$

where τ_{21} is the characteristic time at which species 2 equilibrates with species 1, which can be calculated from observables. The solution to this equation, when ignoring the weak dependence on species fraction, can be written as

$$\frac{T_2}{T_1} = \tanh\left[\frac{t}{\tau_{\mathrm{ii}}} + \operatorname{atanh}\left(R_0\right)\right], \tag{4}$$

where the integration constant R_0 is the temperature ratio as t goes to 0 and the total equilibration time is given by the harmonic mean of the τ_{12} and τ_{21}:

$$\tau_{ii} = 2\left[\frac{1}{\tau_{12}} + \frac{1}{\tau_{21}}\right]^{-1}. \tag{5}$$

This dynamic model can be applied to the average observables from an implosion. For the average time scale, τ_N is calculated from the measured DT neutron emission time τ_{DTn}:

$$\tau_N = \frac{\tau_{DTn}}{\tau_{ii}}. \tag{6}$$

Figure 1 shows the apparent ratio of T_T to T_D plotted versus τ_N for three different D:T fill ratios. The observed trend is consistent for all fill fractions and well described by the equation

$$\frac{T_T}{T_D} = \tanh\left[\tau_N + \operatorname{atanh}(1.52\pm0.04)\right], \tag{7}$$

indicating a trend that begins at ≈1.5 and decays to 1 (or thermal equilibrium) at a rate determined by τ_N. Since the initial temperature ratio will be dominated by shock coupling based on ion-species properties, we conclude that the shock coupling scales linearly with mass (D and T have identical charge), $T_i \propto m_i$. Coupling directly proportional to mass is consistent with the rebounding shock stagnating the incoming flow and converting the flow energy of a species into thermal energy. It is also consistent with predictions for the mass dependence of shock coupling[1,2] and recent astrophysical observations of collisionless shock heating.[3]

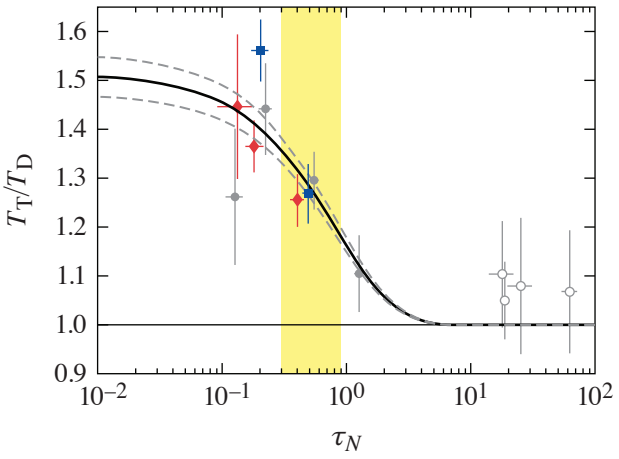

Figure 1
Apparent temperature ratio versus the normalized equilibration time scale for DT gas-filled implosions. Red diamonds are 97:3, gray circles 50:50, and blue squares 40:60 D:T atomic fill ratio. The open gray circles are from NIF IDEP's. All points are consistent with the equation T_T/T_D $[\tau_N + \operatorname{atanh}(1.52\pm0.04)]$, shown by the solid black curve with dashed 95% confidence interval. The reduced χ^2 statistic for this fit is 0.96. The yellow-shaded region represents the conditions most relevant to the shock-convergence phase in NIF ICF implosions.

This material is based upon work supported by the Department of Energy, National Nuclear Security Administration under Awards No. DE-NA0003868 and No. DE-NA0003938.

1. Ya. B. Zel'dovich and Yu. P. Raizer, in *Physics of Shock Waves and High-Temperature Hydrodynamic Phenomena*, edited by W. D. Hayes and R. F. Probstein (Dover, Mineola, NY, 2002), Chap. VII, pp. 515–520.
2. B. D. Keenan *et al.*, Phys. Plasmas **25**, 032103 (2018).
3. M. Miceli *et al.*, Nat. Astron. **3**, 236 (2019).

Enhanced Laser–Energy Coupling with Small-Spot Distributed Phase Plates (SG5-650) in OMEGA DT Cryogenic Target Implosions

W. Theobald,[1,2] D. Cao,[1] R. C. Shah,[1] C. A. Thomas,[1] I. V. Igumenshchev,[1] K. A. Bauer,[1] R. Betti,[1,2,3] M. J. Bonino,[1] E. M. Campbell,[1] A. R. Christopherson,[1] K. Churnetski,[1,2] D. H. Edgell,[1] C. J. Forrest,[1] J. A. Frenje,[4] M. Gatu Johnson,[4] V. Yu. Glebov,[1] V. N. Goncharov,[1] V. Gopalaswamy,[1] D. R. Harding,[1] S. X. Hu,[1,2] S. T. Ivancic,[1] D. W. Jacobs-Perkins,[1] R. T. Janezic,[1] T. Joshi,[1] J. P. Knauer,[1] A. Lees,[1,2] R. W. Luo,[5] O. M. Mannion,[1] F. J. Marshall,[1] Z. L. Mohamed,[1,2] S. F. B. Morse,[1] D. Patel,[1,2] J. L. Peebles,[1] R. D. Petrasso,[4] P. B. Radha,[1] H. G. Rinderknecht,[1] M. J. Rosenberg,[1] S. Sampat,[1] T. C. Sangster,[1] W. T. Shmayda,[1] C. M. Shuldberg,[5] A. Shvydky,[1] C. Sorce,[1] C. Stoeckl,[1] M. D. Wittman,[1] and S. P. Regan[1,2]

[1]Laboratory for Laser Energetics, University of Rochester
[2]Department of Mechanical Engineering, University of Rochester
[3]Department of Physics and Astronomy, University of Rochester
[4]Plasma Science and Fusion Center, Massachusetts Institute of Technology
[5]General Atomics, San Diego

Cryogenic deuterium–tritium ice target implosions on OMEGA with new small-spot ("SG5-650") distributed phase plates (DPP's) achieved an (11±4)% increase in energy coupling compared to implosions with standard-spot DPP's by decreasing the ratio R of the laser spot diameter to the target diameter from 0.93 to 0.75. The ratio R of the laser spot diameter to target diameter is an important parameter for increasing the hydrodynamic efficiency. A significant increase in hydrodynamic efficiency is expected for smaller R. The hydrodynamic efficiency η is defined as the ratio of the kinetic energy of the imploding shell at the end of the acceleration phase and the laser energy, $\eta = (1/2)mv^2/E_L$, where m is the mass of the unablated shell (determined from simulations), v is the shell velocity (determined from shell trajectory measurements), and E_L is the laser energy. The SG5-650 DPP's provide a smaller focal spot size of 674 μm, defined as the diameter that encircles 95% of the measured beam energy compared to 834 μm for the SG5-850. The hydrodynamic efficiency, defined as the ratio of the kinetic energy in the imploding shell to the laser energy, increased from 4.5% to 5.0% based on radiation-hydrodynamic calculations benchmarked to shell trajectory and bang-time measurements. Higher energy coupling came at the expense of increased hot-electron production as well as increased hydrodynamic instabilities seeded by a larger mode-10 amplitude from the beam port geometry, both of which may have reduced the fusion neutron production and areal density.

The shell trajectory from a cryogenic DT target implosion was recorded with the technique described in Ref. 1 for a single-picket–pulse implosion. Figure 1(a) shows the measured trajectory (red crosses) of the imploding shell for shot 91837 compared to simulated trajectories from 1-D radiation-hydrodynamic simulations using *LILAC*,[2] assuming the use of SG5-650 DPP's (black curve). *LILAC* includes a 3-D ray-trace model taking the exact shape of the focal spot into account, a nonlocal electron thermal conduction model,[3] a cross-beam energy transfer model,[4] and first-principles equations of state.[5] In addition, the blue curve shows the predicted trajectory as if the experiment had been performed with SG5-850 DPP's. Similar trajectory measurements driven by laser beams equipped with SG5-850 DPP's are in excellent agreement with the calculated trajectory assuming SG5-850 DPP's in a *LILAC* simulation.[6] As expected, the measured shell trajectory in Fig. 1(a) agrees much better with the simulation for $R = 0.75$ (SG5-650) than for $R = 0.9$ (SG5-850). The simulation with the SG5-850 DPP's shows a delayed shell trajectory. Consequently, the shell implodes faster with the SG5-650 DPP, indicating a higher hydrodynamic efficiency η.

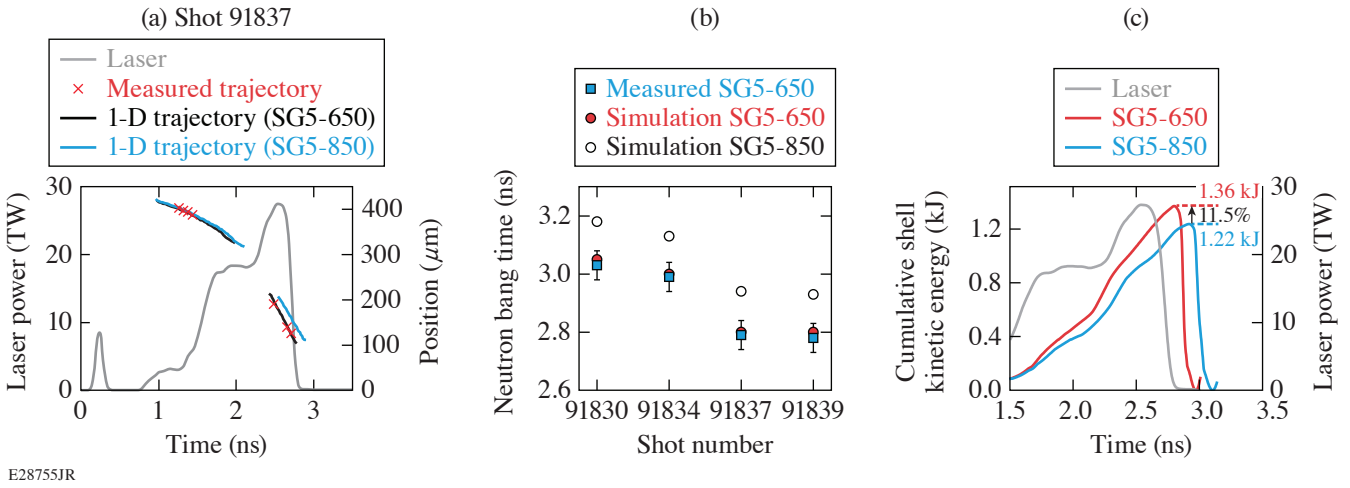

Figure 1
(a) Measured trajectory (red crosses) of the imploding DT cryogenic target shell for shot 91837 in comparison to simulated trajectories assuming SG5-650 DPP's (black curve) and SG5-850 DPP's (blue curve). The gray curve represents the laser pulse. (b) Measured neutron bang time (blue squares) compared to simulated values with SG5-650 (red circles) and SG5-850 (open circles); (c) calculated cumulative shell kinetic energy versus time for shot 91837.

The measured neutron bang time and the absorbed laser-energy fraction support the inferred enhanced energy coupling with SG5-650 DPP's. Figure 1(b) shows the measured neutron bang time (blue squares) compared to simulated values with SG5-650 (red circles) and SG5-850 (open circles). For example, for shot 91837, the measured bang time is 2.79±0.05 ns compared to a predicted bang time of 2.80 ns. Repeating the simulations with SG5-850 DPP's shows that the predicted bang time is later (2.94 ns). The same trend is observed for the other three shots. Knowing that the calculated $(\Delta\eta)_{\text{calc}}$ for shot 91837 is 5.0×10^{-3} and the calculated bang-time shift is 140 ps, the measured bang-time shift of (150±50) ps yields $(\Delta\eta)_{\text{exp}} = (5.5\pm1.8) \times 10^{-3}$. Similar values are obtained for the other three shots since the measured bang-time shifts agree very well with the calculated bang-time shifts. Therefore, the relative increase $(\Delta\eta/\eta)_{\text{exp}}$ is (11±4)% for all four shots and is in agreement with the trajectory measurement and the theoretical value. Figure 1(c) displays the calculated cumulative shell kinetic energy versus time for shot 91837. The energy reaches 1.36 kJ for SG5-650 at bang time and 1.22 kJ for SG5-850; therefore, an 11.5% calculated increase in the kinetic energy of the imploding shell from the smaller-spot DPP. The calculated hydrodynamic efficiency increased from 4.5% with SG5-850 to 5.0% with SG5-650.

Although the experiment provides encouraging results from an increased energy coupling, the overall implosion performance in terms of neutron yield and areal density is poorer compared to other high-performing shots with the SG5-850 DPP's.[6] The smaller DPP focal spots likely limit the implosion performance due to increased hydrodynamic instabilities seeded by low- and mid-mode laser illumination nonuniformity. Three-dimensional hydrodynamic simulations with the code *ASTER*[7] for SG5-650, $R = 0.75$ implosions show a higher susceptibility to low- and mid-mode perturbations induced by target offset, beam mispointing, and power balance compared to similar implosions with SG5-850 and $R = 0.9$. In addition, the beam-port geometry produces, in SG5-650, $R = 0.75$ implosions, a dominant contribution from mid-mode $\ell = 10$.

This material is based upon work supported by the Department of Energy National Nuclear Security Administration under Award Number DE-NA0003856, the University of Rochester, and the New York State Energy Research and Development Authority.

1. D. T. Michel *et al.*, Rev. Sci. Instrum. **83**, 10E530 (2012).
2. J. Delettrez *et al.*, Phys. Rev. A **36**, 3926 (1987).
3. V. N. Goncharov *et al.*, Phys. Plasmas **13**, 012702 (2006).

4. I. V. Igumenshchev *et al.*, Phys. Plasmas **17**, 122708 (2010).
5. S. X. Hu *et al.*, Phys. Rev. E **92**, 043104 (2015).
6. W. Theobald *et al.*, "Enhanced Laser-Energy Coupling with Small-Spot Distributed Phase Plates (SG5-650) in OMEGA DT Cryogenic Target Implosions," to be published in Physics of Plasmas.
7. I. V. Igumenshchev *et al.*, Phys. Plasmas **23**, 052702 (2016).

The Benefits of Spin Polarization for Fusion Propulsion

G. Bruhaug[1,2] and A. Kish[1,3]

[1]Laboratory for Laser Energetics, University of Rochester
[2]Department of Mechanical Engineering, University of Rochester
[3]Department of Physics and Astronomy, University of Rochester

Nuclear fusion has long been considered an ideal method of space propulsion due to the extremely high fuel-specific energy ($\sim 2 \times 10^6$ greater than the best chemical fuels) and exhaust velocity (~4% of the speed of light versus ~4 km/s for the best chemical fuels). This high performance will allow for rapid interplanetary missions as well as interstellar missions within the lifetime of the researchers involved.[1] Fusion propulsion suffers, however, from two primary complications: the difficulty of igniting a self-sustaining fusion chain reaction and the large amount of ionizing radiation generated by the reaction, which requires a considerable mass of shielding to protect against this radiation.[1] This summary describes the ability of a unique, yet well known, nuclear physics technique known as "spin polarization" to lower both the ignition requirements and the flux of ionizing radiation that the spacecraft must handle.

All nuclei possess an inherent angular momentum known as "spin" that plays a significant role in nuclear reactions, especially nuclear fusion. Spin polarization is the process of aligning the nuclear spin vectors of the fusion reactants prior to the reaction. For five-nucleon fusion reactions, notably DT (deuterium and tritium) and D^3He (deuterium and helium-3), spin polarization serves to increase the cross section for fusion and force the reaction products to emit anisotropically. Increasing the reaction cross section lowers the requirements to reach fusion ignition, allowing the spacecraft to use less energy for ignition and requiring less total circulating power during operation. This will decrease both the fusion reactor equipment mass and radiator mass. Additionally, the anisotropic emission of reaction products allows a substantial fraction (up to 80%) of the neutron radiation to be directed away from the spacecraft, reducing the required shielding mass.[2]

Several methods for producing spin-polarized nuclei have been considered and tested for the purposes of nuclear physics experiments and producing beams of spin-polarized particles in particle colliders. For fusion reactors that require a constant stream of gaseous fusion fuel, various optical pumping techniques provide options for creating jets or beams of polarized fusion fuel. These techniques are technologically mature, but they do suffer from various polarization-loss mechanisms, e.g., contact with the walls of the fuel transport system. For fusion reactors that can operate with frozen-fuel injection, spin polarization can be achieved via super chilling of the fuel and/or the application of a strong (>10-T) magnetic field. These methods allow for pellets of prepolarized fuel to be created and stored before injection into the reactor.[2]

A limiting factor on the utility of spin-polarized fuel is the depolarization rate in the fusion reactor.[2] For rapidly pulsed fusion reactors with no significant magnetic fields, the rate of depolarization can be far slower than the expected reaction time. In long-pulse or steady-state fusion reactors, the recycling of fuel from the reactor walls can significantly deplete the population of polarized fuel. Additionally, the presence of an external magnetic field can quickly depolarize the fuel depending on the alignment of the spin polarization with the magnetic field. Such reactor analysis is beyond the scope of this summary, but the authors recommend fusion concepts such as inertial confinement fusion to capitalize on the benefits of spin polarization based on this preliminary analysis.

A unique aspect of spin-polarized DT fusion is the anisotropic emission of the neutrons and alpha particles. This emission profile, seen in Fig. 1 for neutrons, can be leveraged to significantly reduce the neutron radiation impacting the ship while also providing more propulsive efficiency due to the favorable emission profile of the alpha particles (the inverse profile of the neutrons). Figure 2 shows an artistic conception of the change in neutron emission profile on the famous VISTA inertial fusion-powered spacecraft design.

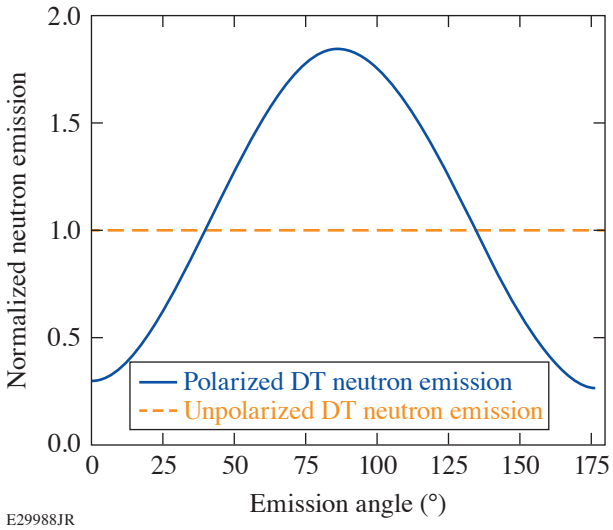

Figure 1
Neutron angular emission profile for polarized and unpolarized DT fuel in the center of mass frame.

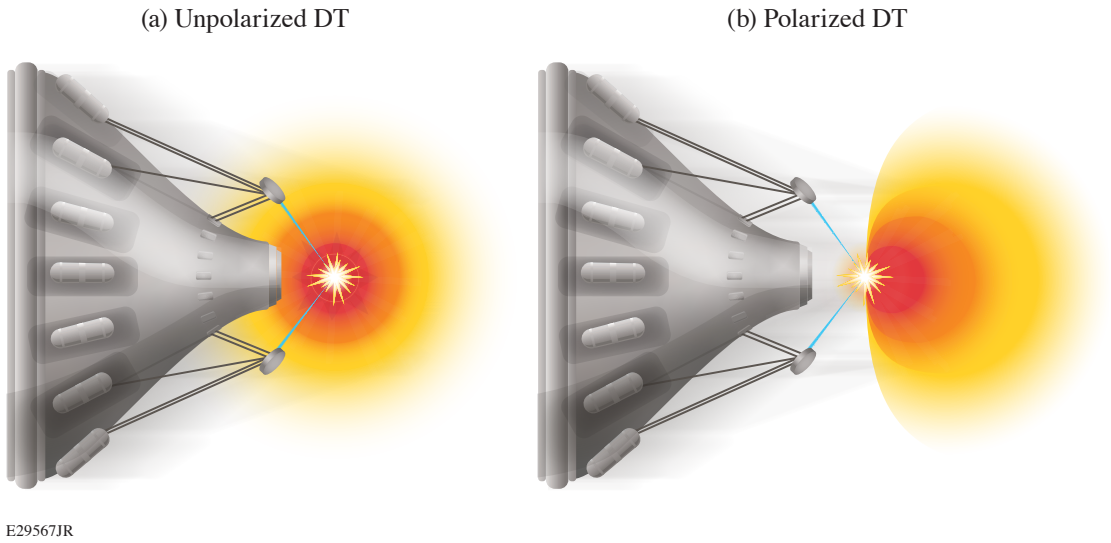

Figure 2
(a) Neutron emission profile from unpolarized DT; (b) Neutron emission from polarized DT.

A conservative analysis was performed to estimate the required radiation shielding, fusion ignition energy, and propulsive efficiency for spacecraft using both spin-polarized DT and spin-polarized D^3He fusion fuel. Based on this analysis we estimate >20% reduction in ignition requirements, ~45% more fusion burnup, ~2% reduction in radiation shielding mass, and >30% increase in propulsive efficiency of the fusion rocket. DT fusion provides the greatest benefits; polarizations >60% were found to provide less radiation flux onto the spacecraft than similarly polarized D^3He fuel. This surprising result shows the incredible potential of spin-polarized DT to act as a power source for future spacecraft.

The authors recommend that future research into fusion spacecraft consider the potential of spin-polarized fuel to improve the structure and performance of spacecraft propulsion and shielding.

1. C. D. Orth, Lawrence Livermore National Laboratory, Livermore, CA, Report UCRL-TR-110500 (2005).
2. G. Ciullo *et al*., in *Nuclear Fusion with Polarized Fuel*, Springer Proceedings in Physics (Springer International Publishing, Switzerland, 2016), Vol. 187, pp. 1–13.

Scaling of Turbulent Viscosity and Resistivity: Extracting a Scale-Dependent Turbulent Magnetic Prandtl Number

X. Bian,[1] J. K. Shang,[1] E. G. Blackman,[2] G. W. Collins,[1,2,3] and H. Aluie[1,3]

[1]Department of Mechanical Engineering, University of Rochester
[2]Department of Physics and Astronomy, University of Rochester
[3]Laboratory for Laser Energetics, University of Rochester

It is widely believed that turbulence plays an important role in the outward transport of angular momentum in accretion disks for inward mass accretion.[1] The simplest conceptual framework is to think of turbulence as an effective (or turbulent) viscosity v_t, which leads to the "turbulent diffusion" of angular momentum at scales far larger than viscous scales; this description has long shaped our thinking of accretion disk dynamics.[2] Similarly, magnetic fields can be transported outward by an effective (or turbulent) resistivity η_t. In this way, the magnetic-field configuration in accretion disks may be influenced by a balance between the inward advection by accretion and the outward diffusion by turbulent resistivity. This balance between the competing effects of v_t and η_t is captured by the turbulent magnetic Prandtl number $\mathrm{Pr}_t \equiv v_t/\eta_t$.

In this summary, we develop a new approach to determine these "effective transport" coefficients acting at different length scales. To our knowledge, our work is the first to calculate the turbulent magnetic Prandtl number as a function of length scale. Our results indicate that it has values of ≈1 to 2 at the smallest ideal hydrodynamic scales, increasing to ≈5 to 10 at the largest scales.

We analyze the coarse-grained kinetic energy (KE) and magnetic energy (ME) density balance of the incompressible magnetohyrodynamic (MHD) equations[3] and extract the effective transport coefficients v_t, η_t, and Pr_t as a function of length scale. We analyze the energy budgets resulting from the eddy viscosity model. Within our coarse-graining framework, this is equivalent to having the rate of energy cascading to scales smaller than l equal to a turbulent dissipation acting on scales $>\ell$:

$$2v_t\left\langle \left| S_\ell \right|^2 \right\rangle \equiv \left\langle \overline{\Pi}_\ell^u \right\rangle, \eta_t\left\langle \left| \overline{\mathbf{J}}_\ell \right|^2 \right\rangle \equiv \left\langle \overline{\Pi}_\ell^b \right\rangle. \tag{1}$$

It is possible to relate v_t and η_t to energy spectra. Indeed, the space-averaged turbulent dissipation can be expressed in terms of energy spectra:

$$\left\langle \overline{\Pi}_\ell^u \right\rangle = 2v_t\left\langle \left| \overline{\mathbf{S}}_\ell \right|^2 \right\rangle = 2v_t\int_0^k k'^2 E^u(k')\mathrm{d}k, \left\langle \overline{\Pi}_\ell^b \right\rangle = \eta_t\left\langle \left| \overline{\mathbf{J}}_\ell \right|^2 \right\rangle = 2\eta_t\int_0^k k'^2 E^b(k')\mathrm{d}k'. \tag{2}$$

The kinetic and magnetic energy spectra scale as

$$E^u(k) \propto k^{-2\sigma_u - 1},\ E^b(k) \propto k^{-2\sigma_b - 1}. \tag{3}$$

The exponents σ_u and σ_b in the scaling of spectra are related to the scaling of velocity and magnetic-field increments:[3]

$$\delta u(\ell) \propto \ell^{\sigma_u},\ \delta B(\ell) \propto \ell^{\sigma_b}. \tag{4}$$

For sufficiently high Reynolds number flows, X. Bian and H. Aluie[4] showed that $\langle \overline{\Pi}^{u}_{\ell} \rangle$ and $\langle \overline{\Pi}^{b}_{\ell} \rangle$ become constant, independent of scale in the so-called "decoupled range." From definitions in Eq. (1), and considering the scaling relations discussed above, we can infer that the turbulent transport coefficients vary with scale in the decoupled range as follows:

$$v_t \propto k^{-2(1-\sigma_u)},\ \eta_t \propto k^{-2(1-\sigma_b)},\ \mathrm{Pr}_t \propto k^{-2(\sigma_b-\sigma_u)}. \tag{5}$$

We conducted pseudo-spectral direct numerical simulations of MHD turbulence using hyperdiffusion with grid resolutions up to 2048^3. Figure 1 shows the effective transport coefficients as a function of scale calculated using their respective definitions in Eq. (1). We can see that $v_t(k) \sim k^{-5/3}$ and $\eta_t(k) \sim k^{-4/3}$ are consistent with relation in Eq. (5) when $\sigma_u = 1/6$ and $\sigma_b = 1/3$, as in our simulations. Moreover, we see that $\mathrm{PR}_t(k) \sim k^{1/3}$, which is also consistent with the derived scaling in Eq. (5) with $\sigma_u = 1/6$ and $\sigma_b = 1/3$ in our simulated flows. For accretion disks, this indicates that the flow may be more efficient at accreting large-scale magnetic fields radially inward than diffusing them outward.

Analyzing the kinetic and magnetic energy cascade rates, we infer power-law scaling in Eq. (5) for v_t, η_t, and PR_t given our definitions of those transport coefficients. This approach circumvents relying on particular values for the spectral scaling exponents (σ_u and σ_b) from a specific MHD phenomenology—whether it exists or not—by relying on results from X. Bian and H. Aluie[4] of conservative KE and ME cascades.

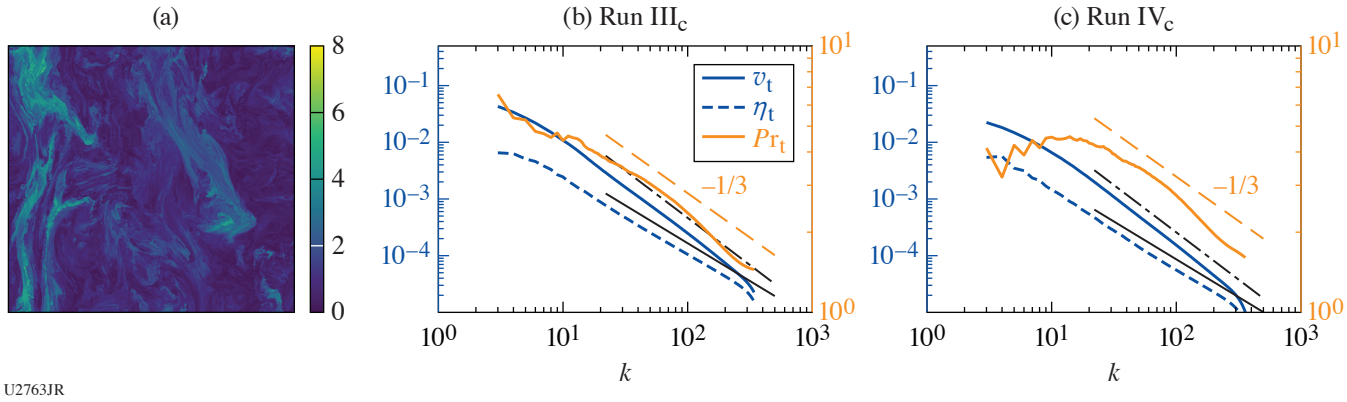

Figure 1
(a) A 2-D slice from a 3-D simulation of turbulent flow subject to a strong external magnetic field in the vertical. It highlights the anisotropic and complex transport in such flows. [(b),(c)] Plots of v_t, η_t, and Pr_t at different scales for two cases at the highest resolution. Three reference lines with a slope of –1/3, –5/3 (dashed–dotted black curve), and –4/3 (solid black curve) are added.

This research was funded by DOE FES grants DE-SC0014318 and DE-SC0020229. Partial funding for this research was provided by the Center for Matter at Atomic Pressures (CMAP), a National Science Foundation (NSF) Physics Frontier Center, under Award PHY-2020249.

1. S. A. Balbus and J. F. Hawley, Rev. Mod. Phys. **70**, 1 (1998).
2. N. I. Shakura and R. A. Sunyaev, Astron. Astrophys. **24**, 337 (1973).
3. H. Aluie, New J. Phys. **19**, 025008 (2017).
4. X. Bian and H. Aluie, Phys. Rev. Lett. **122**, 135101 (2019).

First Demonstration of a Triton Beam Using Target Normal Sheath Acceleration

A. K. Schwemmlein,[1,2] C. Stoeckl,[1] C. J. Forrest,[1] W. T. Shmayda,[1] S. P. Regan,[1] and W. U. Schröder[1,2]

[1]Laboratory for Laser Energetics, University of Rochester
[2]Departments of Physics and Chemistry, University of Rochester

Triton beams provide unique experimental opportunities to study reactions between light nuclei. Of particular interest is the tritium–tritium reaction T(t, 2n)α, which may produce the exotic compound nucleus ^{6}He in an excited state. However, populating the excited state of ^{6}He closest to the entrance configuration of two tritons requires a bombarding energy of at least 2.3 MeV (Ref. 1), which has never been reached experimentally. The results will improve the understanding of both the structure of ^{6}He and the T–T reaction mechanism.

Triton beams up to energies of about 1 MeV have been generated from the 1950s to 1980s in accelerator facilities,[2–4] but tritium contamination of the exposed infrastructure led to a cessation of such experiments. Target normal sheath acceleration[5] (TNSA) isolates the necessary tritium in a small ($500 \times 500 \times 25$-μm^3) target. When exposed to a high-intensity (>10^{16} W/cm^2) laser beam, the target emits energetic (~1-MeV) electrons, which establish a strong (TV/m) electric field that accelerates ions from the target surface. Previous studies using deuterated targets on OMEGA EP[6] demonstrated that deuteron energies of up to 12 MeV are achievable with this technique.

For this study, titanium targets were exposed to approximately 1 bar of 99.97% pure tritium gas at 225°C for 2 h. Several targets were examined separately to determine their tritium content by a thermal desorption process,[7] revealing an activity of 500±10 μCi or approximately 10^{16} tritons. In a first experiment, one target was irradiated by a short (10-ps) OMEGA EP pulse (1.25-kJ, 30-μm focal-spot diameter). The spectra of the emitted ions were analyzed using Thomson parabola ion energy (TPIE[8]) to reveal the triton spectrum shown in Fig 1(a). The experimental data (blue circles) can be fitted reasonably well with a Maxwell–Boltzmann distribution (red curve) and an effective temperature of 1.4±0.1 MeV. This shape is typical for the TNSA process using planar targets. The total integrated yield of tritons was 3×10^{12}, corresponding to a laser-to-triton energy conversion efficiency of approximately 0.04%.

In a proof-of-principle nuclear reaction experiment, a secondary 100-μm-thick deuterated polyethylene (CD) target was arranged parallel to the tritiated target generating the triton beam 5 mm behind the CD target. A standard OMEGA neutron time-of-flight detector,[9] positioned 13.4 m away from the target at 79° to the target normal, was utilized to detect any deuterium–tritium (D–T) fusion neutrons. The neutron spectrum, corrected for instrument and attenuation effects, is shown in Fig. 1(b). The experimental data (blue circles) can be fitted well with a Gaussian (dashed red curve) with parameters 14.2±0.3 MeV (mean±stdev). A Geant4 (Ref. 10) simulation of the experiment is shown by the black curve and accounts for the energy loss of tritons in the CD target and applicable kinematics. The simulation reveals that scattering angles close to 90° greatly reduce the effect of the projectile energy since the momentum transfer from projectile to ejectile becomes very inefficient. In these cases, the Q value of the reaction dominates, and a narrow peak is generated. A total of approximately 10^8 neutrons were produced, in good agreement with predictions by Geant4.

Future experiments will catch the triton beam in a tritiated secondary target to induce T–T reactions at the high energies required to populate the mentioned excited state of ^{6}He. A rapid increase in cross section with triton energy is expected once the state can

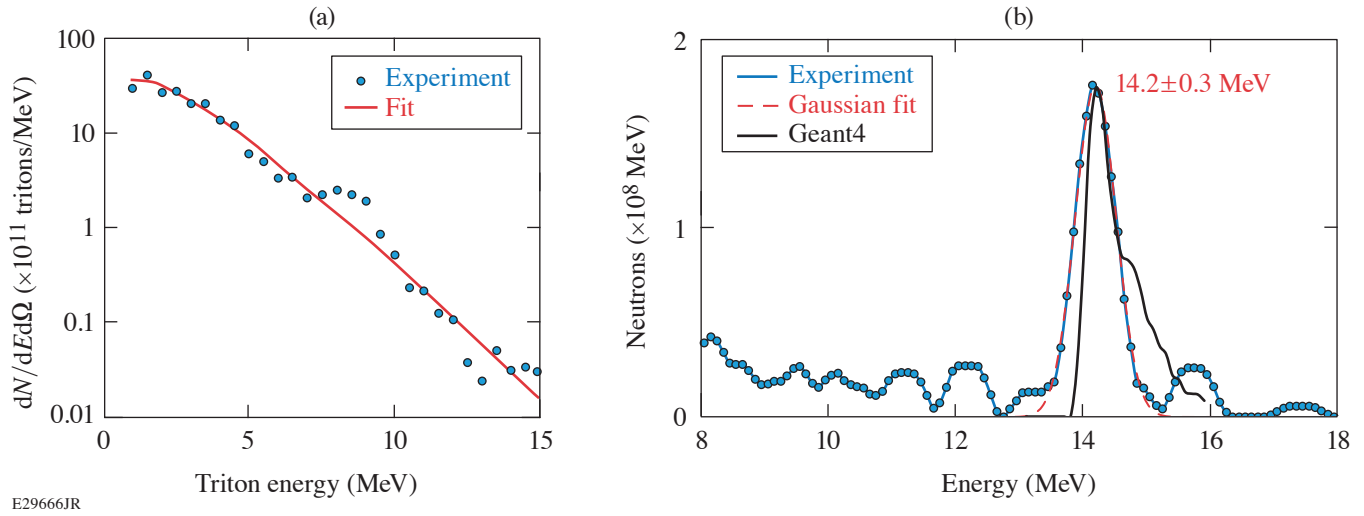

Figure 1
(a) The triton beam spectrum (blue circles) as delivered by TPIE, together with a fit (red curve) to a Maxwell–Boltzmann distribution. (b) The neutron spectrum produced by the D–T reaction experiment (blue circles), together with a Gaussian fit (dashed red curve) and a Geant4 simulation (solid black curve).

be populated, and the shape of the neutron spectrum will reveal details about the reaction mechanism.[11] Further experiments are planned with secondary lithium and beryllium targets to produce exotic, neutron-rich isotopes of these elements via di-neutron transfers. These isotopes are of interest to *ab initio* structure modeling[12,13] and reaction networks in stars.[14]

This material is based upon work supported by the Department of Energy National Nuclear Security Administration under Award Number DE-NA0003856, the University of Rochester, and the New York State Energy Research and Development Authority.

1. TUNL Nuclear Data Evaluation, Energy Level Diagrams for A = 6, Accessed 30 November 2021, https://nucldata.tunl.duke.edu/nucldata/figures/06figs/menu06.shtml.
2. C. Wong, J. D. Anderson, and J. W. McClure, Nucl. Phys. **71**, 106 (1965).
3. A. A. Jaffe *et al.*, Proc. Phys. Soc. **76**, 914 (1960).
4. R. Woods, J. L. McKibben, and R. L. Henkel, Nucl. Instrum. Methods **122**, 81 (1974).
5. S. C. Wilks *et al.*, Phys. Plasmas **8**, 542 (2001).
6. C. Stoeckl *et al.*, Nucl. Instrum. Methods Phys. Res. B **453**, 41 (2019).
7. C. Fagan *et al.*, Fusion Sci. Technol. **76**, 424 (2020).
8. J. A. Cobble *et al.*, Rev. Sci. Instrum. **82**, 113504 (2011).
9. C. J. Forrest *et al.*, Rev. Sci. Instrum. **83**, 10D919 (2012).
10. GEANT4: A Simulation Toolkit, CERN Accelerating Science, Accessed 2 Aug 2021, https://geant4.web.cern.ch/node/1.
11. B. Lacina, J. Ingley, and D. W. Dorn, Lawrence Livermore National Laboratory, Livermore, CA, Report UCRL-7769 (1965).
12. C. Cockrell, J. P. Vary, and P. Maris, Phys. Rev. C **86**, 034325 (2012).
13. C. Forssén *et al.*, Phys. Rev. C **71**, 044312 (2005).
14. M. Terasawa *et al.*, Astrophys. J. **562**, 470 (2001).

Spatiotemporal Control of Laser Intensity Through Cross-Phase Modulation

T. T. Simpson, D. Ramsey, P. Franke, K. Weichman, M. V. Ambat, D. Turnbull, D. H. Froula, and J. P. Palastro

Laboratory for Laser Energetics, University of Rochester

Spatiotemporal pulse shaping provides control over the trajectory and range of an intensity peak. While this control can enhance laser-based applications, the optical configurations required for shaping the pulse can constrain the transverse or temporal profile, duration, or orbital angular momentum (OAM). Here we present a novel technique for spatiotemporal control that mitigates these constraints by using a "stencil" pulse to spatiotemporally structure a second primary pulse through cross-phase modulation (XPM) in a Kerr lens. The temporally shaped stencil pulse induces a time-dependent focusing phase within the primary pulse. This technique, the "flying-focus X," allows the primary pulse to have any profile or OAM, expanding the flexibility of spatiotemporal pulse shaping for laser-based applications. As an example, simulations show that the flying-focus X can deliver an arbitrary-velocity, variable-duration intensity peak with OAM over distances much longer than the Rayleigh range.

Spatiotemporal pulse shaping offers a new paradigm for controlling laser intensity. By exploiting space–time correlations in the amplitude or phase of a laser pulse, a number of recent techniques have created arbitrary-velocity intensity peaks that remain nearly propagation invariant over distances much longer than the Rayleigh range. These features promise to revolutionize a wide range of laser-based applications, including high-power amplifiers and compact accelerators. Nevertheless, each of the existing techniques requires an optical configuration that constrains properties of the intensity peak, such as its transverse or temporal profile, duration, or OAM. As an example, the original "chromatic" flying focus uses a chirp and a chromatic lens to control the time and location at which each temporal slice of a laser pulse comes to focus, respectively. While this technique offers some flexibility to shape the transverse profile of the far field, the chromatic aberration and chirp can place a lower bound on the duration of the intensity peak that is much larger than the transform-limited duration.[1,2] An alternative technique, the "achromatic" flying focus, employs the spherical aberration of an axiparabola to focus different annuli in the near field to different axial locations in the far field and an echelon to adjust their relative timing.[3,4] Here, the intensity peak can have a near-transform-limited duration, but the flattop transverse profile required in the near field and the spherical aberration of the axiparabola fully determine the far-field profile.

We describe a novel technique for spatiotemporal control: the "flying-focus X," which combines temporal pulse shaping with XPM to produce an ultrashort, arbitrary-velocity intensity peak, with or without OAM, over distances far greater than the Rayleigh range. Specifically, a temporally shaped, high-intensity "stencil" pulse induces the time-dependent focusing of a second "primary" pulse through XPM in a medium with an intensity-dependent refractive index (Kerr lens) (Fig. 1). The minimum and maximum intensity of the stencil pulse set the focal range of the primary pulse, while its duration sets the velocity of the resulting intensity peak. Use of a stencil pulse mitigates the constraints on the primary pulse, allowing for spatiotemporal control independent of properties such as the far-field duration, transverse profile, or OAM. In effect, these constraints are offloaded onto the stencil pulse. As a result, flying-focus X provides unprecedented flexibility for structuring the far-field properties of the intensity peak, promising to further enable or enhance a wide range of laser-based applications.

Figure 1 illustrates how temporal pulse shaping and XPM can be used to control the trajectory and range of an intensity peak. A stencil pulse and a primary pulse, overlapped in space and time, co-propagate along the z axis and enter a convex, parabolic

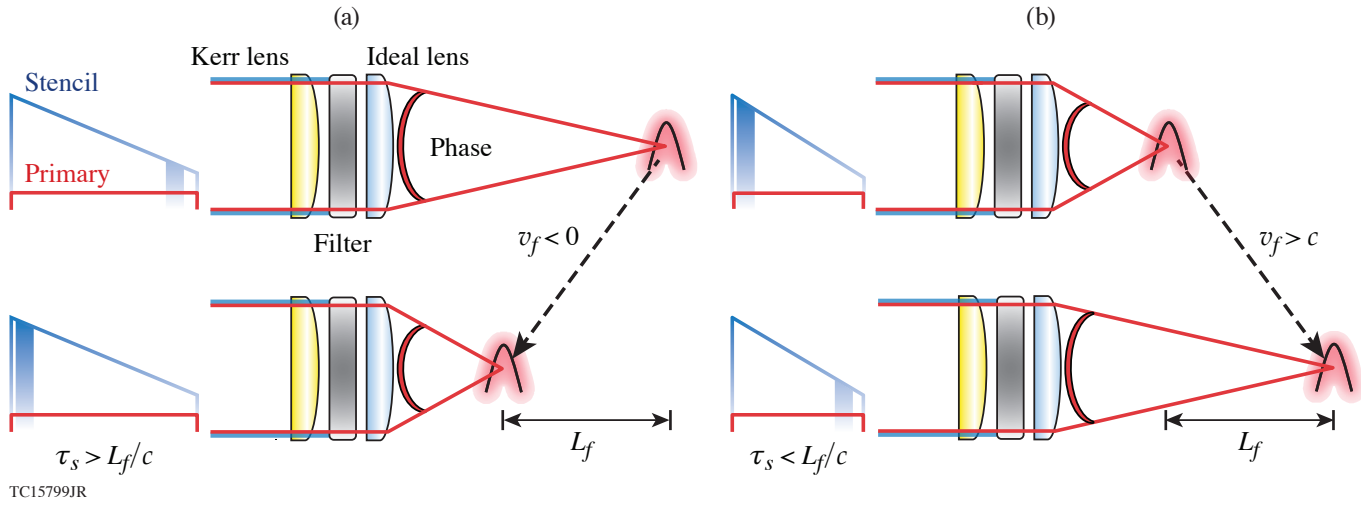

Figure 1
A schematic of the flying-focus X. A high-intensity stencil pulse with a flattop transverse and shaped temporal profile co-propagates with a low-intensity primary pulse. The stencil induces a time-dependent focusing phase on the primary in a parabolic Kerr lens. A filter removes the stencil, while an ideal lens provides additional focusing for the primary. The resulting focus travels over a distance L_f at a velocity v_f, both of which can be tuned by shaping the temporal profile of the stencil. A stencil pulse with an intensity that ramps up in time can produce either (a) negative or (b) positive superluminal focal velocities depending on its duration τ_s.

Kerr lens. The two pulses have distinct wavelengths or polarization vectors, and the stencil intensity is much greater than the primary intensity. The stencil pulse has a flattop transverse profile, which, in combination with the parabolic shape of the Kerr lens, ensures that the primary pulse acquires an aberration-free wavefront curvature. The instantaneous intensity of the stencil dictates the time dependence of that curvature, with high stencil intensities inducing greater curvature. The time-dependent wavefront curvature is equivalent to that applied by an ideal lens with a time-dependent focal length. As a result, the primary pulse can have any transverse profile or orbital angular momentum, in addition to the extended focal range and velocity control afforded by previous spatiotemporal pulse-shaping techniques.

Simulations show that the flying-focus X can create an ultrashort-duration intensity peak traveling near the vacuum speed of light over many Rayleigh ranges (Fig. 2)—a configuration ideal for advanced accelerators.[5,6] To produce the desired focal velocity, the stencil intensity ramps up linearly in time over ~330 fs. In the far field, the ≈10-fs intensity peak maintains its diffraction-limited Gaussian spot over the entire focal range (L_f = 1 cm), while traveling at a focal velocity v_f = 1.01 c.

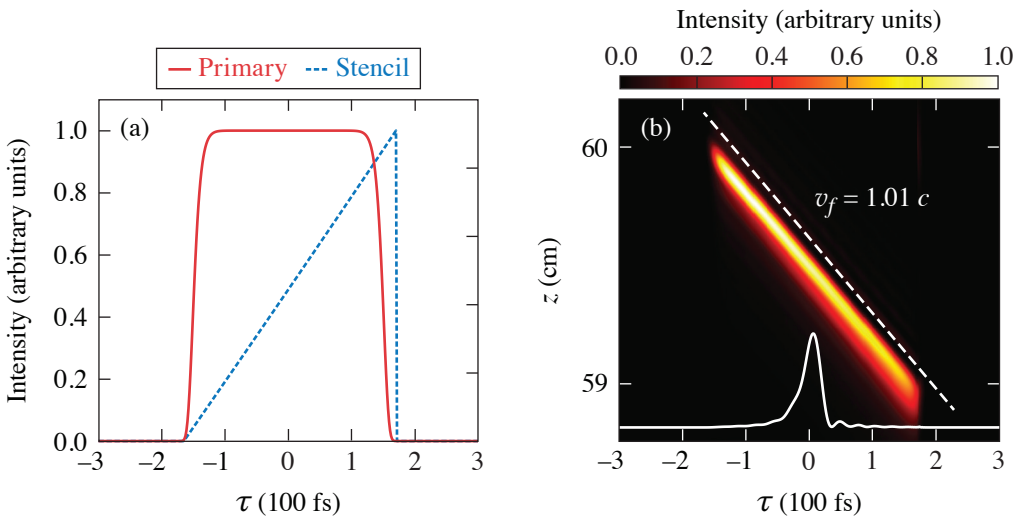

Figure 2
Simulation results for a flying-focus X pulse with v_f = 1.01 c, demonstrating velocity control, an ultrashort duration, and near propagation invariance through the focal range. (a) The temporal profile of the stencil and primary pulses at the entrance of the Kerr lens. (b) The maximum intensity of the primary pulse in the far field and a lineout of its temporal profile. All values are normalized to their respective maxima and $\tau = t – z/c$.

The work published here was supported by the U.S. Department of Energy Office of Fusion Energy Sciences under contract No. DE-SC0016253, the Department of Energy under Cooperative Agreement No. DE-NA0003856, the University of Rochester, and the New York State Energy Research and Development Authority.

1. D. H. Froula *et al.*, Nat. Photonics **12**, 262 (2018).
2. A. Sainte-Marie, O. Gobert, and F. Quéré, Optica **4**, 1298 (2017).
3. J. P. Palastro *et al.*, Phys. Rev. Lett. **124**, 134802 (2020).
4. C. Caizergues *et al.*, Nat. Photonics **14**, 475 (2020).
5. P. Franke *et al.*, Phys. Rev. A **104**, 043520 (2021).
6. J. P. Palastro *et al.*, Phys. Plasmas **28**, 013109 (2021).

Improved Equation-of-State Table of Deuterium for High-Energy-Density Applications

D. I. Mihaylov, V. V. Karasiev, S. X. Hu, J. R. Rygg, V. N. Goncharov, and G. W. Collins

Laboratory for Laser Energetics, University of Rochester

We present an improved first-principles equation-of-state (iFPEOS) table of deuterium that is an update on the previously established FPEOS table[1,2] by introducing (1) fully consistent molecular dynamics (MD) driven by density functional theory (DFT) treatment for all ρ–T points, (2) a universal treatment of exchange-correlation (XC) thermal effects, and (3) quantum treatment of ions. This new iFPEOS includes ρ points in the range of $1 \times 10^{-3} \leq \rho \leq 1.6 \times 10^{3}$ g/cm^3 and T points in the range of 800 K $\leq T \leq$ 256 MK, thereby covering the challenging warm-dense-matter regime.

For an improved description of the electronic structure at high T, iFPEOS employs newly developed T-SCAN-L (Ref. 3), which is a free-energy XC density functional with explicit temperature dependence at the meta-generalized gradient approximation (meta-GGA) level of DFT. Previous models such as FPEOS and other popular DFT-based models[4] rely on the zero-T, GGA-level XC functional PBE (Perdew–Burke–Ernzerhof). Therefore, iFPEOS provides an improvement in accuracy by taking into account important XC thermal effects[5] and including the higher-level, more-accurate treatment of the XC interaction. In addition, we combine T-SCAN-L with the rVV10 XC functional in order to account for van der Waals interactions. Recently, Hinz *et al.* demonstrated the success of DFT with SCAN-L+rVV10 XC in predicting the molecular dissociation boundary in dense D (Ref. 6). This accuracy of the SCAN-L+rVV10 functional, in combination with the development of T-SCAN-L, is the main motivation for constructing iFPEOS.

In the high-T regime, above $T \approx$ 250,000 K, standard Kohn–Sham (KS) DFT calculations become prohibitively expensive due to the high number of thermally occupied orbitals; therefore, we use orbital-free (OF) DFT. In OF DFT, the KS orbital-dependent kinetic energy functional is approximated by a density-dependent one. Here we use the newly developed noninteracting free-energy density functional LKTFγTF, which is a one-parameter, tunable, convex combination of the Luo–Karasiev–Trickey free energy density functional (LKTF)[7] and Thomas–Fermi functional. We tune the γ parameter and various densities spanning iFPEOS and also perform overlapping KS and OF calculations for T point in the region of switching from OF to KS in order to verify that results for pressure and energy agree to within 1% between the two methods.

Finally, nuclear quantum effects (NQE's) are accounted for via path-integral molecular dynamics (PIMD) calculations.[8] Since PIMD calculations are much more computationally demanding, they are performed for only select ρ–T points for conditions in which NQE's are relevant. Results have been compared to those from classical MD and applied to the full iFPEOS as NQE's corrections. For computational details regarding KS, OF, and PIMD calculations, see Secs. III and IV in Ref. 9.

We compare iFPEOS to the latest results from experimental measurements of shock-compressed D, reporting principal and reshock Hugoniot[10] and sound speed along the principal Hugoniot.[11] We performed an extra calculation at initial density ρ_0 = 0.173 g/cm^3, T = 19 K so that initial conditions for solving the Rankine–Hugoniot equations are consistent with those reported in Ref. 10. The main conclusions from comparing the iFPEOS principal Hugoniot to experiment and other models is that iFPEOS provides an improvement in accuracy in the low-pressure (P < 200 GPa), low-T regime (T < 60,000 K), but at higher pressure and temperatures, the iFPEOS Hugoniot joins those predicted by other first-principles models that predict significantly lower compressibility [see Fig. 1(a)].

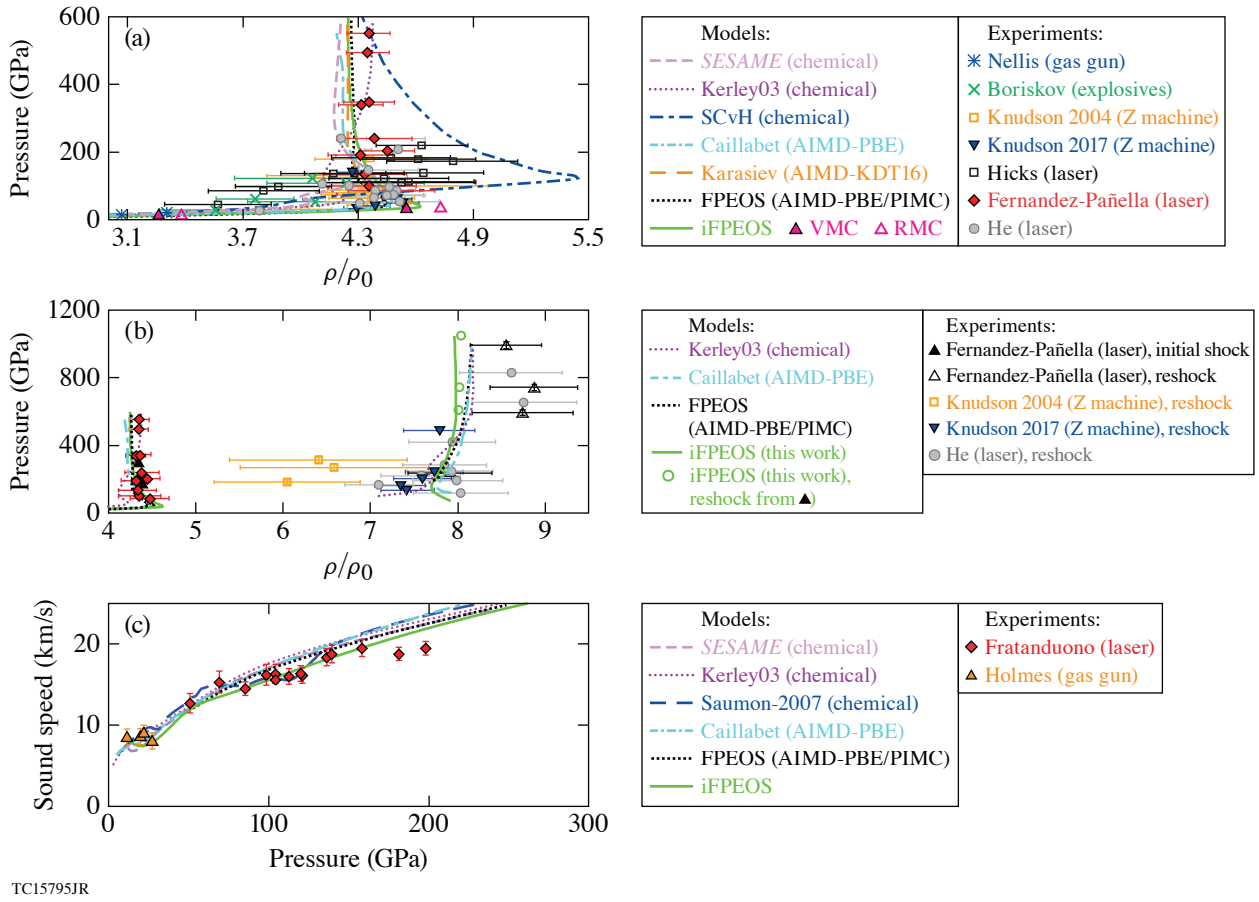

Figure 1

(a) Pressure versus compression along the principal Hugoniot of shocked D as predicted by iFPEOS and other popular first-principles and chemical EOS models and calculations along with the latest experimental data. (b) Pressure versus compression in reshocked D. Collection of points and curves below compression of 5 is select principal Hugoniot data corresponding to (a). Data above compression of 5 correspond to latest experimental measurements along with various EOS models including iFPOES reshock Hugoniot launched off of iFPEOS principal Hugoniot (solid green curve) and iFPEOS reshock states launched off of initial states corresponding to the ones reported in Ref. 10 (green circles) and determined via impedance matching with a-quartz. Green circles serve as a more direct comparison with latest experiments (black upright open triangles). (c) Sound speed along the principal Hugoniot as predicted by iFPEOS and other popular EOS models and according to latest experimental measurements. AIMD: *ab initio* molecular dynamics; KDT: Karasiev–Dufty–Trickey; PIMC: path-integral Monte Carlo; VMC: variational Monte Carlo.

Similar trends are seen in comparing iFPEOS reshock Hugoniot to experimental measurements [Fig. 1(b)], where for pressures $P > 600$ GPa, we see 6% to 11% underestimation of the compression in reshocked D. In the low-pressure regime of the reshocked Hugoniot, we see good agreement between different models that are all in good agreement with the latest experimental measurements considering the relatively larger error bars compared to measurements of principal Hugoniot. For $P > 600$ GPa, however, iFPEOS predicts even stiffer (1% to 3%) behavior than other models.

Finally, we compare iFPEOS to experimental measurements and other EOS model predictions of Eulerian sound speed along the principal Hugoniot [Fig. 1(c)]. This comparison further verifies the conclusions reached in Hugoniot comparisons, namely that iFPEOS provides slightly better agreement with experimental data in the low-pressure, low-T regime, but for $P > 200$-GPa, iFPEOS, as well as other first-principles models, significantly disagrees with experiment by overestimating the sound speed. The excellent agreement with experimental gas-gun measurements at $P < 50$ GPa is expected since this is the region of molecular dissociation, which is accurately captured by the T-SCAN-L+rVV10 functional. The improved agreement with laser-shock

experimental data at $50 < P < 200$ GPa [red diamonds in Fig. 1(c)] is attributed to the improved treatment of XC thermal effects by T-SCAN-L, which are expected to be most important in these particular thermodynamic conditions ($20{,}000 < T < 80{,}000$ K).

This material is based upon work supported by the Department of Energy National Nuclear Security Administration under Award Number DE-NA0003856, U.S. National Science Foundation PHY Grant No. 1802964, the University of Rochester, and the New York State Energy Research and Development Authority.

1. S. X. Hu *et al.*, Phys. Rev. B **84**, 224109 (2011).
2. S. X. Hu *et al.*, Phys. Plasmas **22**, 056304 (2015).
3. V. V. Karasiev, D. I. Mihaylov, and S. X. Hu, "Meta-GGA Exchange-Correlation Free Energy Density Functional to Achieve Unprecedented Accuracy for Warm-Dense-Matter Simulations," submitted to Physical Review Letters.
4. L. Caillabet, S. Mazevet, and P. Loubeyre, Phys. Rev. B **83**, 094101 (2011).
5. V. V. Karasiev, L. Calderín, and S. B. Trickey, Phys. Rev. E **93**, 063207 (2016).
6. J. Hinz *et al.*, Phys. Rev. Research **2**, 032065(R) (2020).
7. K. Luo, V. V. Karasiev, and S. B. Trickey, Phys. Rev. B **101**, 075116 (2020).
8. M. Ceriotti *et al.*, J. Chem. Phys. **133**, 124104 (2010).
9. D. I. Mihaylov *et al.*, Phys. Rev. B **104**, 144104 (2021).
10. A. Fernandez-Pañella *et al.*, Phys. Rev. Lett. **122**, 255702 (2019).
11. D. E. Fratanduono *et al.*, Phys. Plasmas **26**, 012710 (2019).

An X-Ray Penumbral Imager for Measurements of Electron-Temperature Profiles in Inertial Confinement Fusion Implosions on OMEGA

P. J. Adrian,[1] J. A. Frenje,[1] B. Aguirre,[2] B. Bachmann,[3] A. Birkel,[1] M. Gatu Johnson,[1] N. V. Kabadi,[1] B. Lahmann,[1] C. K. Li,[1] O. M. Mannion,[4] W. Martin,[2] Z. L. Mohamed,[4] S. P. Regan,[4] H. G. Rinderknecht,[4] B. Scheiner,[5] M. J. Schmitt,[5] F. H. Séguin,[1] R. C. Shah,[4] H. Sio,[3] C. Sorce,[4] G. D. Sutcliffe,[1] and R. D. Petrasso[1]

[1]Plasma Science and Fusion Center, Massachusetts Institute of Technology
[2]Sandia National Laboratories
[3]Lawrence Livermore National Laboratory
[4]Laboratory for Laser Energetics, University of Rochester
[5]Los Alamos National Laboratory

One of the main challenges of inertial confinement fusion is symmetry control of the implosion. Asymmetries reduce implosion performance and generate bulk flows that degrade the conversion of shell kinetic energy into hot-spot thermal energy. Recently, penumbral imaging of hot-spot x-ray emission was used at the National Ignition Facility to simultaneously measure hot-spot shape and temperature to assess asymmetry in different implosion designs,[1] as well as spatially resolve electron temperature to quantify mix-induced radiative cooling.[2] Penumbral imaging is a coded imaging technique, where a source of size S is imaged with an aperture of radius R_{app} such that $2R_{app} > S$. This imaging technique is used when signal statistics prevent the use of conventional pinhole imaging ($2R_{app} \ll S$). Information about spatial distribution of the emitting source is encoded in the penumbra.

We developed and fielded a new penumbral imager at the Omega Laser Facility, with 6-μm resolution, to image x rays in the energy range of 10 to 30 keV. This system is based on the existing penumbral charged-particle imaging system (PCIS).[3] Three imagers can be fielded in different ten-inch diagnostic manipulators (TIM's) to study 3-D asymmetries. We record images in different x-ray energy bands using a filtered stack of Fuji^{TM} image plates and present a technique to infer the radially dependent electron temperature $T_e(r)$.

The PCIS detectors are TIM-based diagnostics that hold an aperture 4.2 cm from the target chamber center and a detector 59 cm from the aperture, yielding a magnification of ~14. Three types of apertures are used: 1 × 2000 μm, 19 × 400 μm, or 151 × 100 μm (number of pinholes × diameter) made from a substrate of 500-μm-thick Ta, 125-μm-thick W, or 125-μm-thick W, respectively. All apertures are circular to less than 3 μm. The detector is an array of Fuji^{TM} SR x-ray image plates interspersed with x-ray filters. Each subsequent image plate is sensitive to a higher-energy portion of the x-ray spectrum: typical values for peak sensitivity range from 10- to 30-keV x rays. The image plates are scanned with 25-μm resolution. The spatial resolution of the system at a magnification of 14 is 6 μm and is limited by the combination of detector resolution and x-ray diffraction.

A burn-averaged T_e is extracted from the inferred x-ray spectrum, which is derived from the energy deposited in each penumbral image. The image-plate scanner measures the photostimulated luminescence (PSL), which is related to the energy deposited in the phosphor layer. The PSL recorded in the umbra of the kth image plate is calculated as

$$\mathrm{PSL}_k = \int_0^\infty \frac{\mathrm{IP}_{sen}(E)}{F_k(t)} \frac{j(E)}{E} T_k(E)\,\mathrm{d}E, \tag{1}$$

where E is the x-ray energy, $IP_{sen}(E)$ is the image-plate sensitivity in PSL/photon, $F_k(t)$ represents the fading of the image plate when it is scanned t minutes after exposure, $j(E)/E$ is the photon emission in photons/keV, and $T_k(E)$ is the transmission function of all filters in front of the kth image plate. The spectrum is modeled as a single-temperature bremsstrahlung emission $j(E) = A \exp(-E/T_e)$, where A and T_e are the fit variables. The main sources of error in this analysis were due to photon statistics and uncertainty in the fade curve of each image plate.

The source profile is reconstructed from the measured penumbral image using an iterative deconvolution approach based on the Lucy–Richardson algorithm.[4] On each iteration the source image is convolved with the aperture function and compared against the measured penumbral image using a χ^2 metric. Iterations stop once the reduced χ^2 metric is of the order of unity or lower. For x-ray penumbral imaging, we have found that signal statistics are excellent for x rays in the energy range of 10 to 30 keV for most implosions of interest.

Figure 1 shows [(a),(b)] penumbral images and [(c),(d)] reconstructions from a SiO_2 capsule with 422-μm radius, 2.4-μm shell thickness, gas fill of 10 atm D_2, 15 atm ^{3}He, and ~0.04 atm T_2, and imploded with 15.6 kJ of laser energy in a 0.6-ns square pulse. Both reconstructions converged in 100 iterations and show a ring-like structure resulting from the unablated glass shell that surrounds the hot spot.

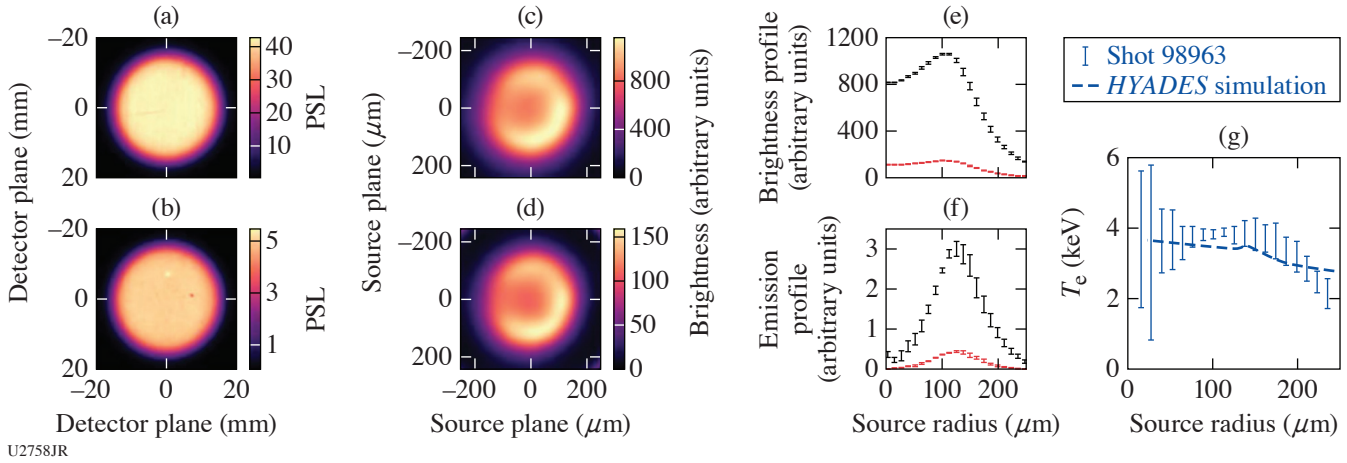

Figure 1
Data from shot 98963. The x-ray penumbral imager used a 1000-μm-radius aperture. (a) Recorded x-ray penumbral image closest to target chamber center (TCC) with 15 μm Ta + 3000 μm CR-39 ($C_{12}H_{18}O_7$) + 100-μm Al filtering. (b) X-ray penumbral image for the image plate farthest from TCC with additional 150-μm Al filtering [(c),(d)]. Reconstructed x-ray emission obtained from (a) and (b), respectively. (e) Azimuthally averaged brightness profiles (chord integrated) from (c) and (d) in black and red, respectively. (f) Radial emission profiles calculated from the surface brightness profiles in (e) via Abel inversion. (g) Measured $T_e(r)$ for shot 98963 (blue error bars). A post-shot *HYADES* simulation is shown (dashed blue line). The simulated T_e is an x-ray emission averaged over the entire implosion time.

From these measurements, the radial profile of T_e is determined. We assume spherical symmetry of the source, which allows us to azimuthally average the reconstructed x-ray images to get the brightness profile shown in Fig. 1(e). The errors in the brightness profiles are determined from the azimuthal variation in each radial bin. To extract $T_e(r)$, we calculate the radial emission from the brightness profiles by an inverse Abel transform [Fig. 1(f)]. We use a discrete version of the Abel transform proposed by Yoshikawa and Suto.[5]

The relative amplitude of the radial emission profiles is used to infer T_e in each radial bin by using Eq. (1) and filtering of the two images. A post-shot simulation of this implosion was performed using the *HYADES* 1-D radiation-hydrodynamics code,[6] and the emission-averaged $T_e(r)$ is shown in Fig. 1(g) for comparison. The measured $T_e(r)$ agrees with the simulation. The average uncertainty in $T_e(r)$ is 10%. The best inference of the temperature is where the most x-ray emission occurs. However, there are

large uncertainties at small radii due to low levels of emission occurring at those small radii. In the future, this technique will be extended to utilize three simultaneous lines of sight to reconstruct 3-D maps of electron temperature.

This material is based upon work supported by the Department of Energy National Nuclear Security Administration under Award Number DE-NA0003856, the University of Rochester, and the New York State Energy Research and Development Authority.

1. B. Bachmann *et al.*, Rev. Sci. Instrum. **87**, 11E201 (2016).
2. B. Bachmann *et al.*, Phys. Rev. E **101**, 033205 (2020).
3. F. H. Séguin *et al.*, Rev. Sci. Instrum. **75**, 3520 (2004).
4. W. H. Richardson, J. Opt. Soc. Am. **62**, 55 (1972).
5. K. Yoshikawa and Y. Suto, Astrophys. J. **513**, 549 (1999).
6. J. T. Larsen and S. M. Lane, J. Quant. Spectrosc. Radiat. Transf. **51**, 179 (1994).

Advanced Laser Development and Plasma-Physics Studies on the Multi-Terawatt Laser

I. A. Begishev,[1] V. Bagnoud,[2] S.-W. Bahk,[1] W. A. Bittle,[1] G. Brent,[1] R. Cuffney,[1] C. Dorrer,[1] D. H. Froula,[1] D. Haberberger,[1] C. Mileham,[1] P. M. Nilson,[1] A. V. Okishev,[1,†] J. L. Shaw,[1] M. J. Shoup III,[1] C. R. Stillman,[1,3] C. Stoeckl,[1] D. Turnbull,[1] B. Wager,[1] J. D. Zuegel,[1] and J. Bromage[1]

[1]Laboratory for Laser Energetics, University of Rochester
[2]GSI - Helmholtzzentrum für Schwerionenforschung GmbH, Germany
[3]Image Science, Space and Airborne System, L3Harris Technologies
[†]Deceased

The Multi-Terawatt (MTW) laser, built initially as the prototype front end for a petawatt laser system, is a 1053-nm hybrid system with gain from optical parametric chirped-pulse amplification (OPCPA) and Nd:glass. Compressors and target chambers were added, making MTW a complete laser facility (output energy up to 120 J, pulse duration from 20 fs to 2.8 ns) for studying high-energy-density physics and developing short-pulse laser technologies and target diagnostics. Further extensions of the laser support the ultrahigh-intensity laser development of an all-OPCPA system and a Raman plasma amplifier.

Fundamental research in high-energy-density physics[1] and materials science[2] has accelerated the development of kilojoule and megajoule lasers;[3–9] however, the deployment of these lasers is limited because of the cost and complexity of construction and operation. The low repetition rates (typically a few shots per day) hinders the mapping of large parameter spaces and statistical averaging. Midscale lasers producing hundreds of joules with subpetawatt peak power provide more flexibility and user access at higher repetition rates. Lasers at this scale enable technologies to be developed and tested before they are implemented on large-scale facilities. They also serve as experimental platforms for scientific research in their own right.

This summary describes LLE's MTW laser, a midscale laser system built initially as the prototype front end for OMEGA EP.[4] Currently, MTW operates at 1053 nm, where gain is provided by a combination of optical parametric amplification in nonlinear crystals and laser amplification in neodymium-doped glass. A pulse compressor and three target chambers have been added, making MTW a complete facility for plasma-physics research and laser science, as well as a development platform for laser technologies, large-area damage tests, and target diagnostics. MTW is also open for external users to conduct experiments.

Separate broadband and narrowband front ends produce synchronized nanosecond pulses for the OPCPA seed and pump, respectively. The narrowband pulse is amplified in three Nd:YLF amplifiers and frequency doubled before it pumps the OPCPA crystals. The resulting broadband signal pulse is further amplified in two Nd:glass amplifiers. After the picosecond compressor, pulses can be directed to the spherical target chamber (STC), the cylindrical target chamber (CTC), or the underdense plasma (UDP) chamber. As an option, the picosecond compressor can be bypassed to allow nanosecond pulses to propagate directly to each target chamber.

MTW can also be configured in a narrowband mode. In this case, the output of the Nd:YLF amplifiers goes directly to the Nd:glass amplifiers. This mode is mainly used to pump the final stage of an ultra-broadband optical parametric amplifier line (OPAL) after second-harmonic generation. It supports the generation of >10-J, >140-nm pulses,[10] which are compressed in the femtosecond compressor and delivered to the UDP chamber. Table I summarizes the range of parameters and applications of the broadband and narrowband modes of operation for the MTW Laser System. A general view of the MTW Laser System from the end of the system shows the picosecond grating compressor chamber (ps-GCC), the STC, and the CTC (Fig. 1).

Table I: Parameters and main applications of the MTW laser.

Mode	Application	λ (nm)	E (J)	τ (ps)
Broadband	Large-area damage tests	1053	120	2400
	High-energy-density physics, x-ray and neutron diagnostics	1053, 527	35 to 50	0.5 to 100
	Raman plasma amplification	1053, 527	35 to 40	0.5 to 100
	Ultrafast streak-camera development	1053, 264	0.1 (5 Hz)	0.5 to 100
Narrowband	Pump for all OPCPA lasers	527	50	1600
	5ω generation development	527, 263, 211	1.2 (5 Hz)	1000 to 2800

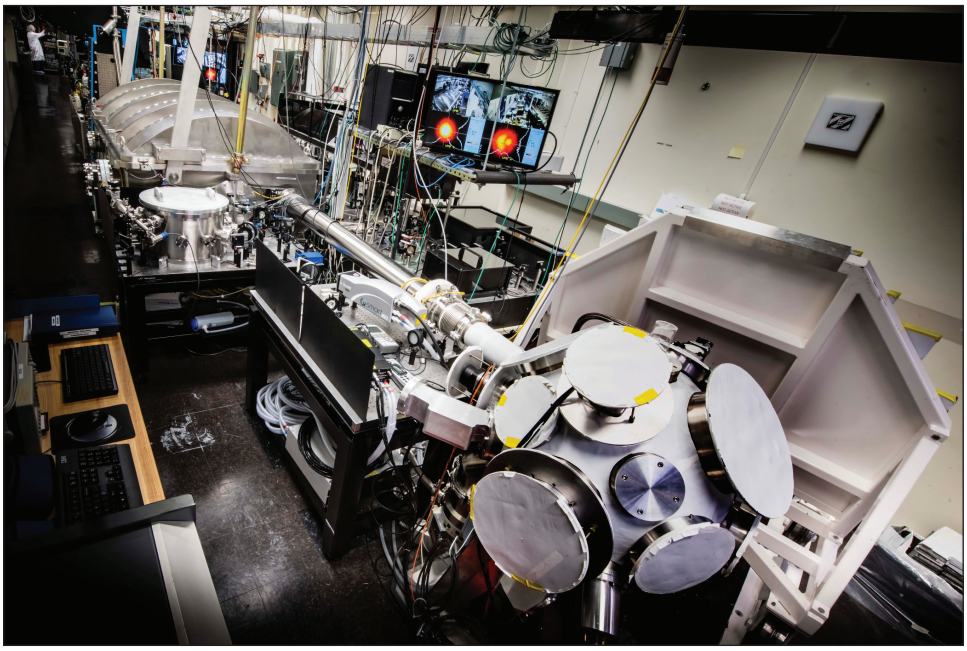

G13292JR

Figure 1
General view of the MTW Laser System from the spherical target chamber side.

A detailed layout of the MTW laser is shown in Fig. 2. Depending on the desired operation mode, switchyards (SY's) 1 to 5 (indicated as blue circles) using mirrors on kinematic or translation stages send beams along different paths. The broadband front end consists of a commercial femtosecond master oscillator, an ultrafast optical parametric amplifier (UOPA) for increased temporal contrast, and a pulse stretcher. The narrowband front end includes a pulse-shaping system,[11] a diode-pumped regenerative amplifier (regen),[12] and a crystal large-aperture ring amplifier (CLARA),[13] all operating at 1053 nm. The amplified narrowband beam is frequency converted to the second harmonic to pump the OPCPA stages,[14] which are seeded by the broadband front end. The UOPA provides approximately four-orders-of-magnitude energy amplification while restricting the associated parametric fluorescence to a few picoseconds around the output pulse.[15] This makes it possible to reduce the required gain in the OPCPA stages, where the pump pulse has a duration of a few nanoseconds, and therefore significantly reduces the level of contrast degradation resulting from nanosecond fluorescence.

The OPCPA output signal beam is shaped by a programmable spatial light modulator (PSLIM) and amplified in a Nd:glass rod amplifier (RA) and disk amplifier (DA). The pulse is then compressed in the ps-GCC and can be delivered to one of three target chambers. For solid-target experiments, the STC or CTC are typically used; gas-jet and gas-cell experiments are conducted in the UDP chamber.

In the narrowband operation mode, the switchyard mirrors send the CLARA output beam directly for amplification by the RA and DA. To pump the final noncollinear optical parametric amplifier for the OPAL system, switchyard 3 is used to send the pulse

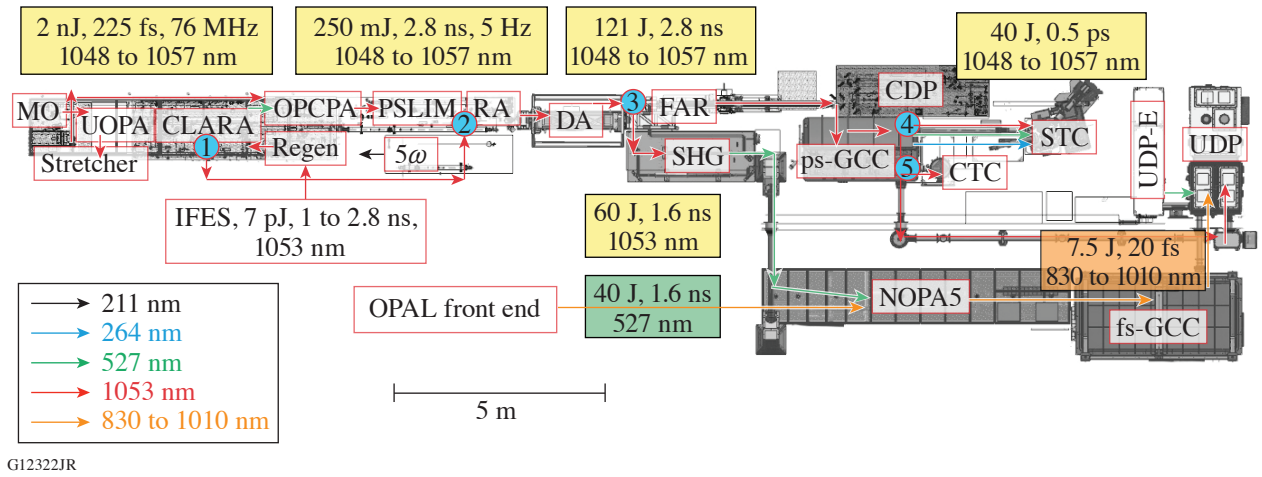

Figure 2
MTW laser layout. MO: master oscillator; IFES: integrated front-end system; 5ω: fifth-harmonic-generation table; FAR: Faraday isolator; CDP: compressor diagnostics package; NOPA5: the fifth nonlinear optical parametric amplifier stage; UDP-E: UDP laser; 1–5: switchyards.

to the second-harmonic-generation (SHG) table before propagating to the OPAL area. Here it is overlapped in time and space at the OPCPA crystal with the ultra-broadband seed pulse from the OPAL front end.[10] The amplified signal pulse is compressed in the femtosecond grating compressor chamber (fs-GCC) and sent to the UDP chamber.

The narrowband mode has also been used to develop technologies for the fifth-harmonic generation of joule-class, near-infrared pulses. For this, the CLARA output can be sent with or without amplification in the RA to the 5ω table, where several studies using cascades of nonlinear crystals have been performed.[16,17]

The gain nonuniformity of the RA can be precompensated by PSLIM.[18] Figure 3(a) shows the profile of the MTW output beam when the PSLIM is bypassed. Figure 3(b) shows that PSLIM can correct the mode to a flat, near-uniform beam profile. The high performance in the uniformity is the result of closed-loop operation of the PSLIM algorithm.

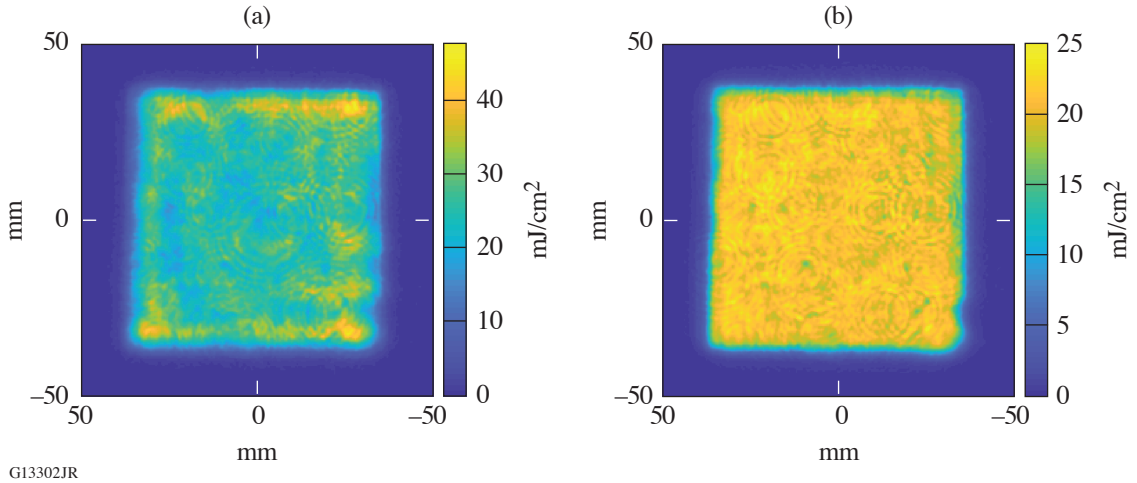

Figure 3
Rod amplifier beam profiles measured at the plane equivalent to the last hit of the beam on the grating in the compressor (a) without and (b) with PSLIM correction.

The on-shot MTW output energy is measured using pickoff calorimeters, which are cross-calibrated with a large-aperture calorimeter that covers a large energy range (1.5 J to 1000 J). Figure 4 demonstrates the MTW energy map at different voltages for the RA and DA. Curves show the increase in output energy versus RA input energy for different RA and DA voltages. Each point has a shot number, energy density, and peak-to-mean beam modulation.

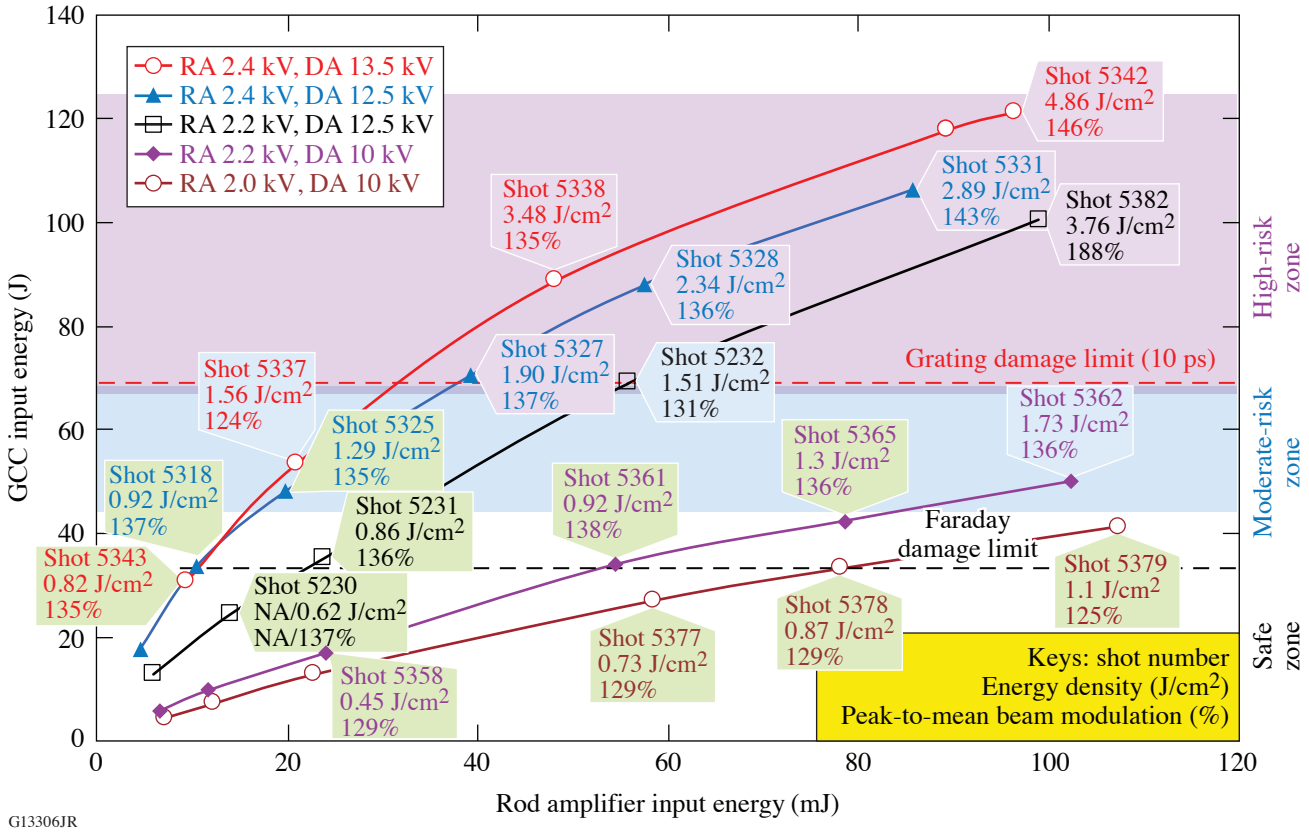

Figure 4
MTW output energy for a range of RA input energies and operating voltages for the rod and disk amplifiers. Dashed lines are damage limits imposed by the final Faraday isolator and the gratings for 10-ps pulses.

The beam propagating to the GCC and on toward the CTC and STC has two major limitations in energy; these limitations arise from the Faraday isolator and the gratings used in the compressor. The 50-J limit is set by the terbium glass damage threshold of 2 J/cm^2. The energy range below 50 J is shown in Fig. 4 as the safe zone (no shading). Because the Faraday isolator is installed before the compressor in the stretched pulse, the isolator energy limitation does not depend on the pulse duration after the compressor.

The second energy limitation is set by the damage threshold of compressor gratings, where the last hit on G1/G4 dominates. This limit does depend on the pulse duration; for example, at 10 ps, the measured damage threshold is 1.7 J/cm^2, which corresponds to the limit of output energy of 85 J. In practice, safe operation must also consider beam modulation and a safety factor of 20%, which results in a maximum energy on the final grating of approximately 70 J. The zone between 50 J and 70 J is the moderate-risk zone (blue shading), while above 70 J is the high-risk zone (purple shading). The energy on target for a 10-ps pulse is typically kept below 36 J and below 18 J for the best compression at 500 fs.

The maximum energy produced by MTW is 120 J. This is acceptable for the all-OPCPA beam path because SY3 (Fig. 2) picks the full energy beam before the last Faraday isolator.

The stretcher varies the MTW pulse duration and the sign of the chirp. A second-order scanning autocorrelator (SAC) is routinely used with the 5-Hz OPCPA beam prior to full-energy shots to measure the pulse autocorrelation width with subpicosecond precision, covering a range up to 100 ps. An autocorrelation trace of the shortest pulse is shown in Fig. 5(a) and has 497 fs at FWHM, which corresponds to a pulse duration of ~369 fs. It is shown along with a simulated autocorrelation function calculated for a transform-limited pulse based on the OPCPA's output spectrum. Both autocorrelation traces overlap well with only a 4.8% mismatch between the FWHM's.

TESSA, a time-expanded single-shot autocorrelator, is required to measure picosecond pulses when the Nd:glass amplifiers are used. It has a limit of 40 ps set by the clear aperture of the noncollinear autocorrelation crystal. Figure 5(b) shows a typical series (not taken at best compression) of single-shot autocorrelation traces, which demonstrates a highly stable operation of the MTW laser.

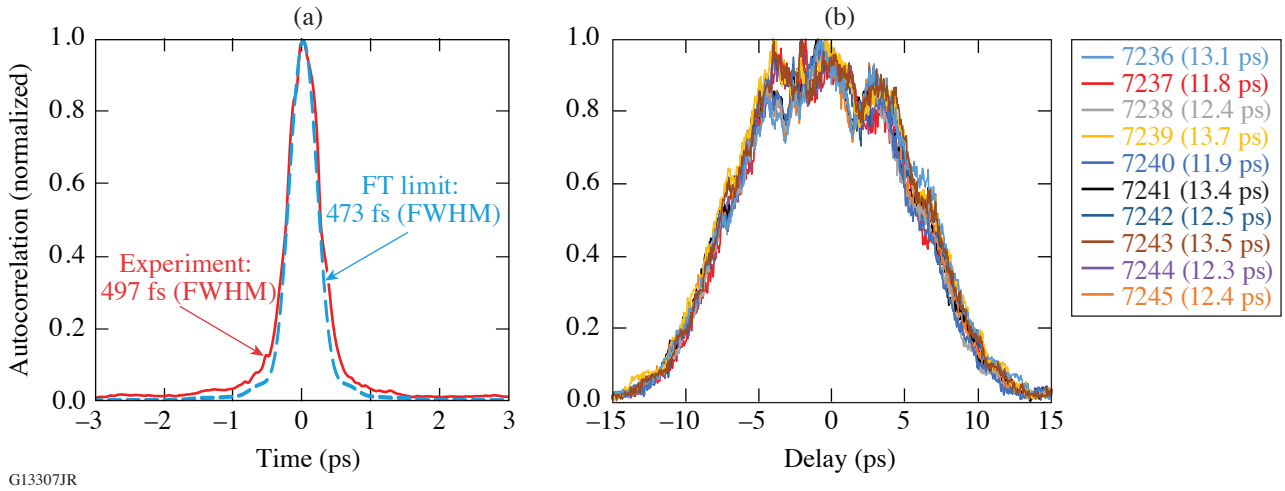

Figure 5
(a) The measured best-compression autocorrelation function and the simulated corresponding autocorrelation function calculated for a transform-limited pulse based on the OPCPA's output spectrum. (b) Single-shot autocorrelation traces taken by TESSA in a series of full-energy, not-the-best compression MTW shots.

To measure relatively long compressed pulses, a high-bandwidth 55-GHz photodiode and a 45-GHz oscilloscope are used. The duration of the resulting impulse response at 1053 nm is 17 ps, which overlaps with short compressed pulse diagnostics based on second-order autocorrelations. The real-time oscilloscope allows for single-shot acquisition; therefore, the diagnostic can be used on high-energy shots. The gain narrowing in the RA and the DA modifies the spectrum of the MTW beam. The changes on the spectrum and, therefore, on the recompressed pulse duration depend on the voltage from each amplifier and OPCPA output energy. Figure 6 shows pulse durations after the picosecond compressor measured with different diagnostics, depending on the stretcher translation stage position referenced to its position for best compression.

The nonlinear cross-correlator provides MTW temporal contrast information with high temporal resolution over an ~200-ps temporal window [Fig. 7(a)], while the high-contrast photodiode provides single-shot contrast information over a much larger temporal window with resolution limited by the bandwidth of the photodetector and oscilloscope, approximately 200 ps [Figs. 7(b) and 7(c)].

The focal spot of the MTW output beam is measured at the focus of the *f*/2 off-axis parabola in the center of the STC using a 12-bit camera and a 10× objective microscope. An attenuation of 10^6 is achieved using two 0.1% leaky wedged mirrors installed in an "antiparallel" configuration inside the GCC. Additional attenuation is provided using neutral-density filters. A typical focal spot is shown in Fig. 8(a) and has a slightly elliptical shape with major and minor axes widths of 6 μm and 5 μm, respectively; 85% of the energy is contained in a circle with a 5-μm radius [Fig. 8(b)].

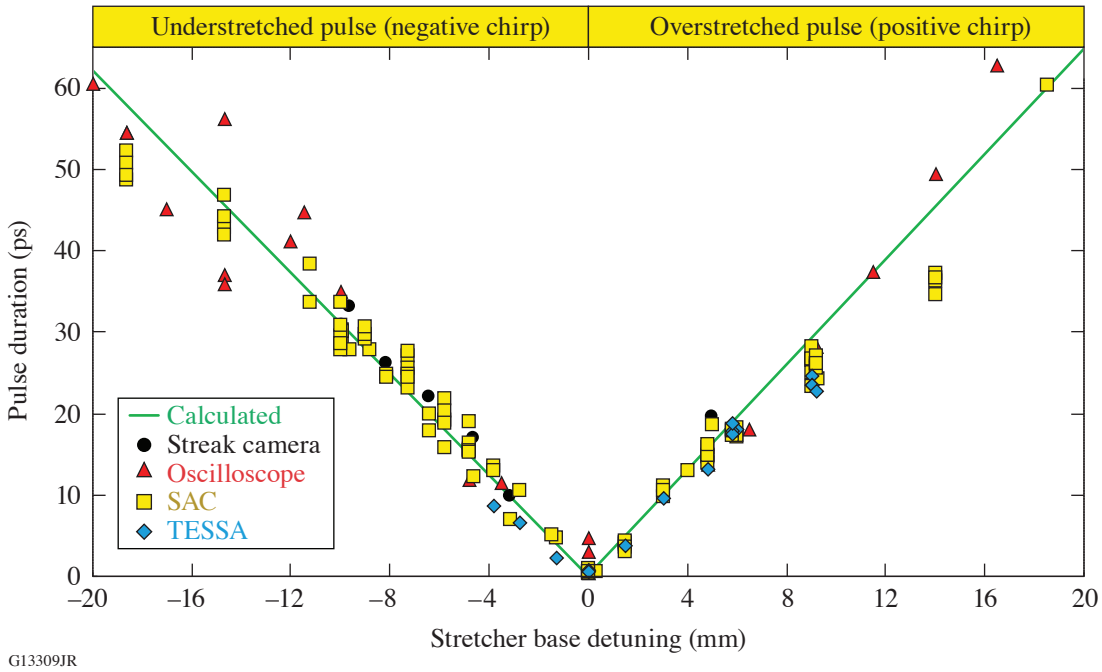

Figure 6
Compressed pulse duration adjustment by the stretcher.

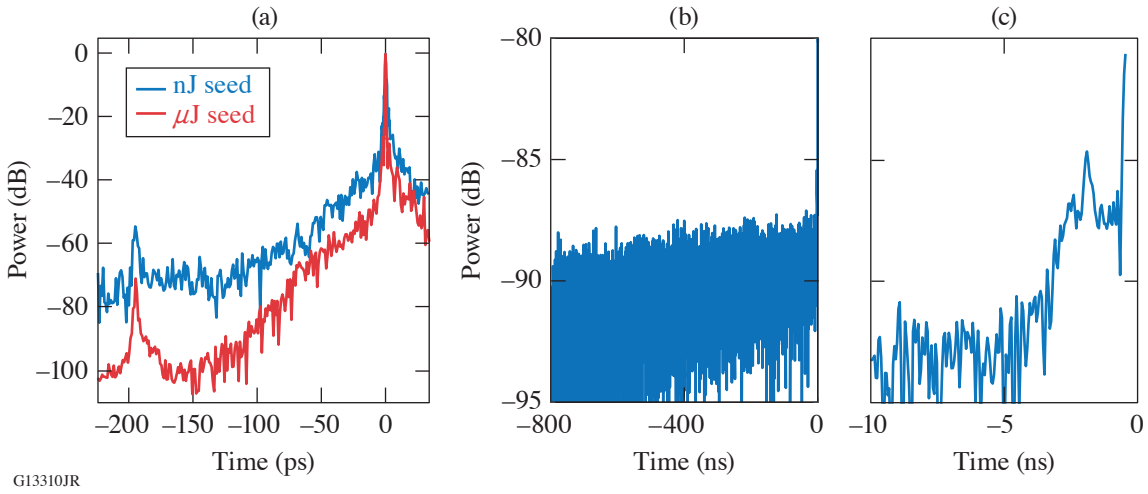

Figure 7
Temporal contrast of the compressed MTW pulse measured with (a) the nonlinear cross-correlator and [(b),(c)] with a photodiode and oscilloscope. In (a), the temporal contrast is shown before and after UOPA deployment.

The MTW wavefront is measured by a wavefront sensor. This measurement requires careful calibration of non-common-path wavefront aberrations in the diagnostic path and a determination of the single-pass contribution through the compressor. A typical MTW wavefront for a single pass through the GCC is shown in Fig. 9 and has a peak-to-valley (p–v) variation of 0.15 λ over 98% of the MTW beam.

The main applications of the MTW laser include high-energy-density science,[19,20] x-ray spectrometers,[21] neutron diagnostic development,[22] and "flying focus"—a concept where the combination of temporal chirp and longitudinal chromatic aberration

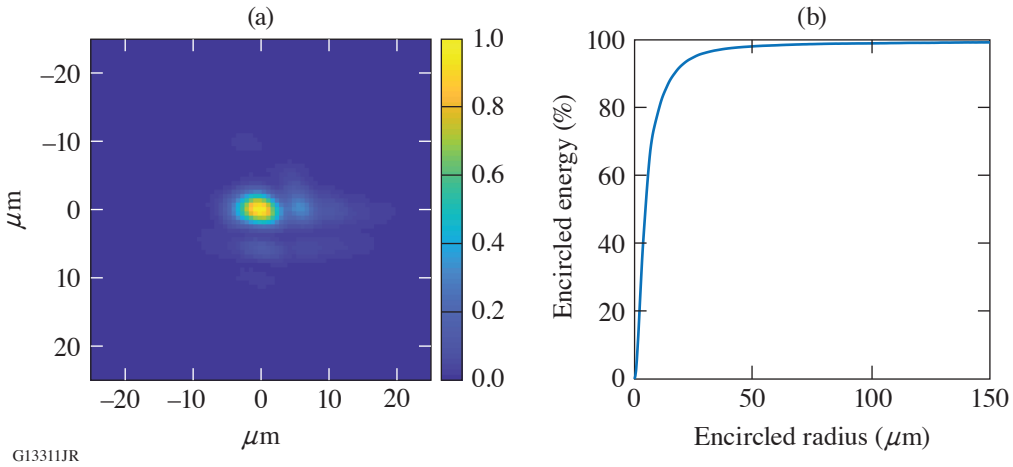

Figure 8
Focal spot of an MTW beam.

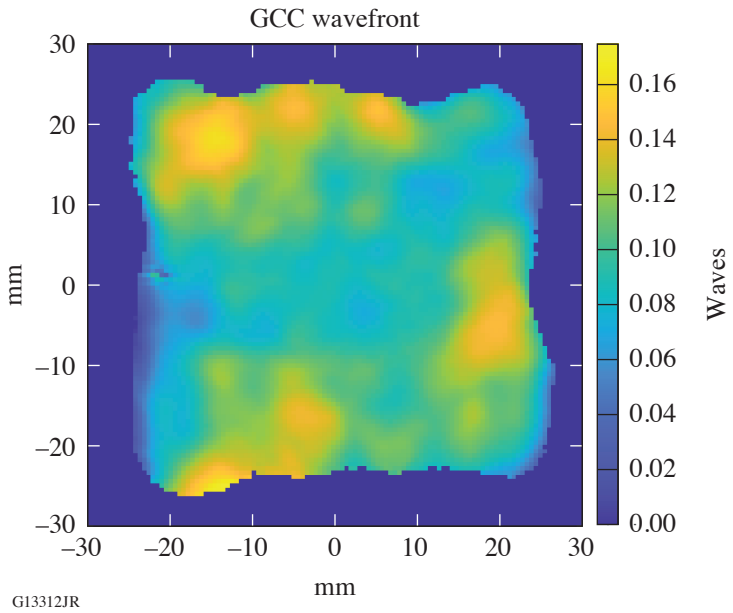

Figure 9
MTW output wavefront, with a 0.15 λ (p–v) modulation.

provides unprecedented spatiotemporal control over the velocity of a high-intensity focal spot over distances far exceeding the Rayleigh length.[23] Efforts are underway to use MTW for parametric amplification; using stimulated Raman scattering in a plasma which could be an enabling technology in the generation of ultrahigh-power laser pulses.[24]

Many experiments on MTW require wavelengths different from the 1053-nm fundamental. For example, picosecond time-resolved measurements of dense plasma line shifts[25] require the second harmonic. Timing calibration of x-ray streak cameras requires short subpicosecond pulses in the deep-UV region. Fifth-harmonic generation is necessary for many plasma diagnostics.[26,27] To satisfy these requirements and to increase the temporal contrast of compressed pulses,[28] the MTW output beam can be converted into the second, fourth, and fifth harmonics.

MTW was built based on the most-recent laser technologies and continues to develop novel ideas in laser science and engineering while also providing a flexible platform for development of frontier laser and plasma diagnostics.

This material is based upon work supported by the Department of Energy National Nuclear Security Administration under Award Number DE-NA0003856, the University of Rochester, and the New York State Energy Research and Development Authority.

1. S. Gales *et al.*, Rep. Prog. Phys. **81**, 094301 (2018).
2. A. L. Kritcher *et al.*, Nature **584**, 51 (2020).
3. G. H. Miller, E. I. Moses, and C. R. Wuest, Opt. Eng. **43**, 2841 (2004).
4. J. H. Kelly *et al.*, J. Phys. IV France **133**, 75 (2006).
5. J. Ebrardt and J. M. Chaput, J. Phys.: Conf. Ser. **244**, 032017 (2010).
6. C. N. Danson *et al.*, Nucl. Fusion **44**, S239 (2004).
7. G. Xu *et al.*, Rev. Laser Eng. **36**, 1172 (2008).
8. V. V. Lozhkarev *et al.*, Laser Phys. Lett. **4**, 421 (2007).
9. C. N. Danson *et al.*, High Power Laser Sci. Eng. **7**, e54 (2019).
10. J. Bromage *et al.*, High Power Laser Sci. Eng. **7**, e4 (2019).
11. J. R. Marciante and J. D. Zuegel, Appl. Opt. **45**, 6798 (2006).
12. A. V. Okishev *et al.*, in Advanced Solid-State Lasers, edited by M. E. Fermann and L. R. Marshall, OSA TOPS Vol. 68 (Optical Society of America, Washington, DC, 2002), pp. 418–422.
13. V. Bagnoud *et al.*, Appl. Opt. **44**, 282 (2005).
14. V. Bagnoud *et al.*, Opt. Lett. **30**, 1843 (2005).
15. C. Dorrer, A. V. Okishev, and J. D. Zuegel, Opt. Lett. **32**, 2143 (2007).
16. I. A. Begishev *et al.*, Opt. Lett. **43**, 2462 (2018).
17. I. A. Begishev *et al.*, Opt. Express **29**, 1879 (2021).
18. S.-W. Bahk, I. A. Begishev, and J. D. Zuegel, Opt. Commun. **333**, 45 (2014).
19. P. M. Nilson *et al.*, J. Phys. B: At. Mol. Opt. Phys. **48**, 224001 (2015).
20. M. Storm *et al.*, Rev. Sci. Instrum. **79**, 10F503 (2008).
21. C. R. Stillman *et al.*, Rev. Sci. Instrum. **87**, 11E312 (2016).
22. C. Stoeckl *et al.*, Rev. Sci. Instrum. **87**, 053501 (2016).
23. D. H. Froula *et al.*, Nat. Photonics **12**, 262 (2018).
24. D. Turnbull *et al.*, Plasma Phys. Control. Fusion **61**, 014022 (2019).
25. C. R. Stillman *et al.*, Phys. Rev. E. **95**, 063204 (2017).
26. J. S. Ross *et al.*, Rev. Sci. Instrum. **81**, 10D523 (2010).
27. V. V. Ivanov, A. A. Anderson, and I. A. Begishev, Appl. Opt. **55**, 498 (2016).
28. D. Hillier *et al.*, Appl. Opt. **52**, 4258 (2013).

Analytic Phase Solutions of Three-Wave Interactions

S.-W. Bahk

Laboratory for Laser Energetics, University of Rochester

Analytic solutions for three- and four-wave nonlinear interactions have long been available since the very early discussion of this phenomena.[1] The original approach provided amplitude and relative phase solutions as well as a general methodology based on utilizing constants of motion. The conservation laws involving the total and relative powers and relative phase between these waves provide an efficient way of solving the coupled-wave equations. The phase solution provided by Ref. 1 is the relative phase solution between interacting waves, but *no closed-form phase solution of an individual wave* has been presented over the last six decades. Smith and Bowers have shown that one of the interacting waves that starts from zero intensity always develops a phase that is linearly proportional to wave-vector mismatch.[2] Buchvarov *et al.* derived phase solutions by approximating the intensity solutions using an approximate form of the elliptic sinus function.[3] Marhic found analytic phase solutions for four-wave interactions but did not extend the work to three-wave mixing.[4] Ross *et al.* found phase solutions under nondepleted pump assumption.[5] The authors also provided the integral form of the phase solution as a function of pump depletion in a pump-depletion regime.[6] A survey of these works reveals that complete analytic phase solutions for three-wave mixing have not been previously published, while the necessity of the phase solutions has been mostly addressed by numerical methods.[7] In this summary, analytic phase solutions are shown to exist for three-wave mixing, expressible using standard mathematical functions. The solution provided by Ross *et al.*[6] does not explicitly show the functional dependence of phase on the wave-vector mismatch, Δk. It rather shows a linear dependence of Δk with residual terms hidden in the integral. The integral also does not provide an advantage in calculation speed over a direct numerical integration of differential equations.

Despite the availability of numerical approaches for directly solving differential equations with a minimum number of approximations, analytic solutions are still powerful tools in calculating optical parametric chirped-pulse–amplification (OPCPA) performance where the group delay and walk-off terms are often negligible. The temporal slice or the corresponding frequency slice of a stretched signal pulse interacts with the concurrent portion of the pump pulse, independent of other frequency slices. The local approximation approach allows one to apply analytic solutions at each wavelength slice. This computational efficiency allows for fast estimation and optimization of the phase performance in the amplified signal beam. Phase performance is becoming increasingly important in ultra-broadband, large-scale OPCPA systems since they are associated with the performance of pulse compression and focusing.

The equations for three interacting waves inside a second-order nonlinear medium in a normalized electric field (E') unit are written as

$$\frac{\mathrm{d}E'_\mathrm{s}}{\mathrm{d}z} = \mathrm{i}E'^{*}_\mathrm{i}E'_\mathrm{p}\exp\left(-i\Delta kz\right), \quad \frac{\mathrm{d}E'_\mathrm{i}}{\mathrm{d}z} = \mathrm{i}E'^{*}_\mathrm{s}E'_\mathrm{p}\exp\left(-\mathrm{i}\Delta kz\right), \quad \frac{\mathrm{d}E'_\mathrm{p}}{\mathrm{d}z} = \mathrm{i}E'_\mathrm{s}E'_\mathrm{i}\exp\left(i\Delta kz\right),$$

where the subscripts s, i, and p indicate signal, idler, and pump fields. The z axis is defined to be normal to the crystal surface and Δk is measured along the z axis, i.e., $\Delta k = k_{\mathrm{s},z} + k_{\mathrm{i},z} - k_{\mathrm{p},z}$. Normalized electric fields are defined as

$$E_s' = \frac{d}{c}\sqrt{\frac{\omega_i\omega_p}{n_i n_p}}E_s = \sqrt{u}\exp(i\phi_s), \quad E_i' = \frac{d}{c}\sqrt{\frac{\omega_s\omega_p}{n_s n_p}}E_i = \sqrt{v}\exp(i\phi_i), \quad E_p' = \frac{d}{c}\sqrt{\frac{\omega_s\omega_i}{n_s n_i}}E_p = \sqrt{w}\exp(i\phi_p).$$

The constants d and c are the second-order effective nonlinear coefficient and speed of light. It can be shown that there are four constants of motion: $p = u + w$, $q = v + w$, $r = u–v$, and $s = \sqrt{uvw}\cos\left(\Delta kz + \phi_s + \phi_i + \phi_p\right) – (1/2)\Delta k w_0$. Since these are constants, we can set these values using the initial intensity and phase values, e.g.,

$$p = u_0 + w_0,\ s = \sqrt{u_0 v_0 w_0}\cos\left(\phi_{s,0} + \phi_{i,0} - \phi_{p,0}\right) - \frac{1}{2}\Delta k w_0, \text{ etc.}$$

The 0 subscript indicates the initial value at $z = 0$.

The solutions in the case of $v_0 = 0$ (no idler input) will be shown here without derivation. This case covers the most-practical case for optical parametric amplification. The intensity solutions are

$$w(z) = w_c - \frac{w_c - w_0}{\mathrm{dn}^2\left(z/z_d, m\right)}, \quad u(z) = p - w(z), \quad v(z) = q - w(z),$$

where $z_d = 1/\sqrt{w_c - w_a}$ and $m = (w_b – w_a)/(w_c – w_a)$.The three pump parameters (w_a, w_b, w_c) are calculated as

$$w_a = (1/2)\left(p' - \sqrt{p'^2 - \Delta k^2 w_0}\right), \ w_b = w_0, \ \text{ and } w_c = (1/2)\left(p' + \sqrt{p'^2 - \Delta k^2 w_0}\right),$$

with $p' = p + \Delta k^2/4$. The function dn is one of the Jacobi elliptic functions. The unit of normalized intensity is in (distance unit of $z)^{-2}$. The pump depletion distance, which is of the order of z_d, is easily estimated from the initial normalized pump intensity or vice versa.

The phase solutions are

$$\phi_s(z) = \phi_s(0) - \frac{\Delta k}{2}\left(\frac{w_c - w_0}{w_c - p}\right)\left\{z - z_d\,\Pi\left[\frac{(w_c - p)}{-u_0}m; am\left(z/z_d, m\right), m\right]\right\},$$

$$\phi_i(z) = \pi/2 - \phi_s(0) + \phi_p(0) - \frac{1}{2}\Delta k z,$$

$$\phi_p(z) = \phi_p(0) + \frac{\Delta k}{2}\left(\frac{w_c - w_0}{w_c}\right)\left\{z - z_d\,\Pi\left[\frac{w_c}{w_0}m; am\left(z/z_d, m\right), m\right]\right\}. \tag{1}$$

Here, $\Pi(.;.,.)$ and $am(.,.)$ are an elliptic integral of the third kind and the Jacobi amplitude function, respectively.

The signal gain $[u(z)/u(0)]$ and phase plots are shown in Fig. 1 for a 6.8-cm KDP crystal with its c axis oriented at 41.06° with respect to the z axis. The initial signal and pump intensities are 1 MW/cm^2 at 0.930 μm and 1 GW/cm^2 at 0.527 μm, respectively. The phase plot shows linear behavior within the amplification bandwidth, which can be approximated to $-\Delta k/2\left[z - \tanh\left(\sqrt{w_0}\,z\right)/\sqrt{w_0}\right]$ (dashed line). In the depletion regime for a 20-dB amplifier, $\sqrt{w_0}z \sim 3.68$, so phase in the linear regime can be further approximated to $-0.36\ \Delta kz$. Outside the gain bandwidth the phase asymptotically approaches $-w_0 z/\Delta k$ (dotted line). The signal beam in this regime therefore has a pump-beam-intensity–dependent phase profile, which can be used to produce an instantaneous phase profile. This behavior is similar to the cascaded nonlinearity.[8]

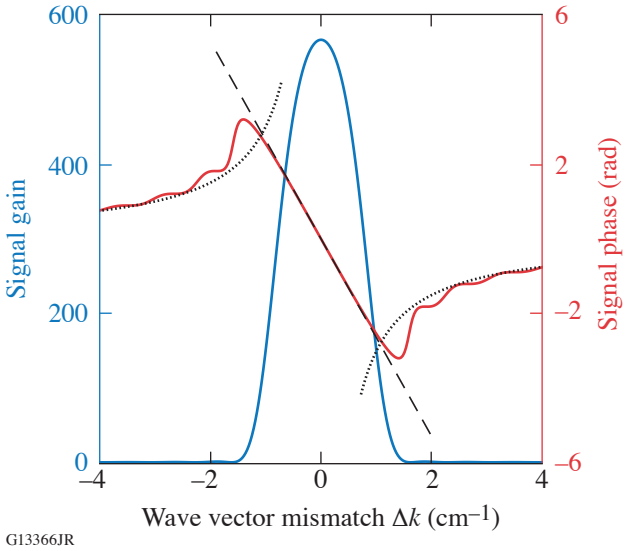

Figure 1
Intensity and phase response with respect to wave-vector mismatch Δk.

These results provide convenient tools to estimate the phase performance of an OPA in either spatial or temporal domains. The analytic phase solutions for the case of nonzero idler input and for the case of sum-frequency and second-harmonic generation are discussed in detail in Ref. 9.

This material is based upon work supported by the Department of Energy National Nuclear Security Administration under Award Number DE-NA0003856, the University of Rochester, and the New York State Energy Research and Development Authority.

1. J. A. Armstrong *et al.*, Phys. Rev. **127**, 1918 (1962).
2. A. V. Smith and M. S. Bowers, J. Opt. Soc. Am. B **12**, 49 (1995).
3. I. Buchvarov *et al.*, Opt. Commun. **141**, 173 (1997).
4. M. E. Marhic, J. Opt. Soc. Am. B **30**, 62 (2013).
5. I. N. Ross *et al.*, Opt. Commun. **144**, 125 (1997).
6. I. N. Ross *et al.*, J. Opt. Soc. Am. B **19**, 2945 (2002).
7. I. Jovanovic *et al.*, J. Opt. Soc. Am. B **26**, 1169 (2009).
8. R. DeSalvo *et al.*, Opt. Lett. **17**, 28 (1992).
9. S. W. Bahk, Opt. Lett. **46**, 5368 (2021).

Overcoming Gas-Ionization Limitations with Divided-Pulse Nonlinear Compression. II. Experimental Demonstration

G. W. Jenkins,[1,2] C. Feng,[1] and J. Bromage[1,2]

[1]Laboratory for Laser Energetics, University of Rochester
[2]Institute of Optics, University of Rochester

Recent work has pushed self-phase modulation (SPM)-based spectral broadening to higher pulse energies and peak powers in both hollow-core fibers (HCF's)[1] and multipass cells (MPC's).[2] While these demonstrations have shown that spectral broadening using gas-based SPM can handle very high pulse energies, they also show that the process is limited by gas ionization. SPM-based pulse compressors must therefore employ large-core fibers or large focal spots in the MPC to avoid gas ionization.

This work demonstrates a more-scalable method to improve the energy limits of SPM-based pulse compression: divided-pulse nonlinear compression (DPNLC) (illustrated in Fig. 1). In DPNLC, a high-energy pulse is divided into multiple low-energy pulses that are spectrally broadened, recombined back into a high-energy pulse, and then compressed to a short duration.[3] The low-energy pulses have peak intensities below the gas-ionization intensity threshold and can pass through the HCF with high efficiency, while the original high-energy pulse would suffer significant ionization losses.

We demonstrated the advantages of DPNLC by spectrally broadening 1030-nm, 1.2-ps laser pulses in a 300-μm inner-diam, xenon-filled HCF. Xenon was chosen for its low ionization threshold to make the ionization effects strong. The advantage of

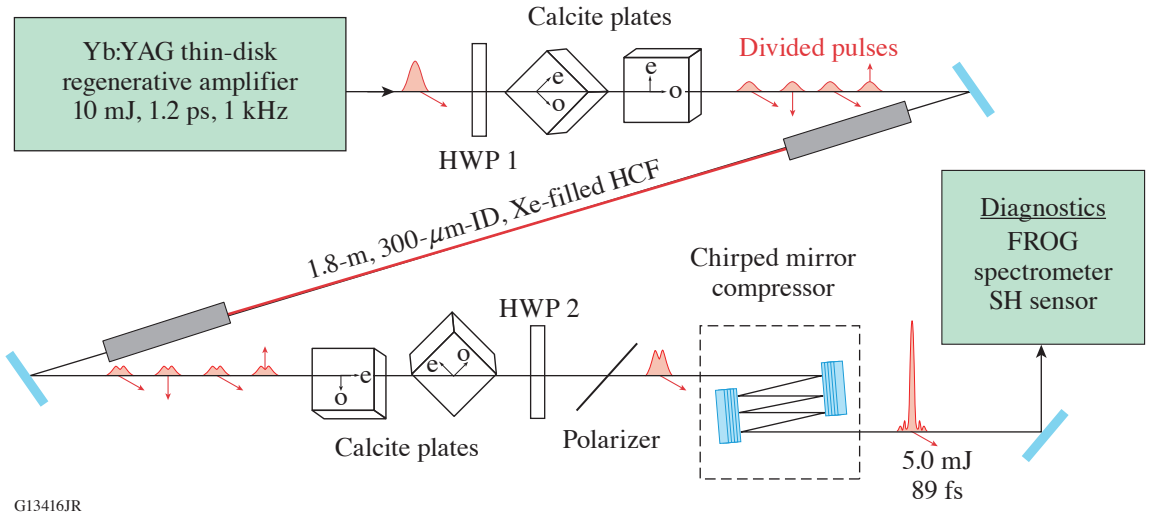

Figure 1
Apparatus for divided-pulse nonlinear compression analyzed in this summary. Birefringent plates with extraordinary axis "e" and ordinary axis "o" are used to divide one pulse into multiple low-energy, orthogonally polarized pulses. Red arrows indicate the pulse's polarization, and the distorted pulse shape after the SPM stage indicates an arbitrary reshaping by nonlinear processes in the SPM stage. FROG: frequency-resolved optical gating; HWP: half-wave plate; SH: Shack–Hartmann wavefront sensor.

DPNLC was immediately obvious based on the output energy from the HCF, as shown in Fig. 2. We measured a near-constant 67% transmission through the evacuated HCF for all input pulse energies, but once the HCF was filled with xenon, the transmission became a strong function of input energy. Above an input energy of 4 mJ, the xenon started ionizing, reducing the fiber throughput dramatically. HCF is a loosely guiding structure so plasma defocusing after the onset of ionization defocused energy out of the HCF and created large energy losses. Larger input energies did not yield larger output energies beyond exceeding the ionization threshold; the ionization clamped the output to approximately 2 mJ, consistent with previous observations of ionization in HCF.[1,4] By dividing the input into two pulses, the cumulative energy threshold for ionization nearly doubled and good HCF throughput was measured up to 8-mJ input energy. Finally, by dividing into four pulses, the full 10-mJ pulse energy of our laser can be broadened in the fiber without ionization losses; we measured 6.6-mJ output (four pulses with 1.65 mJ each).

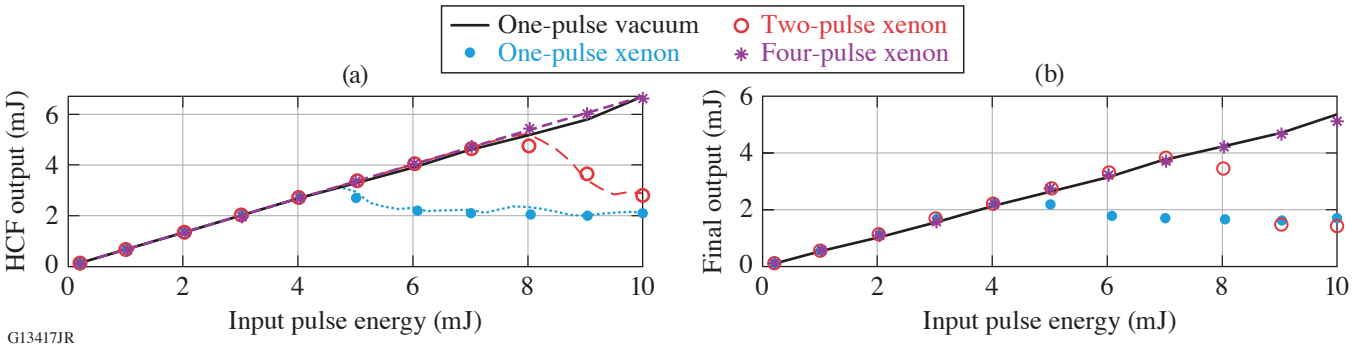

Figure 2
HCF throughput using one, two, and four divided pulses (a) immediately after the HCF and (b) after recombination and compression. Data markers plot the experimentally measured energies and dotted and dashed curves in (a) plot the simulated output energy using the model in our previous work.[5]

After the HCF, the divided and SPM-broadened pulses were recombined using a set of calcite plates identical to the dividing plates. High recombination efficiency was measured. For two pulses, the recombination efficiency was near perfect (>97% limited by the 2.5% polarization reflection on the polarizer) for all energies before the onset of gas ionization. After the onset of ionization, phase artifacts from the gas–plasma mixture prevented good recombination, and we measured losses as great as 50%. For four pulses, recombination efficiency was high for all input energies; we measured only a slow decrease with pulse energy down to 89% efficiency at 10-mJ input. We attribute this decrease to a small misalignment of the first calcite plate.

After recombination, DPNLC produces a high-quality output beam. The measured spectra are significantly broadened and agree with the side-lobed structure produced by SPM-based spectral broadening. The beam profile is high quality, with a measured M^2 of 1.21 and 1.20 along the x and y axes of the beam, respectively. M^2 did not change significantly with pulse energy, or the number of pulse divisions, or ionization plasma effects. We attribute the M^2 invariance to the modal-cleaning properties of the HCF;[6] only the fundamental mode of the fiber has significant energy at the end of the fiber and the fundamental mode sets the beam profile.

Finally, the recombined pulse was compressed with chirped mirrors to a shorter duration. In the best case (10-mJ input with four-pulse division), the pulse was compressible to 89 fs (FWHM), a compression factor of 13.4×. We estimate this pulse has 5.0 mJ of pulse energy at 91% of the transform-limited pulse's peak power. We expect this work will motivate DPNLC for use on higher-energy systems. DPNLC can enable large factors without the need for switching gases or making the system prohibitively large.

This material is based upon work supported by the Department of Energy National Nuclear Security Administration under Award Number DE-NA0003856, the University of Rochester, and the New York State Energy Research and Development Authority.

1. G. Fan *et al.*, Opt. Lett. **46**, 896 (2021).
2. M. Kaumanns *et al.*, Opt. Lett. **46**, 929 (2021).
3. H. Jacqmin *et al.*, J. Opt. Soc. Am. B **32**, 1901 (2015).
4. O. Hort *et al.*, J. Opt. Soc. Am. B **32**, 1055 (2015).
5. G. W. Jenkins, C. Feng, and J. Bromage, Opt. Express **28**, 31,943 (2020).
6. P. Patimisco *et al.*, J. Appl. Phys. **118**, 113102 (2015).

Electric-Field Enhancement Caused by Subwavelength-Sized Particles Located on the Surface of Multilayer Dielectric Mirrors

H. Huang, K. R. P. Kafka, and S. G. Demos

Laboratory for Laser Energetics, University of Rochester

An important factor that limits the output performance of laser systems is the coupling of energy from the laser beam into localized areas of its constituent optical components, which leads to permanent modification of the affected localized regions (commonly referred to as laser-induced damage). There are a number of underlying mechanisms that introduce such localized damage precursors that are typically associated with the introduction of impurities during the manufacturing process, during handling and installation of the optic, or due to contamination during operation. While this problem has been extensively investigated for large-aperture nanosecond laser systems, the impact of particle contamination on the laser-damage performance of short-pulse laser systems has only recently received attention.[1,2] Whereas most of the optics of concern in nanosecond laser systems are transmissive, optical elements for short-pulse laser systems are typically reflective and are based on metal or multilayer dielectric (MLD) coating designs. A laser pulse impinging on the surface of an optical component can interact with particles, such as contamination debris, to produce a scattered electric field. The coherent superposition of this scattered field with the incident laser field can significantly increase the local field intensity. This effect can be of critical importance because it can reduce the laser-induced–damage threshold of the affected component. To address this issue, a combination of experimental and modeling effort is required to assess the specific features of such contamination particles that pose a high risk for the lifetime and performance of the optics. These features include the size of the particles in combination with their shape and their optical and thermomechanical properties.

In this work, we use a field-propagation code to determine the magnitude and location of the electric-field enhancement arising from the presence of small particles located on the surface of MLD mirrors. In our modeling we consider a steady-state, monochromatic electric-field distribution within the volume of interest. Taking into account the 20 to 30 fs required for fields to propagate throughout the simulated volume, the results are directly applicable to laser pulse durations longer than that time. For shorter pulses, we would need to consider the time-dependent nature of the electric-field distribution. The monochromatic nature of the simulations also neglects potential effects due to broad bandwidths of ultrashort pulses. Here we study the following variables:

- Particle material: transparent dielectric or metal with high reflectivity
- Particle size $\lambda/8$ to 2λ (for laser wavelength λ)
- Particle shape: regular (spherical, cubic, triangular) or irregular
- Region of interest: particle surface, inside the particle, and inside the coating
- Particle density: coherent effects arising from adjacent particles

The model estimates the peak electric-field intensity as a function of the particle size normalized by the incident wavelength. Two particle shapes (rectangle and triangle) and two classes of material optical properties (dielectric/transparent and metal/absorbing) are considered. Figure 1 summarizes the modeling results providing the maximum field intensity values and their general location separated into four general categories: inside the MLD layers, inside the particles, below the surface of the optic (within the MLD layers), and on the surface of the particle. The shape and material optical properties of the particle (such as the reflectance by the particle surface and its absorption properties) govern this interaction. Furthermore, the locations and value of

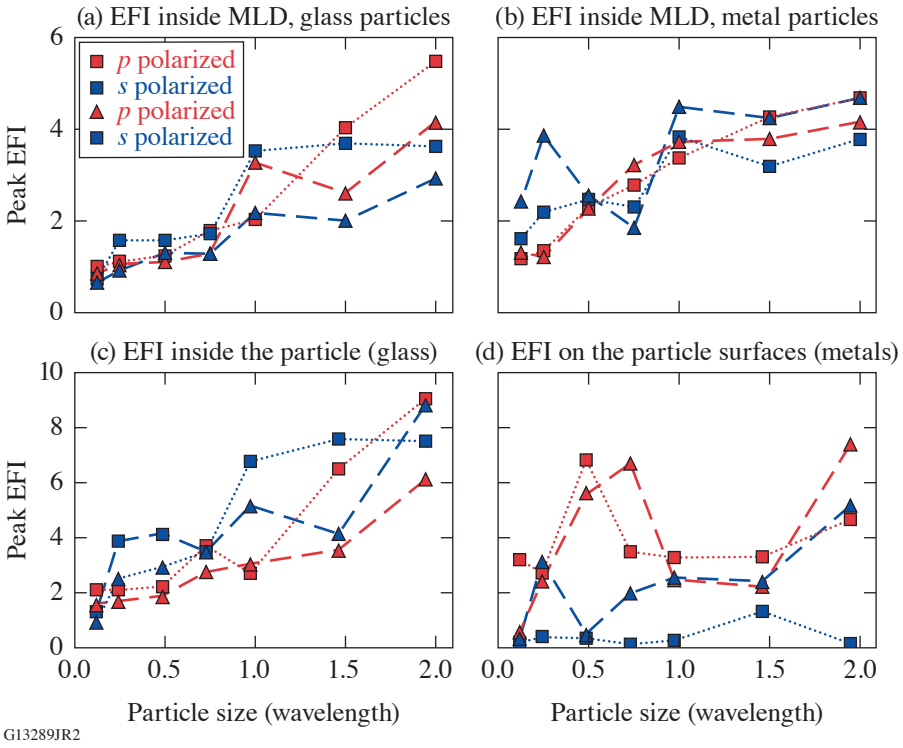

Figure 1
The peak electric-field intensity (EFI) as a function of the ratio between the particle size and the incident wavelength for two particle shapes (rectangle and triangle depicted as solid squares and triangles, respectively) using *p*-polarized and *s*-polarized (red and blue shapes, respectively) laser beams inside the MLD for (a) glass and (b) metal particles, (c) inside the bulk for glass, and (d) on the surface for metal particles.

maximum field intensity are indicators of the locations of damage initiation and the corresponding reduction of the laser-damage threshold in the presence of debris particles, respectively.

The results suggest that particle sizes as small as 1/4 of the laser wavelength can introduce a field enhancement that is higher than that inherent to the coating-design parameters. Such particles would be very difficult to detect after the installation of the optic; therefore, an effective way for detecting particles smaller than wavelength may be needed. Understanding the field enhancement on laser optics caused by contamination particles located on the surface is important in terms of estimating the associated reduction of the laser-induced–damage threshold. On the other hand, understanding of the field enhancement on the particles help understand secondary contamination effects[1,2] that can also have detrimental effect on the damage resistance of the optic. Although this study is limited by the resolution and the nature of the 2-D modeling, we expect that the general conclusions are still valid. We plan further studies using more advanced modeling capabilities to further study specific cases that are relevant to the performance and lifetime of optics located inside the grating compressor chamber in the OMEGA EP Laser System. Quantitative modeling of this effect provides guidance to determine quality control for fabrication, handling, and maintenance of optics.

This material is based upon work supported by the Department of Energy National Nuclear Security Administration under Award Number DE-NA0003856, the University of Rochester, and the New York State Energy Research and Development Authority.

1. K. R. P. Kafka and S. G. Demos, Opt. Lett. **44**, 1844 (2019).
2. K. R. P. Kafka *et al*., Opt. Eng. **60**, 031009 (2020).

Central Density and Low-Mode Perturbation Control of Inertial Confinement Fusion Dynamic Shell Targets

W. Trickey,[1] V. N. Goncharov,[1,2] I. V. Igumenshchev,[1] A. Shvydky,[1] T. J. B. Collins,[1] and E. M. Campbell[1]

[1]Laboratory for Laser Energetics, University of Rochester
[2]Department of Mechanical Engineering, University of Rochester

The dynamic shell is a new class of target in inertial confinement fusion (ICF).[1] ICF targets require a high-density outer shell to contain a fusion burn triggered by the ignition of a central low-density fuel. Traditionally, this outer shell is formed during capsule production by the manufacture of a solid, cryogenic deuterium–tritium (DT) layer. In the dynamic shell target, the high-density outer layer is formed dynamically in-flight via a series of laser pulses that compress the target, allow it to rebound, and then decelerate the expanding plasma, forming a shock that develops into the shell. In this summary, we first consider control of the fuel density in the central region, set by the initial profile of the laser pickets. By controlling the central density, it is possible to modify the convergence ratio (CR) of the implosion. Secondly, we consider how best to minimize low-mode perturbation through the choice of beam-port configuration.

In conventional targets, CR is determined mainly by the implosion velocity and shell adiabat. High convergence ratios require high implosion velocities; such implosions are susceptible to hydrodynamic instabilities formed during the acceleration of the shell. However, CR can additionally be controlled by changing the initial density of the central vapor region. In conventional targets this is limited by the operational temperature range of the DT ice. The dynamic shell target can access a broader range of central densities by controlling the laser pickets. Longer pulses allow for longer periods of expansion and therefore lower central densities. This is plotted in Fig. 1, where two pulses are shown to have a central density range of nearly an order of magnitude, 0.1 to 0.8 mg/cm^3.

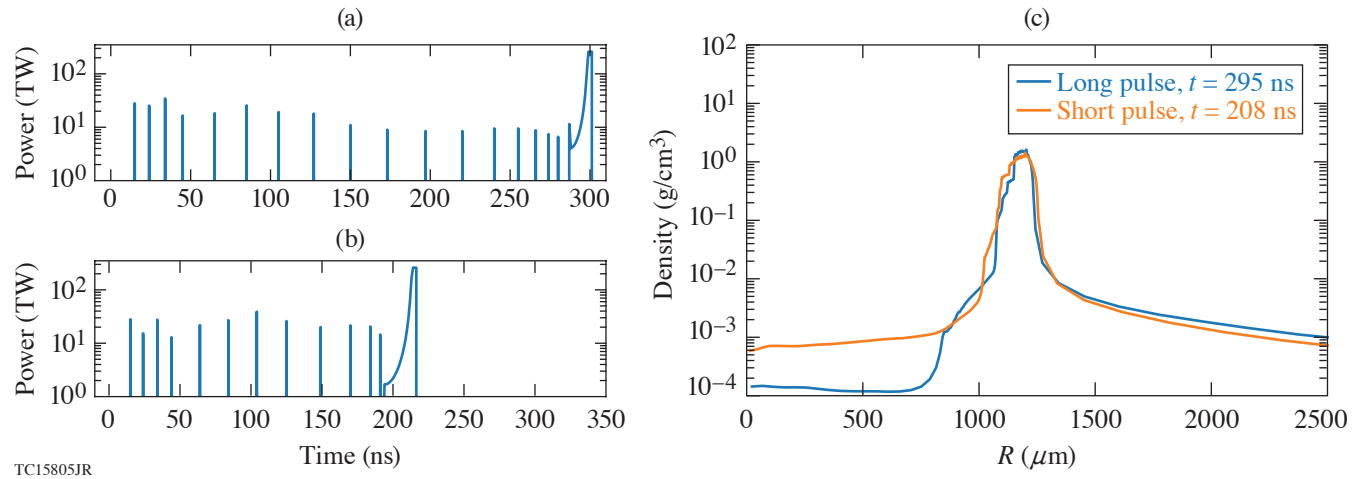

Figure 1
Time profiles of the laser profile for a (a) long- and (b) short-pulse dynamic shell target. (c) The mass-density profiles from a *LILAC* simulation, taken at the point of shell formation.

In the formation of the dynamic shell, there are three sequences of hydrodynamic implosion, expansion, and implosion again. The long periods involved allow ample time for low-mode ($\ell \leq 20$) perturbations to form, threatening the stability of the shell. Beam-port geometry is a major contributor to these perturbations. Previous work by Murakami *et al.*[2] has shown that high-performing configurations can be found using a technique where each port is modeled as a charged particle fixed to the surface of a sphere. In a numerical simulation initialized with a random configuration, the particles are allowed to repel up to the point where they reach a minimum Coulomb potential across the surface of a sphere. Using this technique it was found that configurations with certain beam numbers produced "particularly symmetric" configurations, which are observed as sharp drops in the root-mean-square perturbation in Fig. 2.

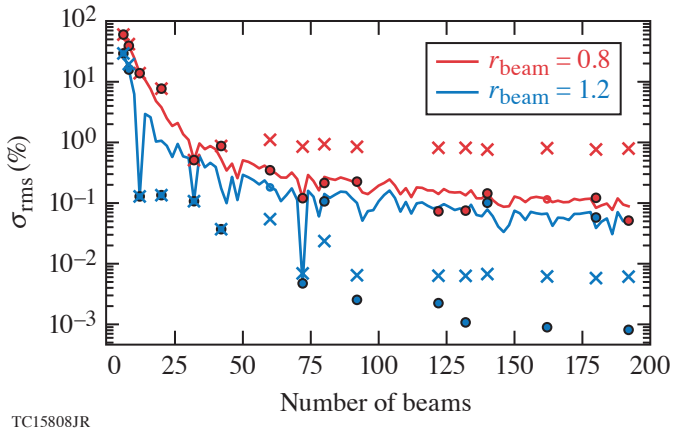

Figure 2
The root-mean-square perturbation as a function of beam number for two sets of super-Gaussian beam parameters. The solid curves show the performance of charged-particle configurations. Icosahedral configurations are shown as ×'s. Icosahedral initialized charged-particle configurations are shown as circles.

In the present work, it is shown that high performance occurs when the charged-simulation naturally tends toward a polyhedral shape, namely the geodesic icosahedron. These icosahedral configurations have a spectral mode structure where the majority of the nonuniformity is supplied by only a select number of modes and all other modes contribute negligible perturbation. This is in contrast to a typical charged-particle configuration that will have similar contributions from all modes up to a dominant beam mode. The main contributing mode in icosahedral configurations is $\ell = 6$; high performance comes when the beam shape suppresses the $\ell = 6$ mode. A further improvement can be made when icosahedral configurations are optimized using a charged-particle simulation. The effect is to reduce the $\ell = 6$ mode while sacrificing increased contribution from other less-significant modes. Different geometries and spectral mode structures of the configurations are shown in Fig. 3. In Fig. 2, it can be seen that the icosahedral configurations optimized with the charged-particle method achieve the lowest nonuniformity of all the configurations.

This material is based upon work supported by the Department of Energy National Nuclear Security Administration under Award Number DE-NA0003856, the University of Rochester, and the New York State Energy Research and Development Authority.

1. V. N. Goncharov *et al.*, Phys. Rev. Lett. **125**, 065001 (2020).
2. M. Murakami and D. Nishi, Matter Radiat. Extremes **2**, 55 (2017).

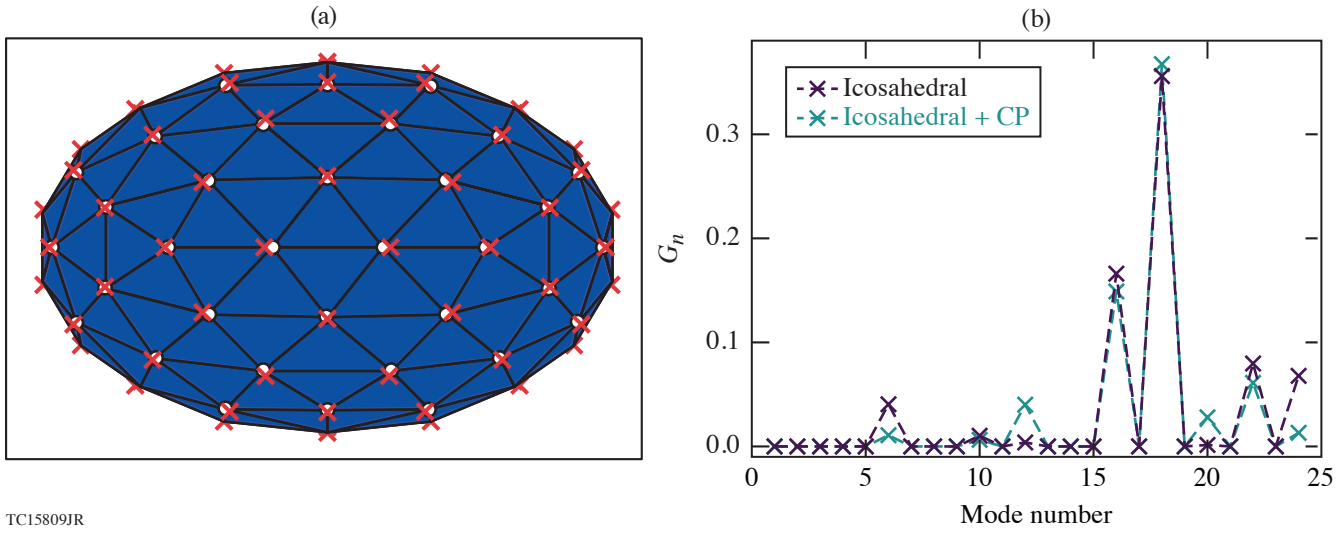

Figure 3
Comparisons between icosahedral and icosahedral initialized, charged-particle configurations. (a) The blue surface and white circles show the position of beam ports for a 92-beam icosahedral configuration, the red ×'s show where the beam ports move under a charged-particle simulation. (b) The change in the geometric factors between the two configurations.

High Yields in Direct-Drive Inertial Confinement Fusion Using Thin-Ice DT Liner Targets

C. A. Williams,[1,2] R. Betti,[1,2,3] V. Gopalaswamy,[2,3] and A. Lees[2,3]

[1]Department of Physics and Astronomy, University of Rochester
[2]Laboratory for Laser Energetics, University of Rochester
[3]Department of Mechanical Engineering, University of Rochester

Achieving the thermonuclear instability known as "ignition" in inertial confinement fusion implosions requires high levels of compression and large fusion yields.[1] This summary centers around a new target design—the thin-ice DT liner—that is intended to greatly increase neutron yields from direct-drive implosions on OMEGA.

Nominal OMEGA cryogenic implosions are able to produce implosion velocities v_{imp} within the range of 350 to 450 km/s, which generate ion temperatures ~5 keV when the deuterium–tritium (DT) shell stagnates at the target center.[2] The implosion velocity can be increased to over 650 km/s by driving large-outer-diam targets (~1010 μm) with thinner DT ice layers (~34 μm), with the target in Fig. 1(a) serving as an example. The implosion velocity scales as

$$v_{\text{imp}} \propto \sqrt{\frac{P_{\text{a}}}{\rho_0}\left(\frac{R_0}{\Delta_0}\right)}, \tag{1}$$

where P_{a} is the ablation pressure, ρ_0 is the initial density of the shell, R_0 is the initial shell radius, and Δ_0 is the initial shell thickness.[3] Therefore, large initial aspect ratios (R_0/Δ_0) allow DT liners to be imploded quickly without increasing laser intensity, which is preferred since intensities above 10^{15} W/cm^2 excite deleterious laser–plasma interactions that reduce laser absorption and limit compression.[4]

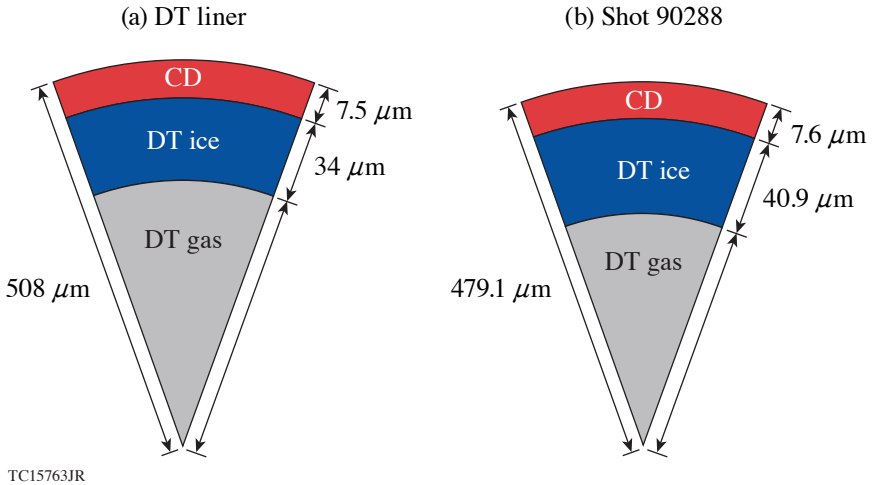

Figure 1
A target geometry comparison between (a) a thin-ice DT liner and (b) the capsule of shot 90288, a more-conventional direct-drive target. Note that the DT liner is 6% larger in diameter, yet, its fuel layer is 17% thinner, which raises v_{imp} according to Eq. (1).

One-dimensional simulations of DT liners exhibit neutron-averaged ion temperatures just below 9 keV and core temperatures up to 14 keV. These elevated temperatures greatly augment the fusion reaction rate, which leads directly to an increase in fusion yield. Statistical models predict DT liner yields to exceed 3.5×10^{14} fusion reactions when driven with ~30 kJ of 351-nm laser light.

Historically, thin and fast implosions are degraded by hydrodynamic instabilities that jeopardize the integrity of the shell during the acceleration phase of the implosion.[5] Furthermore, the instabilities that grow while the shell accelerates can feed through the shell to its inner surface and perturb it. During deceleration, the inner shell surface is unstable and the seeded perturbations are free to grow, which leads to reduced temperatures and pressures in the stagnating fusion fuel. The designs of this work promote stability during shell acceleration by raising the laser power early in the pulse, as shown in Fig. 2. This causes strong shock waves to travel through the shell, creating entropy and density profiles that are conducive for ablative stabilization of the in-flight shell.[6] In fact, strong ablative stabilization results in a 25% decrease in the cutoff wave number of DT liners compared to shot 90288, a previous high-performing implosion performed on OMEGA. Due to the high temperature of the hot spot and low density of the confining shell, DT liners benefit greatly from ablative stabilization during deceleration as well.[7] The temporally shaped pulses presented in this work demonstrate cutoffs in the unstable spectrum at lower modes than nominal implosions; they cut off at $\ell \approx 35$ for DT liners compared to a cutoff at $\ell \approx 45$ for shot 90288. The square pulse shape produces a more-extreme spectrum than the temporally shaped laser pulses; it has its cutoff mode number at $\ell \approx 15$, corresponding to greatly improved deceleration phase stability.

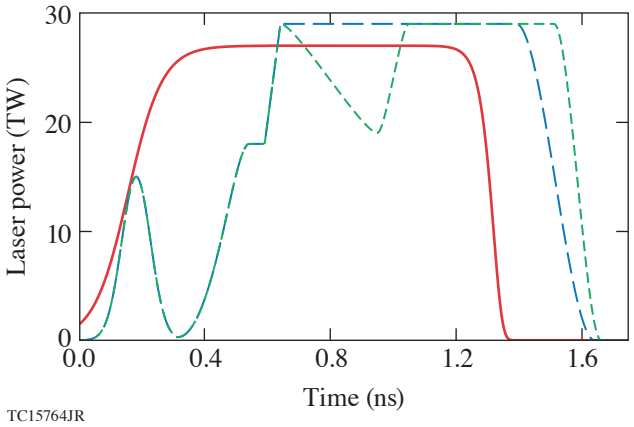

Figure 2
The laser pulse shapes used to irradiate the target described in Fig. 1(a). The laser energy of the square (solid red curve), flattop (long dashed blue curve), and double-spike (short dashed green curve) pulses is 31 kJ each.

Simulations of thin-ice DT liners show them to possess unique properties apart from their ability to produce high yields. For instance, higher mass ablation at the hot spot/cold shell interface during deceleration leads to a substantial accumulation of mass in the hot spot. At the time of peak neutron-production rate (the bang time), roughly 60% of the total areal density comes from the hot-spot plasma, with the remaining 40% provided by the cold tamping shell. In contrast, for high-convergence implosions such as shot 90288, only ~40% of the total areal density comes from the hot spot. The cold shell accounts for the remaining 60%.

The distinction between hot spot and cold shell vanishes as the in-flight shell entropy is increased, a regime easily accessed by using square pulses. Instead of two distinct regions at bang time, the unablated mass is nearly constant density and the temperature gradient becomes smoother, with temperatures above 6 keV persisting up to 25 μm from the target center. Implosions of this kind resemble those of volume ignition designs, in which all of the unablated mass acts as a hot spot.

An additional consequence of the thin ice layer in DT liner targets is that by starting with less ice at the beginning of the implosion, most of the fuel mass (up to 70% in the reported designs) has been ablated by bang time. This allows the return shock rebounding off the target origin to pass through almost all of the final fuel mass. Since most of the piston-like compression work is done by the shocked portion of the shell, DT liners act as efficient pistons with very little residual kinetic energy in the unshocked "free-fall" portion of the shell.[8]

The designs for thin-ice DT liner targets show that fusion energies above 1 kJ can be attained with only ~30 kJ of laser energy. If validated experimentally, this would be the first demonstration of capsule gain for an implosion on the 60-beam OMEGA laser, with capsule gain defined as the ratio of fusion energy yield to in-flight shell kinetic energy. Realizing the record yields that DT liners are predicted to produce will help LLE shot designers find an optimum between the high-yield, low-convergence DT liners and more-conventional designs that have greater areal densities but lower yields.

This material is based upon work supported by the Department of Energy National Nuclear Security Administration under Award Number DE-NA0003856, the University of Rochester, and the New York State Energy Research and Development Authority.

1. J. Nuckolls *et al.*, Nature 239, **139** (1972).
2. R. Betti and O. A. Hurricane, Nat. Phys. **12**, 435 (2016).
3. R. S. Craxton *et al.*, Phys. Plasmas **22**, 110501 (2015).
4. W. Seka *et al.*, Phys. Plasmas **16**, 052701 (2009).
5. Lord Rayleigh, in *Scientific Papers* (Cambridge University Press, Cambridge, England, 1900), Vol. II.
6. K. Anderson and R. Betti, Phys. Plasmas **10**, 4448 (2003).
7. V. Lobatchev and R. Betti, Phys. Rev. Lett. **85**, 4522 (2000).
8. R. Betti *et al.*, Phys. Plasmas **9**, 2277 (2002).

LLE's Summer High School Research Program

R. S. Craxton

Laboratory for Laser Energetics, University of Rochester

During the summer of 2021, eight students from Rochester-area high schools participated in the Laboratory for Laser Energetics' Summer High School Research Program. This was the 32nd year of the program, which started in 1989. The 2020 program was unfortunately canceled because of the Covid pandemic. In 2021, LLE held a fully virtual program for students who had applied and been interviewed for the 2020 program. The program started earlier than usual (in the middle of June rather than after July 4) and finished earlier (in the middle of August) to meet the schedules of the graduating seniors. The program comprised nine weeks rather than the usual eight.

The goal of LLE's program is to excite a group of highly motivated high school students about careers in the areas of science and technology by exposing them to research in a state-of-the-art environment. Too often, students are exposed to "research" only through classroom laboratories, which have prescribed procedures and predictable results. In LLE's summer program, the students experience many of the trials, tribulations, and rewards of scientific research. By participating in research in a real environment, the students often become more excited about careers in science and technology. In addition, LLE gains from the contributions of the many highly talented students who are attracted to the program.

The students spent most of their time working on their individual research projects with members of LLE's technical staff. The projects were related to current research activities at LLE and covered a broad range of areas of interest including experimental diagnostic development, computer modeling of implosion physics, experimental design, plasma-physics simulations, physical chemistry, future laser system design, and scientific data management (see Table I).

The students attended weekly seminars on technical topics associated with LLE's research. Topics this year included laser physics, fusion, nonlinear optics, nuclear physics, pulsed power, fiber optics, and LLE's cryogenic target program. The students also learned how to give scientific presentations and were introduced to LLE's computational resources.

The program culminated on 11 August with the virtual "High School Student Summer Research Symposium," at which the students presented the results of their research to an audience including parents, teachers, and LLE staff. The students' written reports will be made available on the LLE Website and bound into a permanent record of their work that can be cited in scientific publications.

Three hundred and ninety-nine high school students have now participated in the program. This year's students were selected from nearly 70 applicants to the canceled 2020 program. LLE is planning a normal, in-person program for 2022.

This material is based upon work supported by the Department of Energy National Nuclear Security Administration under Award Number DE-NA0003856, the University of Rochester, and the New York State Energy Research and Development Authority.

Table I: High School Students and Projects—Virtual Program, Summer 2021.

Name	High School	Supervisor	Project Title
Semma Alfatlawi	Victor	C. J. Forrest	Inferring a Neutron Yield from Nuclear Activation Techniques
Felix Huang	Webster Schroeder	H. G. Rinderknecht	Uniformity of X-Ray Prepulses for Imprint Mitigation in Directly Driven Implosions
Audrey Kohlman	Churchville-Chili	R. S. Craxton	Polar-Direct-Drive Designs for the Laser Megajoule
Meghan Marangola	Brighton	R. S. Craxton	Optimization of Direct-Drive Designs for a Proposed Dual Direct-/Indirect-Drive Laser
Tyler Petrillo	Webster Schroeder	R. S. Craxton	Development of a Polar-Direct-Drive Design for a Large-Diameter Beryllium Target on the National Ignition Facility
Leo Sciortino	School of the Arts	R. W. Kidder	Data Services to Improve Access to Scientific Image Data
Aditya Srinivasan	Pittsford Sutherland	A. B. Sefkow and M. Lavell	Exploration of Collision Models for Hybrid Fluid-Kinetic Simulations
Andrew Wu	Pittsford Mendon	K. L. Marshall	Computational Modeling of the Polarizability of Liquid Crystals

FY21 Q4 Laser Facility Report

J. Puth, M. Labuzeta, D. Canning, and R. T. Janezic

Laboratory for Laser Energetics, University of Rochester

During the fourth quarter of FY21, the Omega Facility conducted 304 target shots on OMEGA and 257 target shots on OMEGA EP for a total of 561 target shots (see Tables I and II). OMEGA averaged 10.1 target shots per operating day, averaging 88.1% Availability and 93.9% Experimental Effectiveness. OMEGA EP averaged 8.7 target shots per operating day, averaging 91.0% Availability and 97.1% Experimental Effectiveness.

Table I: OMEGA Laser System target shot summary for Q4 FY21.

Program	Laboratory	Planned Number of Target Shots	Actual Number of Target Shots
ICF	LLE	66	67
	LANL	11	11
	LLNL	22	22
	SNL	11	9
ICF Subtotal		110	109
HED	LLE	16.5	16
	LANL	11	7
	LLNL	55	44
	SNL	11	11
HED Subtotal		93.5	78
LBS	LLE	11	12
	LLNL	11	10
LBS Subtotal		22	22
AIBS		11	9
APL		11	14
OFES		11	14
CMAP		11	11
NLUF		60.5	47
Grand Total		330	304

AIBS: Academic and Industrial Basic Science
APL: Applied Physics Labs (Johns Hopkins University)
CMAP: Center for Matter at Atomic Pressures
LBS: Laboratory Basic Science
NLUF: National Laser Users Facility
OFES: Office of Fusion Energy Sciences

Table II: OMEGA EP Laser System target shot summary for Q4 FY21.

Program	Laboratory	Planned Number of Target Shots	Actual Number of Target Shots
ICF	LLE	31.5	49
	LLNL	21	21
ICF Subtotal		52.5	70
HED	LLE	14	20
	LANL	14	13
	LLNL	38.5	42
	SNL	7	8
HED Subtotal		73.5	83
LBS	LLNL	14	18
LBS Subtotal		14	18
AIBS		14	19
CMAP		14	18
LaserNetUS		21	23
NLUF		17.5	18
Calibration	LLE	7	8
Grand Total		213.5	257

During this quarter, the port H2 neutron time-of-flight diagnostic was installed and activated on OMEGA to add additional views to the neutronics suite of diagnostics. This additional view has allowed scientists to measure variations in ion temperature along a previously uncharacterized axis.

The Gas-Jet Target System, a ten-in. manipulator (TIM)-based payload that injects a plume of gas into the vacuum of the target chamber immediately prior to laser shot arrival and allows for the formation of a low-density plasma, has been upgraded to provide up to 1500 psia of pressure. The design of the nozzle controls the speed and pattern of the gas plume and configurations allowing Mach numbers in the range of 3 to 8 have been characterized at this point. With adequate design time, users may request additional nozzle designs.

Publications and Conference Presentations

Publications

X. Bian, J. K. Shang, E. G. Blackman, G. W. Collins, and H. Aluie, "Scaling of Turbulent Viscosity and Resistivity: Extracting a Scale-Dependent Turbulent Magnetic Prandtl Number," Astrophys. J. Lett. **917**, L3 (2021).

A. R. Christopherson, R. Betti, C. J. Forrest, J. Howard, W. Theobald, J. A. Delettrez, M. J. Rosenberg, A. A. Solodov, C. Stoeckl, D. Patel, V. Gopalaswamy, D. Cao, J. L. Peebles, D. H. Edgell, W. Seka, R. Epstein, M. S. Wei, M. Gatu Johnson, R. Simpson, S. P. Regan, and E. M. Campbell, "Direct Measurements of DT Fuel Preheat from Hot Electrons in Direct-Drive Inertial Confinement Fusion," Phys. Rev. Lett. **127**, 055001 (2021).

D. H. Edgell, P. B. Radha, J. Katz, A. Shvydky, D. Turnbull, and D. H. Froula, "Nonuniform Absorption and Scattered Light in Direct-Drive Implosions Driven by Polarization Smoothing," Phys. Rev. Lett. **127**, 075001 (2021).

G. Fiksel, W. Fox, M. J. Rosenberg, D. B. Schaeffer, J. Matteucci, and A. Bhattacharjee, "Electron Energization During Merging of Self-Magnetized, High-Beta, Laser-Produced Plasmas," J. Plasma Phys. **87**, 905870411 (2021).

L. E. Hansen, D. E. Fratanduono, S. Zhang, D. G. Hicks, T. Suer, Z. K. Sprowal, M. F. Huff, X. Gong, B. J. Henderson, D. N. Polsin, M. Zaghoo, S. X. Hu, G. W. Collins, and J. R. Rygg, "Melting of Magnesium Oxide up to Two Terapascals Using Double-Shock Compression," Phys. Rev. B **104**, 014106 (2021).

C. J. Horsfield, M. S. Rubery, J. M. Mack, H. W. Herrmann, Y. Kim, C. S. Young, S. E. Caldwell, S. C. Evans, T. S. Sedillo, A. M. McEvoy, N. M. Hoffman, M. A. Huff, J. R. Langenbrunner, G. M. Hale, D. C. Wilson, W. Stoeffl, J. A. Church, E. M. Grafil, E. K. Miller, and V. Yu. Glebov, "First Spectral Measurement of Deuterium-Tritium Fusion γ Rays in Inertial Fusion Experiments," Phys. Rev. C **104**, 024610 (2021).

H. Huang, K. R. P. Kafka, and S. G. Demos, "Electric-Field Enhancement Caused by Subwavelength-Sized Particles Located on the Surface of Multilayer Dielectric Mirrors," Opt. Express **29**, 27,031 (2021).

N. V. Kabadi, R. Simpson, P. J. Adrian, A. Bose, J. A. Frenje, M. Gatu Johnson, B. Lahmann, C. K. Li, C. E. Parker, F. E. Séguin, G. D. Sutcliffe, R. D. Petrasso, S. Atzeni, J. Eriksson, C. Forrest, S. Fess, V. Yu. Glebov, R. Janezic, O. M. Mannion, H. G. Rinderknecht, M. J. Rosenberg, C. Stoeckl, G. Kagan, M. Hoppe, R. Luo, M. Schoff, C. Shuldberg, H. W. Sio, J. Sanchez, L. Berzak Hopkins, D. Schlossberg, K. Hahn, and C. Yeamans, "Thermal Decoupling of Deuterium and Tritium During the Inertial Confinement Fusion Shock-Convergence Phase," Phys. Rev. E **104**, L013201 (2021).

M. Kaloyan, S. Ghazaryan, C. G. Constantin, R. S. Dorst, P. V. Heuer, J. J. Pilgram, D. B. Schaeffer, and C. Niemann, "Raster Thomson Scattering in Large-Scale Laser Plasmas Produced at High Repetition Rate," Rev. Sci. Instrum. **92**, 093102 (2021).

C. F. Kawaguchi, K. A. Flippo, A. M. Rasmus, B. Tobias, T. Byvank, C. A. Di Stefano, E. C. Merritt, F. W. Doss, K. V. Kelso, N. N. Vazirani, C. Stoeckl, M. Bedzyk, R. Jungquist, and C. Mileham, "Improved Imaging Using Mn He-α X Rays at OMEGA EP," Rev. Sci. Instrum. **92**, 093508 (2021).

A. Lees, R. Betti, J. P. Knauer, V. Gopalaswamy, D. Patel, K. M. Woo, K. S. Anderson, E. M. Campbell, D. Cao, J. Carroll-Nellenback, R. Epstein, C. Forrest, V. N. Goncharov, D. R. Harding, S. X. Hu, I. V. Igumenshchev, R. T. Janezic, O. M. Mannion, P. B. Radha, S. P. Regan, A. Shvydky, R. C. Shah, W. T. Shmayda, C. Stoeckl, W. Theobald, and C. Thomas, "Experimentally Inferred Fusion Yield Dependencies of OMEGA Inertial Confinement Fusion Implosions," Phys. Rev. Lett. **127**, 105001 (2021).

B. J. MacGowan, O. J. Landen, D. T. Casey, C. V. Young, D. A. Callahan, E. P. Hartouni, R. Hatarik, M. Hohenberger, T. Ma, D. Mariscal, A. Moore, R. Nora, H. G. Rinderknecht, D. Schlossberg, and B. M. Van Wonterghem, "Trending Low Mode Asymmetries in NIF Capsule Drive Using a

Simple Viewfactor Metric," High Energy Density Phys. **40**, 100944 (2021).

M. C. Marshall, M. Millot, D. E. Fratanduono, D. M. Sterbentz, P. C. Myint, J. L. Belof, Y.-J. Kim, F. Coppari, S. J. Ali, J. H. Eggert, R. F. Smith, and J. M. McNaney, "Metastability of Liquid Water Freezing into Ice VII Under Dynamic Compression," Phys. Rev. Lett. **127**, 135701 (2021).

A. L. Milder, J. Katz, R. Boni, J. P. Palastro, M. Sherlock, W. Rozmus, and D. H. Froula, "Statistical Analysis of Non-Maxwellian Electron Distribution Functions Measured with Angularly Resolved Thomson Scattering," Phys. Plasmas **28**, 082102 (2021) (invited).

K. L. Nguyen, L. Yin, B. J. Albright, A. M. Hansen, D. H. Froula, D. Turnbull, R. K. Follett, and J. P. Palastro, "Cross-Beam Energy Transfer Saturation by Ion Trapping-Induced Detuning," Phys. Plasmas **28**, 082705 (2021).

J. L. Peebles, G. Fiksel, M. R. Edwards, J. von der Linden, L. Willingale, D. Mastrosimone, and H. Chen, "Magnetically Collimated Relativistic Charge-Neutral Electron–Positron Beams from High-Power Lasers," Phys. Plasmas **28**, 074501 (2021).

A. Pineau, B. Chimier, S. X. Hu, and G. Duchateau, "Improved Modeling of the Solid-to-Plasma Transition of Polystyrene Ablator for Laser Direct-Drive Inertial Confinement Fusion Hydrocodes," Phys. Rev. E **104**, 015210 (2021).

S. Rai, M. Hecht, M. Maltrud, and H. Aluie, "Scale of Oceanic Eddy Killing by Wind from Global Satellite Observations," Sci. Adv. **7**, eabf4920 (2021).

S. P. Regan and E. M. Campbell, "Inertial Confinement Fusion—Experimental Physics: Laser Drive," in *Encyclopedia of Nuclear Energy*, edited by E. Greenspan (Elsevier, Oxford, 2021), pp. 713–723.

H. G. Rinderknecht, T. Wang, A. Laso Garcia, G. Bruhaug, M. S. Wei, H. J. Quevedo, T. Ditmire, J. Williams, A. Haid, D. Doria, K. M. Spohr, T. Toncian, and A. Arefiev, "Relativistically Transparent Magnetic Filaments: Scaling Laws, Initial Results and Prospects for Strong-Field QED Studies," New J. Phys. **23**, 095009 (2021).

R. H. H. Scott, K. Glize, L. Antonelli, M. Khan, W. Theobald, M. Wei, R. Betti, C. Stoeckl, A. G. Seaton, T. D. Arber, D. Barlow, T. Goffrey, K. Bennett, W. Garbett, S. Atzeni, A. Casner, D. Batani, C. Li, and N. Woolsey, "Shock Ignition Laser-Plasma Interactions in Ignition-Scale Plasmas," Phys. Rev. Lett. **127**, 065001 (2021).

A. Shvydky, D. Haberberger, A. V. Maximov, R. Boni, D. Cao, J. Carroll-Nellenback, D. H. Froula, V. N. Goncharov, S. X. Hu, I. V. Igumenshchev, S. T. Ivancic, V. V. Karasiev, J. P. Knauer, P. M. Nilson, P. B. Radha, S. P. Regan, J. R. Rygg, T. C. Sangster, M. D. Rosen, and V. A. Smalyuk, "Density Evolution After Shock Release from Laser-Driven Polystyrene (CH) Targets in Inertial Confinement Fusion," Phys. Plasmas **28**, 092703 (2021).

C. Stoeckl, M. J. Bonino, C. Mileham, S. P. Regan, W. Theobald, T. Ebert, and S. Sander, "Optimization of a Short-Pulse-Driven Si He_{α} Soft X-Ray Backlighter," High Energy Density Phys. **41**, 100973 (2021).

J. von der Linden, G. Fiksel, J. Peebles, M. R. Edwards, L. Willingale, A. Link, D. Mastrosimone, and H. Chen, "Confinement of Relativistic Electrons in a Magnetic Mirror en Route to a Magnetized Relativistic Pair Plasma," Phys. Plasmas **28**, 092508 (2021).

J. Zhang, W. R. Donaldson, and G. P. Agrawal, "Impact of the Boundary's Sharpness on Temporal Reflection in Dispersive Media," Opt. Lett. **46**, 4053 (2021).

J. Zhang, W. R. Donaldson, and G. P. Agrawal, "Time-Domain Fabry–Perot Resonators Formed Inside a Dispersive Medium," J. Opt. Soc. Am. B **38**, 2376 (2021).

Y. Zhang, J. R. Davies, P. V. Heuer, and C. Ren, "Kinetic Simulation Study of Magnetized Collisionless Shock Formation on a Terawatt Laser System," Phys. Plasmas **28**, 072111 (2021).

Forthcoming Publications

S.-W. Bahk, "Analytic Phase Solutions of Three-Wave Interactions," to be published in Optics Letters.

J. Bromage, S.-W. Bahk, M. Bedzyk, I. A. Begishev, S. Bucht, C. Dorrer, C. Feng, C. Jeon, C. Mileham, R. G. Roides, K. Shaughnessy, M. J. Shoup III, M. Spilatro, B. Webb, D. Weiner, and J. D. Zuegel, "MTW-OPAL: A Technology Development Platform for Ultra-Intense Optical Parametric Chirped-Pulse Amplification Systems," to be published in High Power Laser Science and Engineering.

A. Colaïtis, I. Igumenshchev, J. Mathiaud, and V. N. Goncharov, "Inverse Ray Tracing on Icosahedral Tetrahedron Grids for Nonlinear Laser Plasma Interaction Coupled to 3-D Radiation Hydrodynamics," to be published in the Journal of Computational Physics.

S. Heidtfeld, R. Adam, T. Kubota, K. Takanashi, D. Cao, C. Schmitz-Antoniak, D. E. Bürgler, F. Wang, C. Greb, G. Chen, I. Komissarov, H. Hardtdegen, M. Mikulics, R. Sobolewski, S. Suga, and C. M. Schneider, "Generation of Terahertz Transients from $CO_2Fe_{0.4}Mn_{0.6}Si$-Heusler-Alloy/Normal-Metal Nanobilayers Excited by Femtosecond Optical Pulses," to be published in Physical Review Research.

G. W. Jenkins, C. Feng, and J. Bromage, "Alignment Tolerance Analysis for Divided-Pulse Nonlinear Compression," to be published in the Journal of the Optical Society of America B.

V. V. Karasiev, J. Hinz, S. X. Hu, and S. B. Trickey, "On the Liquid–Liquid Phase Transition of Dense Hydrogen," to be published in Nature.

D. I. Mihaylov, V. V. Karasiev, S. X. Hu, J. R. Rygg, V. N. Goncharov, and G. W. Collins, "Improved First-Principles Equation-of-State Table of Deuterium for High-Energy-Density Applications," to be published in Physical Review B.

S. Nwabunwanne and W. R. Donaldson, "Boosting the External Quantum Efficiency of AlGaN-Based Metal–Semiconductor–Metal Ultraviolet Photodiodes by Electrode Geometry Variation," to be published in the IEEE Journal of Quantum Electronics.

A. M. Saunders, C. V. Stan, K. K. Mackay, B. Morgan, J. A. K. Horwitz, S. J. Ali, H. G. Rinderknecht, T. Haxhimali, Y. Ping, F. Najjar, J. Eggert, and H.-S. Park, "Experimental Observations of Laser-Driven Tin Ejecta Microjet Interactions," to be published in Physical Review Letters.

A. Shvydky, A. V. Maximov, V. V. Karasiev, D. Haberberger, S. X. Hu, and V. N. Goncharov, "Ionization State and Dielectric Constant in Cold Rarefied Hydrocarbon Plasmas of Inertial Confinement Fusion," to be published in Physical Review E.

R. Sobolewski, "Optical Detectors and Sensors," to be published in the Handbook of Superconducting Materials.

A. Tentori, A. Colaitis, W. Theobald, A. Casner, D. Raffestin, A. Ruocco, J. Trela, E. Le Bel, K. Anderson, M. Wei, B. Henderson, J. Peebles, R. Scott, S. Baton, S. A. Pikuz, R. Betti, M. Khan, N. Woolsey, S. Zhang, and D. Batani, "Experimental Characterization of Hot-Electron Emission and Shock Dynamics in the Context of the Shock-Ignition Approach to Inertial Confinement Fusion," to be published in Physics of Plasmas.

Conference Presentations

E. M. Campbell, "A Vision of the Future for High-Power Laser Research and Its Applications," presented at Frontiers in Lasers and Applications, virtual, 5–29 July 2021.

E. M. Campbell, "Inertial Confinement Fusion: Present State of Research for Energy Demonstration and Potential Spin-Offs," presented at Curso de Verano de la Universidad Complutense de Madrid (UCM) El Escorial, virtual, 12–13 July 2021.

W. T. Shmayda, "Overview of Tritium Handling," presented at the Nevada National Security Site, virtual, 14 July 2021.

K. L. Marshall, B. E. Ugur, and W. Scullin, "Toward High-Performance Terahertz-Region Liquid Crystals: Computational Modeling of Fused-Ring Nematic and Discotic Mesogens," presented at Liquid Crystals XXV, virtual, 1–5 August 2021 (invited).

K. Churnetski, K. M. Woo, W. Theobald, P. B. Radha, R. Betti, V. Gopalaswamy, I. V. Igumenshchev, S. T. Ivancic, M. Michalko, R. C. Shah, C. A. Thomas, and S. P. Regan, "Three-Dimensional Hot-Spot Reconstruction from Cryogenic Deuterium–Tritium Polar-Direct-Drive Implosions on OMEGA," presented at High-Energy-Density Science Summer School, virtual, 2-6 August 2021.

D. Mihaylov, V. V. Karasiev, S. X. Hu, J. R. Rygg, V. N. Goncharov, and G. W. Collins, "Improved First-Principles Equation-of-State Table of Deuterium," presented at the American Physical Society Topical Group on Shock Compression of Condensed Matter Early Career Symposium, virtual, 3–4 August 2021.

C. Dorrer, "Parametric Amplification of Spectrally Incoherent Signals," presented at the Nonlinear Optics Topical Meeting, virtual, 9–13 August 2021.

The following presentations were made at the 2021 LaserNetUS User Meeting, virtual, 17–19 August 2021:

S.-W. Bahk, I. A. Begishev, S. Bucht, C. Dorrer, C. Feng, B. N. Hoffman, C. Jeon, C. Mileham, J. B. Oliver, R. G. Roides, M. J. Shoup III, M. Spilatro, B. Webb, J. D. Zuegel, and J. Bromage, " 'First Light' Results from MTW-OPAL: An All-OPCPA Platform for Laser Development and Petawatt Science."

E. M. Campbell, "Inertial Fusion Energy (IFE): Opportunities and Challenges."

E. M. Campbell, "NAS Study on High Energy Density Science," presented at the National Academy of Sciences Site Visit, virtual, 26 August 2021.

D. H. Froula, "Taming Plasmas and Controlling Laser Beams for Grand Challenge Applications," presented at the Fusion Energy Sciences Advisory Committee Meeting, virtual, 30 August 2021.

E. M. Campbell, "Laboratory for Laser Energetics (LLE) Comments on HIBEF Dedication," presented at the HIBEF Inauguration, virtual, 31 August 2021.

R. B. Spielman, "Pulsed-Power Innovations Needed for Next-Generation, High-Current Drivers," presented at the 48th IEEE International Conference on Plasma Science, virtual, 12–16 September 2021.

L. Savino, S. Atzeni, V. N. Goncharov, and I. V. Igumenshchev, "Studies on Dynamical Shell Formation for Direct-Drive Laser Fusion," presented at the 107th Italian Physical Society Conference, virtual, 13–17 September 2021.

J. D. Zuegel, "2021 Multi-Petawatt Physics Prioritization (MP3) Workshop," presented at the 4th Extremely High Intensity Laser Physics Conference, virtual, 13–17 September 2021.

E. M. Campbell, "Inertial Fusion Energy (IFE): Opportunities and Challenges," Fusion Energy Council of Canada Annual General Meeting, virtual, 15 September 2021.

S. Zhang, R. Paul, M. Ghosh, S. X. Hu, L. E. Hansen, J. R. Rygg, G. W. Collins, M. Morales, F. Malone, and D. E. Fratanduono, "Multi-Megabar Phase Transitions from First-Principles Examples in MgO and Fe," presented at the Center for Matter at Atomic Pressures Seminar, virtual, 17 September 2021.

C. Dorrer, J. Bromage, S.-W. Bahk, M. Bedzyk, I. A. Begishev, S. Bucht, C. Feng, B. N. Hoffman, C. Jeon, C. Mileham, J. B. Oliver, R. G. Roides, E. M. Schiesser, K. Shaughnessy, M. J. Shoup III, M. Spilatro, B. Webb, D. Weiner, and J. D. Zuegel, "MTW-OPAL: A Technology Development Platform for Ultra-Intense OPCPA Systems," presented at Topical Problems of Nonlinear Wave Physics, virtual, 19–22 September 2021.

S. Zhang, "Molecular to Atomic Transition in Liquid Silica at Extreme Conditions," presented at the Emerging Leader Celebration, virtual, 20–21 September 2021.

The following presentations were made at the 5th Asia Pacific Conference on Plasma Physics, virtual, 26 September–1 October 2021:

S. X. Hu, P. M. Nilson, V. V. Karasiev, D. Bishel, V. Recoules, N. Brouwer, M. Torrent, I. E. Golovkin, M. Gu, T. Walton, and S. B. Hansen, "Probing Extreme Atomic Physics of Warm and Superdense Plasmas" (invited).

P. Tzeferacos, "TDYNO: Laser-Driven Laboratory Plasma Astrophysics Experiments of Magnetized Turbulence and Fluctuation Dynamo."

K. Weichman, A. V. Arefiev, H. Mao, F. N. Beg, J. P. Palastro, A. P. L. Robinson, M. Murakami, S. Fujioka, J. J. Santos, T. Toncian, Y. Shi, T. Ditmire, H. Quevedo, and V. V. Ivanov, "Effects of Kilotesla-Level Magnetic Fields on Relativistic Laser–Plasma Interactions" (invited).

C. J. Forrest, A. Crilly, B. Applebe, V. Yu. Glebov, J. P. Knauer, O. M. Mannion, Z. L. Mohamed, P. B. Radha, S. P. Regan, A. K. Schwemmlein, and C. Stoeckl, "Inferring Absolute Neutron Energy Spectra from Time-of-Flight Spectrometers Operating in Current Mode," presented at the Neutron Detector Workshop, Knoxville, TN, 30 September–2 October 2021.


1850
MELIORA
UNIVERSITY of
ROCHESTER